POLISH
ACADEMY
OF SCIENCES
INSTITUTE
OF FUNDAMENTAL
TECHNOLOGICAL
RESEARCH

ECOLE
NATIONALE
D'INGENIEURS
DE METZ (ENIM)

ENGINEERING TRANSACTIONS

ROZPRAWY INŻYNIERSKIE - TRAITE d'INGENIERIE

QUARTERLY
VOLUME 59
ISSUE 3

WARSZAWA - METZ 2011

SUBSCRIPTIONS

Address of the Editorial Office: Engineering Transactions
Institute of Fundamental Technological Research
Pawińskiego 5B, PL 02-106 Warsaw, Poland
Tel.: (48-22) 826 12 81 ext. 206, Fax: (48-22) 826 98 15, E-mail: engtrans@ippt.gov.pl

Subscription orders for all journals edited by IPPT (Institute of Fundamental Technological Research) may be sent directly to the Publisher:
Institute of Fundamental Technological Research
e-mail: subscribe@ippt.gov.pl

Please transfer the subscription fee to our bank account: Payee: IPPT PAN,
Bank: Pekao S.A. IV O/Warszawa,
Account number 05124010531111000004426875.

All journals edited by IPPT are available also through:

- Foreign Trade Enterprise ARS POLONA ul. Obrońców 25,
  03-933 Warszawa, Poland, Tel. (48-22) 509 86 38, 509 86 37
  e-mail: arspolona@arspolona.com.pl
- RUCH S.A. ul. Jana Kazimierza 31/33,
  01-248 Warszawa, Poland,
  Tel. (48-22) 532 88 16, Fax (48-22) 532 87 31
  e-mail: prenumerata@okdp.ruch.com.pl
- International Publishing Service Sp. z o.o. ul. Noakowskiego 10 lok. 38
  00-664 Warszawa, Poland, Tel./fax: (48-22) 625 16 53, 625 49 55
  e-mail: books@ips.com.pl

Warunki prenumeraty

Prenumeratę na wszystkie czasopisma wydawane przez IPPT PAN przyjmuje Dział Wydawnictw IPPT. Bieżące numery można nabywać, a także zaprenumerować roczne wydanie Engineering Transactions, bezpośrednio w IPPT PAN,
ul. Pawińskiego 5B, 02-106 Warszawa
Tel.: (48-22) 826 60 22; Fax: (48-22) 826 98 15
e-mail: subscribe@ippt.gov.pl

Wpłaty na prenumeratę przyjmują także regionalne Działy Sprzedaży Prasy RUCH S.A. Infolinia: 804 200 600. Zamówienia można przesyłać pocztą elektroniczną ze strony www.prenumerata.ruch.com.pl

Arkuszy wydawniczych 8.75; Arkuszy drukarskich 7.00
Papier offset. kl. III 80 g.
Skład w systemie LaTeX K. Jezierska

ENGINEERING TRANSACTIONS • *Engng. Trans.* • **59**, 3, 139–159, 2011
Polish Academy of Sciences • Institute of Fundamental Technological Research (IPPT PAN)
National Engineering School of Metz (ENIM)

LIMIT ANALYSIS OF STRUCTURES WITH DESTRUCTIBLE ELEMENTS UNDER IMPACT LOADINGS

P. A l i a w d i n [1)], Y. M u z y c h k i n [2)]

[1)] **University of Zielona Góra**
Prof. Z. Szafrana 1, 65-516 Zielona Góra, Poland
e-mail: P.Aliawdin@ib.uz.zgora.pl

[2)] **Research & Experimental Design State Enterprise for Construction "Institute BelNIIS"**
F. Skoriny 15B, 220114 Minsk, Republic of Belarus

Limit states and identification of structures with shock- or seismic-protected system under dynamic loadings are discussed. Such structures include both the destructible (elastic-brittle) and indestructible (elastic-plastic) elements. A mathematical model and algorithm for solving shakedown problem of bearing capacity of systems with destructible elements are suggested. Next the propagation of vibrations from impacts of Minsk subway trains into nearby skeleton of 9-storied building is investigated. The experimental data for this building are received. Then the propagation of vibrations is analyzed numerically. Finally, a technique of minimax to evaluate dynamic elastic modules of concrete in the considered structure elements is used.

Key words: shock- or seismic-protected system, brittle and plastic elements, limit states, skeleton buildings, subway trains, parameter identification, experiment.

1. Introduction

Protection of buildings and structures from shock and seismic actions is very important. One way of protection is equipment of their load-bearing structures with systems of different elements absorbing the energy of external actions [1–3]. Some elements can be abruptly shut down (elastic-brittle ones), and some can be damaged as a result of plastic flow (elastic-plastic ones). This paper presents a mathematical model, proposed by the first of author, of the limit analysis of systems with destructive elements providing such protection. Next, by the example of 9-storey residential building located near the subway shallow in Minsk, the identification of its computational model is considered [4–11]. Significant sensitivity of stiffness of joints between reinforced concrete columns and floor slabs as a result of dynamic analysis of the building was shown.

The problem of protection of buildings from vibration caused by the movement of subway trains has also lately acquired specific urgency, when at construction of new lines of subway railway, the tunnels of shallow subway have been generally laid. This way of the tunnels laying has technical and economic advantages in comparison with the tunnels at the great depth, and comes to be the basic one at present. However, in the buildings located close to the tunnels of the shallow subway, vibrations achieve such a level that they become perceptible for people being inside [12–14]. To reduce the vibrations, it is necessary to study them in order to efficiently select or create new means of decreasing vibration level in residential and public buildings, being under construction or constructed close to the tunnels of shallow subway [15, 16]. Existing methods of vibration insulation, that use steel springs and vibration absorbers set between the foundation and upstream construction elements, do not take into account the peculiarities of vibration propagation within a building. These methods of the vibration insulation are basically used for the existing buildings.

The remoteness of buildings and constructions from sources of vibration corresponding to norm SNB 3.01.04–02 [17] should make 100 m for railway and 40 m for the shallow subway. In practice, according to [18], about 24% of areas defined above are built up. The organization of such areas is first of all caused by an attempt to reduce a harmful impact of vibration on people and buildings, not resorting to expensive methods of vibration decreasing.

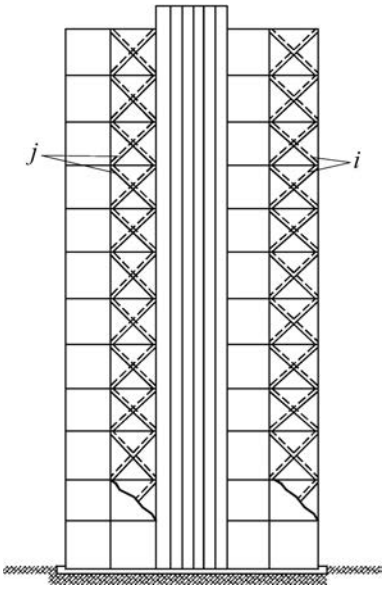

FIG. 1. Scheme of seismic protection of tall building by combined strengthening: i are brittle-destructible ties; j are elastic-plastic ties [19].

Protection of buildings against seismic and shock actions is achieved by equipping them with systems bearing structures of various elements absorbing energy of these actions. As a result, the destruction of the basic structure is prevented. Some elements can be abruptly shut down (elastic-brittle elements), and some damaged as a result of plastic flow (elastic-plastic elements). By the way of illustration these may be ties, guys, fascicles, strands, and other elements which are off in the process of shock or earthquakes.

Two examples of protection systems, for tall building and for nuclear power plant with a seismic isolation foundation and combined elements mounted on the frame, are shown in Figs. 1, 2. It was found [19] that after 5 cycles of plastic deformations and brittle-destructions of protected elements for 8- and 7-intensity scales, the seismic loads on the structures are reduced accordingly by 50% and 30%.

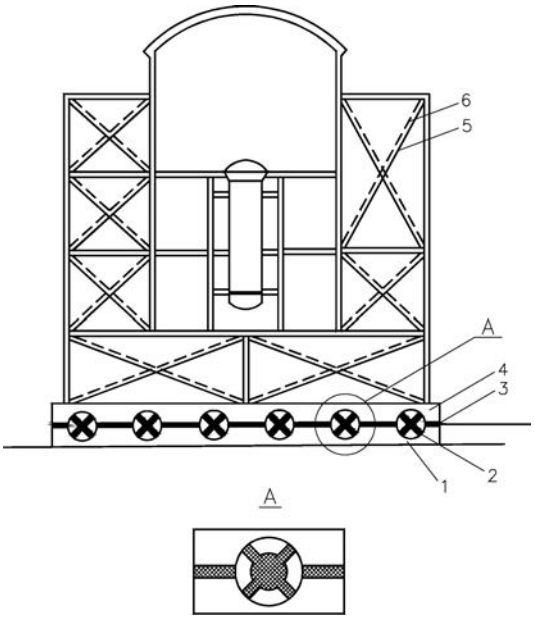

FIG. 2. Basic scheme of reactor with seismic safety foundation and combined strengthening elements on the building frame: 1 is lower foundation plate; 2 are damping supports; 3 is sliding support; 4 is upper foundation plate; 5 are elastic-plastic ties; 6 are brittle-destructible ties [19].

2. A MATHEMATICAL MODEL OF STRUCTURES WITH SHOCK- OR SEISMIC-PROTECTED SYSTEMS

Let us assume the problem of load-bearing capacity of such structures as a generalized dynamic shakedown problem [20–22], taking into account small

system displacements under low cyclic external actions. First we write the FEM equation of motion for a damped discrete elastic system under loading $\mathbf{F}$, expressed in matrix notation, as follows:

$$[M]\,\ddot{\mathbf{u}} + [C]\,\dot{\mathbf{u}} + [K]\,\mathbf{u} = \mathbf{F}, \tag{2.1}$$

where $[M]$, $[C]$, $[K]$ are accordingly structural mass, damping and stiffness matrices; $\ddot{\mathbf{u}}$, $\dot{\mathbf{u}}$, $\mathbf{u}$ are accordingly nodal acceleration, velocity and displacement vectors; $\mathbf{F}$ is a vector of load as a function of time t.

The vector $\mathbf{F}$ belongs to the set $\Omega_{\mathbf{F}}$, described by the vectors of single loadings $\mathbf{F}_j$, $j \in J$; J is a set of single loadings. The set $\Omega_{\mathbf{F}}$ has to include a natural structures stress state $\mathbf{F} = \mathbf{0}$ (i.e. $\mathbf{0} \in \Omega_{\mathbf{F}}$) and generally is nonconvex (grey domain in Fig. 3), [20]. For the purpose of simplification it may be approximated by the convex domain (bordered by firm line in Fig. 3).

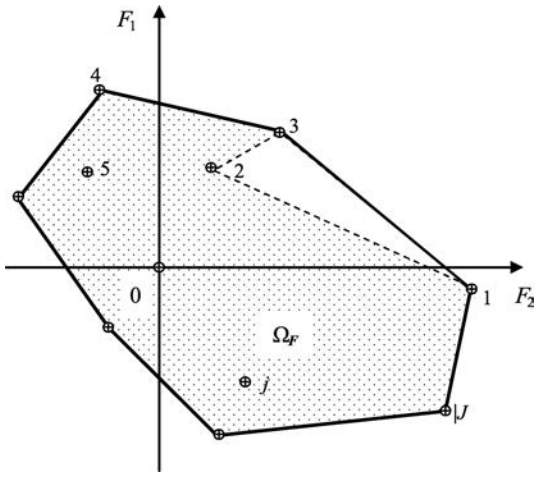

FIG. 3. The set $\Omega_{\mathbf{F}}$ of system loading $\mathbf{F}$, described by the vectors of single loadings $\mathbf{F}_j$, $j \in J$, for $\mathbf{F} \in \mathbf{R}^2$.

The "elastic" solution of Eq. (2.1) is used then as a basis for analysis of real inelastic system. Namely the problem of load-bearing capacity of structures made of perfectly elastic-plastic and elastic-brittle elements, under variable loads, is formulated as follows. Find the vectors of single loadings $\mathbf{F}_j$, $j \in J$, a vector of load $\mathbf{F}$, as well as the vector of residual forces $\mathbf{S}^r = (\mathbf{S}^r_{pl},\ \mathbf{S}^r_{br})$ such, that

$$\sum_{j \in J} \mathbf{T}^T_{\mathbf{F}j} \mathbf{F}_j \to \max, \tag{2.2}$$

$$\boldsymbol{\varphi}_{pl/\Omega\mathbf{F}}(\mathbf{S}^e_{pl} + \mathbf{S}^r_{pl}, \mathbf{K}_{pl}) \leq \mathbf{0}, \tag{2.3}$$

$$\boldsymbol{\varphi}_{br}(\mathbf{S}^e_{br} + \mathbf{S}^r_{br}, \mathbf{K}_{br}) \le \mathbf{0}, \tag{2.4}$$

$$\mathbf{S}^e = \boldsymbol{\omega}_{\mathbf{F}}\mathbf{F}, \tag{2.5}$$

$$\mathbf{A}_{pl}\mathbf{S}^r_{pl} + \mathbf{A}_{br}\mathbf{S}^r_{br} = \mathbf{0}, \tag{2.6}$$

$$\mathbf{S}^r_{br} \ge \mathbf{0}_{br}. \tag{2.7}$$

Here $\mathbf{T}_{\mathbf{F}j}$ are the vectors of weight coefficients corresponding to the vectors of single j-loading $\mathbf{F}_j$, $j \in J$; $\boldsymbol{\varphi}_{pl/\Omega\mathbf{F}}$ are the yield functions, depending on the set $\Omega_{\mathbf{F}}$ external actions (loadings $\mathbf{F}_j$) for elastic-plastic elements; $\boldsymbol{\varphi}_{br}$ are the strength functions for brittle elements; $\boldsymbol{\omega}_{\mathbf{F}}$ is the matrix of loads influence on the elastic forces $\mathbf{S}^e = (\mathbf{S}^e_{pl},\ \mathbf{S}^e_{br})$; $\mathbf{A} = (\mathbf{A}_{pl},\ \mathbf{A}_{br})$ is a matrix of equilibrium Eqs. (2.6). The subscripts pl and br relate to the elastic-plastic and elastic-brittle elements, superscripts e and r – to the elastic and residual forces.

After finding the failure mechanism (active constraints (2.4)) in problem (2.1)–(2.7) one must take into account the dynamic effects of this destruction in iterative procedure [23]. The simple approach to such dynamic analysis was proposed in [24].

Note that the formulated above problem (2.1)–(2.7) for mixed structures with elastic-plastic and elastic-brittle elements is new. In addition to loads $\mathbf{F}_j$, in this problem it is possible to consider the dislocations $\mathbf{d}_j$, $j \in J$, as similar external actions. By changing the dislocation $\mathbf{d}_j$ we can also optimize the state of structures prestressing.

In the particular case of one-pass loading, the problem (2.1)–(2.7) is simplified when $|J| = 1$, this problem is also applicable for the analysis of the progressive collapse of structures [25].

3. Description of the research building nearby the subway tunnels

Investigation of vibration propagation within the building structure caused by the movement of the rolling stock of the subway, have been executed on a residential building being under construction, which is located in the Prityts kiego street in Minsk. This building has five sections (parts), with different number of floors in each section. The first section is completed and has 9 floors. The third section that has 9 floors is at the initial stage of construction: the foundation and 3 floors (at the moment of carrying out of measurements) have been completed. The analysis of parameters of vibration has been executed for the fourth 9-storied section, that is the highest and the most closely located to the subway ($\sim$28 m up to the axis of a tunnel).

Construction works have not been completed at the moment of carrying out the measurements. Works on construction of coating on the 9th floor and the garret floor were performed, what has resulted in a raised level of a vibration background at the moment of carrying out the measurements. The plan of the building divided into sections and the axis location of the subway tunnel line relatively to the building are presented in the Fig. 4.

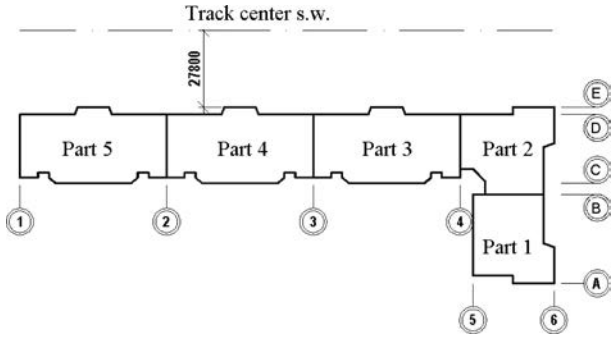

FIG. 4. The plan of the building and location of the subway line axis.

The given section represents monolithic skeleton system with longitudinal and cross-section shear wall, and supported by floor walls made of cell concrete

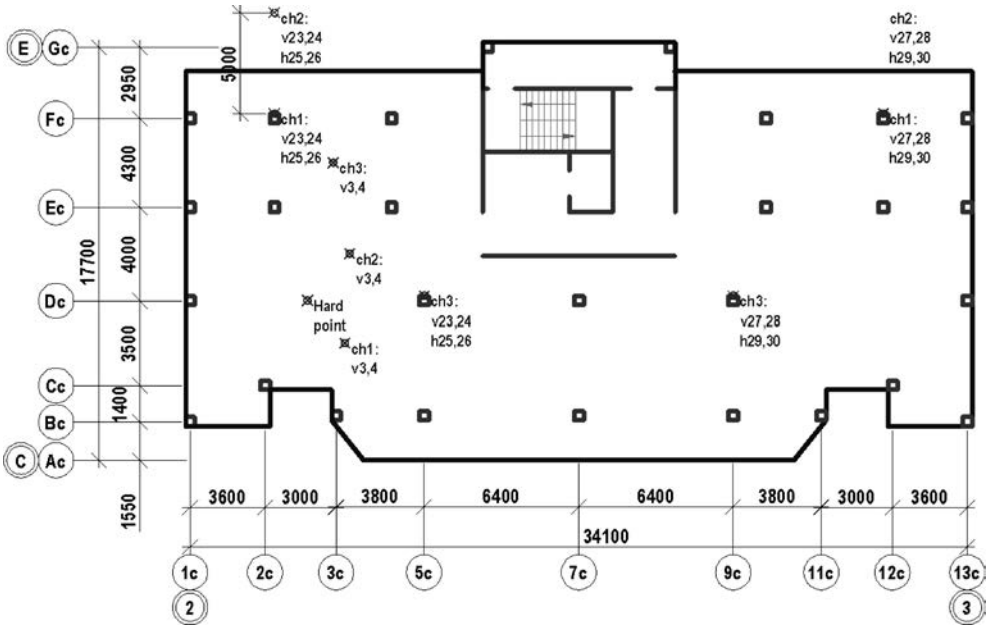

FIG. 5. The constructive scheme of a typical floor of the fourth section of the 9-floor residential unit.

blocks. Floor slabs are monolithic, 200 mm thick, with concealed beam heads. The basement part along the perimeter of the building is made of massive concrete, 400 mm thick. Columns cross-section size is 400×400 mm. The constructive scheme of a typical floor of the fourth section of the 9-storied monolithic-frame residential unit is presented in the Fig. 5.

4. Measurements of vibration for the soil and for the construction foundation

The measurement of vibrations was performed by means of a four-channel measuring system with use of a piezoceramic accelerometer. At passing of the subway trains, the greatest changes of the spectrum were observed in the range of frequencies from 1 to 100 Hz [9]. Measurements of vibration have been taken on the soil in front (∼3.5 m) of the building and in the basement, as well as on the construction elements of the basement part of the building: the shear wall and the columns. Due to the busy schedule of construction works, the total measurements within the whole building were not possible at the moment of measuring. The general layout of measurement points in the basement part of the building is presented in the Fig. 5.

The results of iterative measurements of vibration (not less than 3 hours per each point, an interval of trains movement is about 5 min) are shown in Figs. 6–8. Envelope curve of the narrow-band acceleration spectrum is denoted

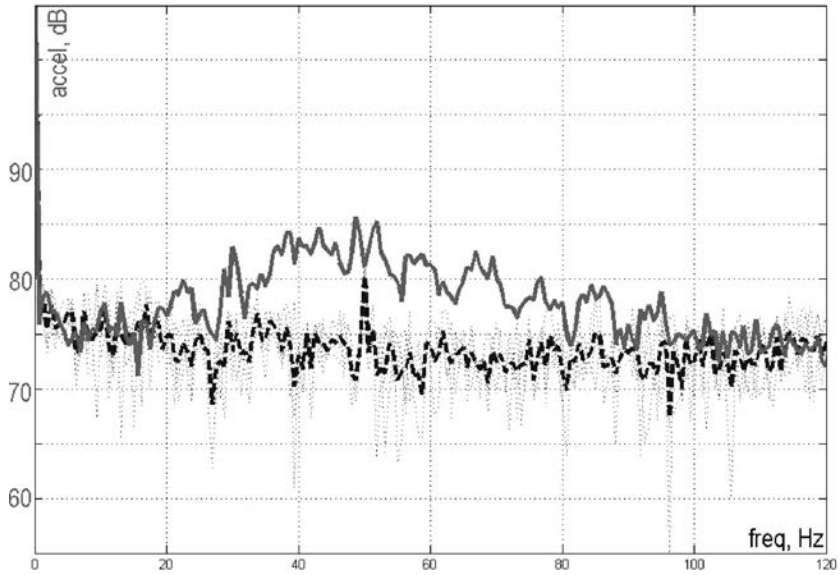

Fig. 6. The spectrogram of vertical levels of vibration of the soil in the point ch1-v23.

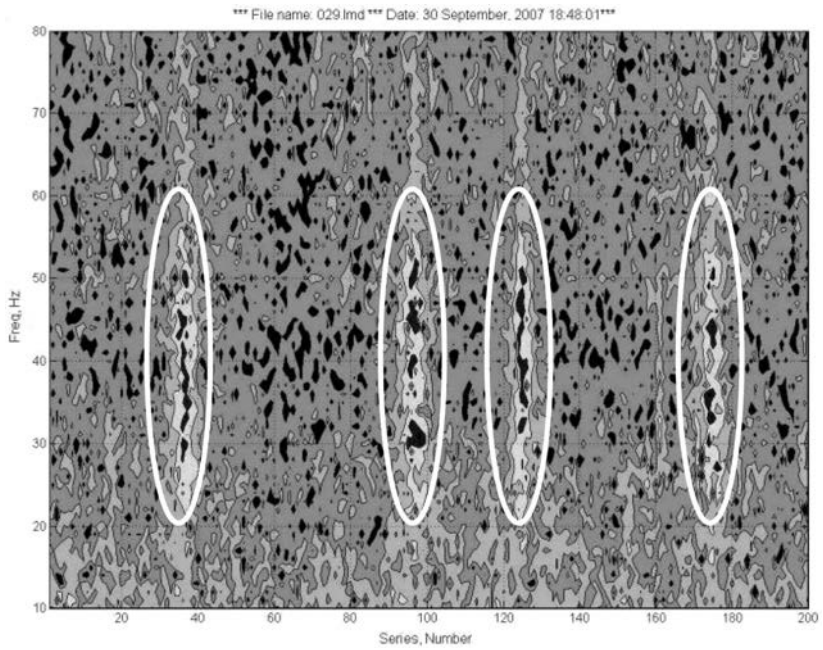

FIG. 7. The spectrogram of horizontal levels of vibration of the soil in the point ch2-h29.

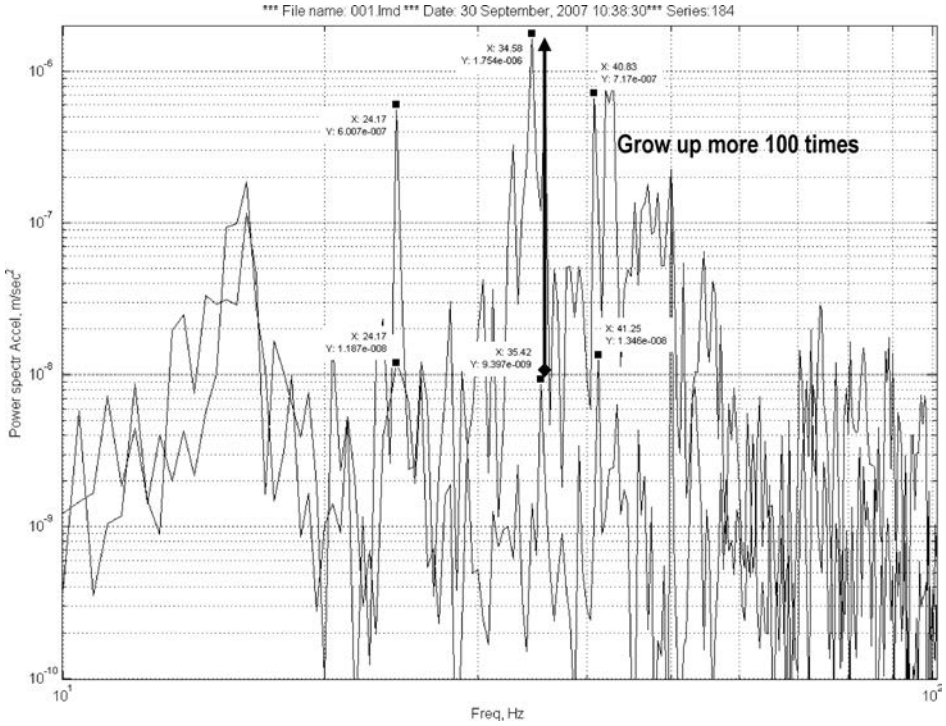

FIG. 8. The spectrogram of vertical levels of vibration of a column in the point ch3-v23.

by a solid line, levels of the background are denoted by a dashed line. The levels L_a of acceleration in these figures,

$$L_a = 20 \cdot \mathrm{Log}_{10}\left(\frac{a}{1 \cdot 10^{-6}}\right), \tag{4.1}$$

are measured in dB; a is acceleration (ref 1E-6), m/s^2.

At passing of subway trains it has been revealed that with the increase in amount of passengers (the rush hour is between 17 and 19 o'clock), the levels of acceleration is 3...3.5 dB higher if compared with the period between 19 and 22 o'clock. Besides, the levels of acceleration depend on the technical state of the railway, the rolling stock, and on the speed of the stock movement (for the rush hours, as a rule, the speed is higher) [13, 26]. All the factors listed above affect the frequency distribution of the levels of acceleration. The peaks of vibration in the range of frequencies of 20 to 60 Hz are displaced in relation to some central frequency (Fig. 8).

At low frequencies, in the range of 1 to 10 Hz, the changes of the levels of acceleration are insignificant in relation to the background and therefore have not been further analyzed.

As a definition of objectively accurate borders of spectral bands for the forced vibration is not obviously possible without total modal analysis, further calculation is performed by means of replacing a real chart of distribution of vibration levels from frequency by a two-level chart (Fig. 9) with a level of 0.001 m/s^2 (60 dB) for the range of frequencies from 1 to 100 Hz and 0.03 m/s^2 (90 dB) for the range of frequencies from 20 to 60 Hz. The calculation is executed by means of the spectral method on a random vibration.

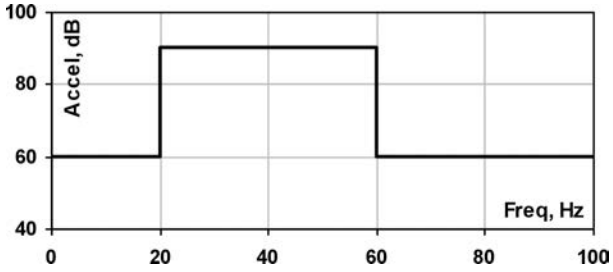

FIG. 9. The spectrum of acceleration for the building calculation on a random vibration.

5. Modelling of vibrations

The modal FEM analysis is used for natural frequencies and mode shapes determination. The Eq. (2.1) of motion for a damped system is as following:

$$[M]\,\ddot{\mathbf{u}} + [C]\,\dot{\mathbf{u}} + [K]\,\mathbf{u} = \mathbf{0}. \tag{5.1}$$

The scheme of the finite elements net of the investigated building fragment is presented in Fig. 10. The shell finite elements of the SHELL63 type are taken here (in the FEA ANSYS) for the slabs and stiffening diaphragms, and bar finite elements BEAM4 for the columns. The total number of elements is 6528.

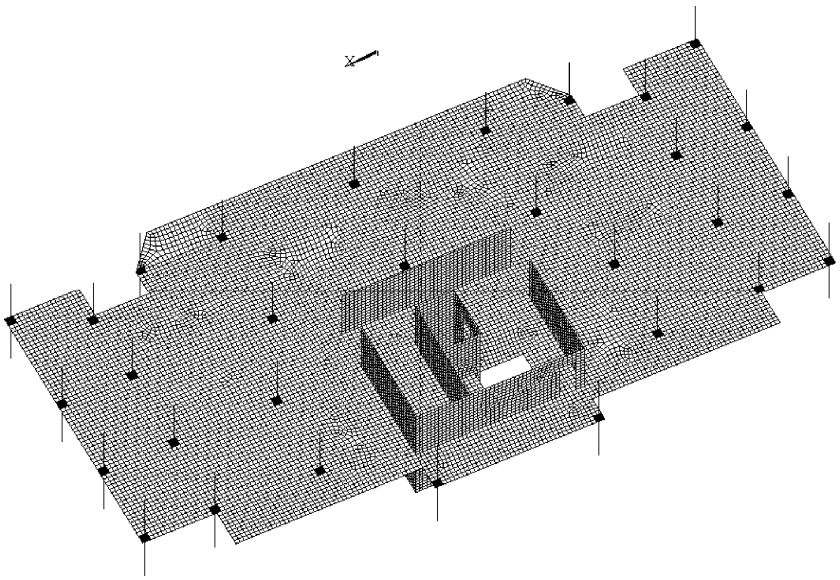

FIG. 10. Design model of the investigated building fragment.

For a linear system without damping, natural vibrations will be harmonic of the form:

$$\mathbf{u} = \boldsymbol{\phi}_i \cos\ \omega_i t, \tag{5.2}$$

where $\boldsymbol{\phi}_i$ is the eigenvector representing the mode shape of the i-th natural frequency; ω_i is the i-th natural circular frequency (radians per unit time); t is time.

After substitution Eq. (5.2) into (5.1), the eigenvalue and eigenvector problem has the form:

$$[K]\boldsymbol{\phi}_i = \lambda_i [M]\boldsymbol{\phi}_i, \tag{5.3}$$

where λ_i is i-th eigenvalue.

This problem is solved here by the block Lanczos eigenvalue extraction method. For each eigenvector $\boldsymbol{\phi}_i$, normalization with the mass matrix is:

$$\boldsymbol{\phi}_i^T [M]\boldsymbol{\phi}_i = 1. \tag{5.4}$$

Then the spectrum analysis is used for the nondeterministic, random vibration method with excitations at the support. In its part, the random vibration method is based on the power spectral density (PSD) approach. The damping ratio is equal to 0.05. The displacement, velocity or acceleration vector for each mode is computed from the corresponding eigenvector taking into account a "mode coefficient":

$$\mathbf{r}_i = \omega_i^2 A_i \boldsymbol{\phi}_i, \tag{5.5}$$

where A_i is spectral acceleration for the i-th mode.

For excitation acceleration of the base we have:

$$A_i = \frac{S_{ai}\gamma_i}{\omega_i^2}, \tag{5.6}$$

where S_{ai} is spectral acceleration for the i-th mode (obtained from the input acceleration response spectrum at frequency $f_i = \omega_i/(2\pi)$ and effective damping ratio ξ_i').

The participation factors, for the given excitation direction (i-th mode), are defined as:

$$\gamma_i = \boldsymbol{\phi}_i [M] \mathbf{D}, \tag{5.7}$$

where $\boldsymbol{\phi}_i$ is eigenvector normalized using Eq. (5.4); $\mathbf{D}$ is a vector describing the excitation direction.

The vector $\mathbf{D}$ has the form:

$$\mathbf{D} = [T]\mathbf{e}, \tag{5.8}$$

where

$$\mathbf{D} = [\, \mathbf{D}_1^a \quad \mathbf{D}_2^a \quad \mathbf{D}_3^a \quad \ldots]^T, \tag{5.9}$$

$\mathbf{D}_j^a$ is excitation at the j-th Degree of Freedom (DOF) in the direction a; a may be either any axis X, Y, Z or rotation about one of these axes;

$$[T] = \begin{bmatrix} 1 & 0 & 0 & 0 & (Z-Z_0) & -(Y-Y_0) \\ 0 & 1 & 0 & -(Z-Z_0) & 0 & (X-X_0) \\ 0 & 0 & 1 & (Y-Y_0) & -(X-X_0) & 0 \\ 0 & 0 & 0 & 1 & 0 & 0 \\ 0 & 0 & 0 & 0 & 1 & 0 \\ 0 & 0 & 0 & 0 & 0 & 1 \end{bmatrix},$$

X, Y, Z are global Cartesian coordinates of a point on the structure space; X_0, Y_0, Z_0 are global Cartesian coordinates of a point about which rotations are done (reference point); $\mathbf{e}$ denotes six possible unit vectors.

For spectrum analysis, the values $\mathbf{D}^a$ may be determined as:

$$\mathbf{D}_X = \frac{S_X}{B}, \qquad \mathbf{D}_Y = \frac{S_Y}{B}, \qquad \mathbf{D}_Z = \frac{S_Z}{B}, \tag{5.10}$$

where S_X, S_Y, S_Z are components of excitation direction; $B = \sqrt{S_X^2 + S_Y^2 + S_Z^2}$.

The modal displacements, velocity and acceleration are combined by complete quadratic combination method to obtain the response of the structure

$$R_a = \left(\left| \sum_{i=1}^{N} \sum_{j=1}^{N} k \varepsilon_{ij} R_i R_j \right| \right)^{1/2}, \tag{5.11}$$

where

$$k = \begin{cases} 1 & \text{if } i = j, \\ 2 & \text{if } i \neq j, \end{cases} \qquad \varepsilon_{ij} = \frac{8\sqrt{\xi_i' \xi_j'} \left(\xi_i' + r\xi_j' \right) r^{3/2}}{(1-r^2)^2 + 4\xi_i'\xi_j'(1+r^2) + 4(\xi_i'^2 + \xi_j'^2) r^2},$$

$r = \omega_j / \omega_i$, $\qquad \xi_{i,j}'$ is effective damping ratio for the mode i, j.

The combined value "Sum",

$$\mathrm{Sum}_i = \sqrt{X_i^2 + Y_i^2 + Z_i^2}, \tag{5.12}$$

is calculated for one node of X, Y and Z displacement.

6. Numerical procedure of parameter identification

Identification of the constitutive parameters holds true for three material constants (modules of concrete elasticity), accordingly E_{p1} for slab, E_{p3} for joint slab with column and E_c for column (Fig. 10), which combine into a vector of parameters of system $\mathbf{x} = (E_{p1}, E_{p3}, E_c) \in \mathbf{R}^n$, $n = 3$.

Criterion of a minimax identification of system in terms of [27, 28],

$$\rho(\mathbf{x}) = \max_{i \in I} \left| \frac{f_{mi} - f_{ci}(\mathbf{x})}{(f_i^+ + f_i^-)/2} \right|, \tag{6.1}$$

has to minimize under Eq. (5.1), and known initial conditions, where f_{mi} are measured values of i-th natural frequencies, $f_i = \omega_i/(2\pi)$, $i \in I$; I is a set of analyzed frequencies; $f_{ci} \equiv f_{ci}(\mathbf{x})$ are values of i-th natural frequencies, calculated from Eq. (5.1) and known initial conditions, depending on the vector $\mathbf{x}$; f_i^+, f_i^- are accordingly high and low values of i-th natural frequencies of vibration given by the designer. Three natural frequencies were investigated here, $|I| = 3$.

As far as the identification of system is an ill-posed problem, criterion of optimality (6.1) is modified

$$\rho_\alpha(\mathbf{x}) = \rho(\mathbf{x}) + \alpha \|\mathbf{x}\|^2, \tag{6.2}$$

where α is a Tikhonov regularization parameter [29], $\alpha > 0$; $\|\mathbf{x}\| = \sqrt{\sum_{i\in 1:n} (x_i^2)}$.

Choice of regularization parameter α on k-step of calculations process, $k = 0, 1, \dots K$, was made by the formula

$$\alpha_k = \alpha_0 q^k, \qquad q > 0. \tag{6.3}$$

The next parameter α_{k+1} is found from the following $(K+1)$-th problem:

$$\left\|\mathbf{x}_{\alpha_{k+1}} - \mathbf{x}_{\alpha_k}\right\| \to \min_{k\in 0:K}, \tag{6.4}$$

up to the comprehensible accuracy of solving an initial problem (6.2).

The received optimum vector $\mathbf{x}^*$ of parameters of the investigated 9-storied building contains the following values of modules of concrete elasticity: for the slabs $E_{p1} = 30.24$ GPa (reduction of the reference modulus by 19.05%) and for the columns $E_c = 47.54$ GPa (increment the reference modulus for 18.85%). Change of modulus of concrete elasticity for the joints of slabs with columns E_{p3} comes to 5.3 times. Comparison of natural frequencies of the fragment vibration, found by reference with the results of measurements, is shown in Table 1.

Table 1. The optimum parameters of building constructions received by decision of the identification problem for the investigated fragment.

The parameter name	Reference values	Optimum values	The measured values
Modulus of concrete elasticity, Pa			
E_{p1} (slab)	3.6E+10	3.024E+10	–
E_c (column)	4.0E+10	4.754E+10	–
E_{p3} (slab in region joint with column)	3.6E+10	1.911E+11	–
Natural frequencies of vibration for investigated fragment, Hz			
FREQS04	17.877	16.601	16.25
FREQS13	26.554	23.428	24.17
FREQS24	35.748	34.582	35.00
Parameters of system optimality on Eqs. (6.1)–(6.4)			
TST	0.136	0.397E-01	–
TST1	0.91E-2	0.456E-03	–
TST2	0.88E-2	0.972E-03	–
TST3	0.45E-3	0.144E-03	–

The difference between reference, optimum and measured values of natural frequencies is small, but it leads to the distinction in kind of vibration forms, as is shown in Fig. 13 for the frequencies of 40.682 Hz and 40.721 Hz accordingly.

7. Analysis of constructure vibration

A typical feature of the vibration of construction elements for the four sections of the 9-storied building model for the range of frequencies from 0 to 10 Hz at calculation for a random vibration (the propagation of the basis by a random force is set by means of a spectrum of acceleration of bearers), is a prevalence of the horizontal component of displacement above the vertical one. Natural frequencies of construction vibrations for the range of frequencies from 0 to 10 Hz are presented in the Table 2.

Table 2. Natural frequencies of vibrations for the range from 0 to 10 Hz.

No	1	2	3	4	5	6
Frequency, Hz	1.72	2.38	3.23	5.84	9.07	9.73

It is necessary to note that at low frequencies, the greatest contribution to the process of the building vibration is introduced by the horizontal component along the axis Y-Y or X-X, but with the increase in frequency, the greatest contribution to the vibration process is introduced by the vertical component of vibration, along the axis Z-Z.

The distributions of the vibration accelerations (Sum_a, see Eq. (5.12)) over construction elements of the model for the ranges of frequencies accordingly 0–20, 20–40, 40–60 Hz by calculation for a random vibration, are presented in Figs. 11a-c. The distribution of vibration accelerations in the vertical plane Z-Z over construction elements of the model, for the range of frequencies from 0 to 20 Hz by calculation for a random vibration, is presented in the Fig. 12.

The numbers of forms of normal vibration frequencies for the specified foregoing ranges are presented in the Table 3.

Table 3. Natural vibrations frequencies of the model of the building.

Frequency, Hz	0–20	20–40	40–60	60–80
Number of eigenvalues	186	278	287	278

The analysis of normal frequencies and forms of vibration in the range of frequencies from 1 to 60 Hz shows that components of horizontal displacement prevail over the vertical ones for the lowest frequencies between 1 and 7 Hz.

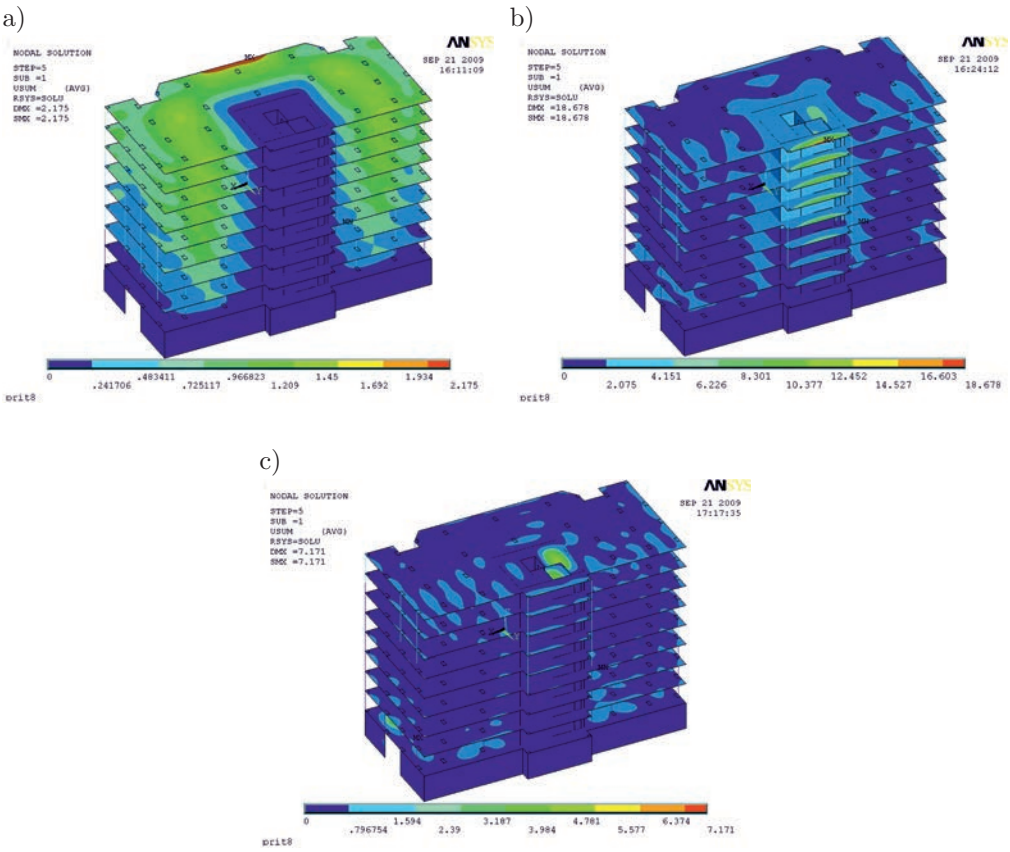

FIG. 11. Vibration accelerations (Sum) of construction elements by calculation for random vibration: a) for the range of frequencies, from 0 to 20 Hz; b) the same, from 20 to 40 Hz; c) the same, from 40 to 60 Hz.

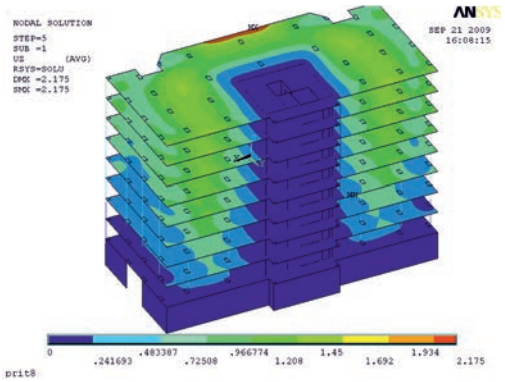

FIG. 12. Vibration accelerations of construction elements (Z-Z) by calculation for random vibration for the range of frequencies, from 0 to 20 Hz.

With the increase in frequency, the vertical component of vibration becomes a prevailing component in the vibrating mode. Therefore, the vibration analysis of the rolling stock of the subway is considered mainly in a plane of floor disks for 1–9 floors.

The proportion of the maximal amplitudes for the displacements of construction elements (Sum:Z:Y:X, related to displacement Sum) for different forms of normal vibration in the range of frequencies from 1 to 60 Hz are presented in the Table 4. The maximal amplitudes of displacement specified in this table along X, Y and Z axes are presented for various nodes of the model within the limits of one form of vibration; however the value "Sum" is defined for the node with the maximal displacement defined by the Eq. (5.12).

Table 4. Proportion of the maximal amplitudes for the displacements along the orthogonal axes *X*, *Y*, *Z*.

Frequency, Hz	Sum	Z	Y	X
1.72	1.00	0.13	0.21	0.98
2.38	1.00	0.10	0.79	0.48
3.23	1.00	0.31	0.85	0.72
5.84	1.00	0.33	0.60	0.84
9.07	1.00	0.34	0.50	0.90
9.73	1.00	0.99	0.64	0.75
11.02	1.00	1.00	0.12	0.08
20.13	1.00	1.00	0.67	0.02
35.01	1.00	1.00	0.29	0.10

A building being under construction gives a possibility of free planning. As a result, there can appear areas with significant levels of vibrations in case the cross-walls are irrationally placed. Occurrence of low-frequency noise in empty accommodations (the effect of rumbling) is also possible. It is determined that areas with excessive vibration can be formed on any floors of a building, from the 1st to the 9th. At various forms of normal vibrations of construction elements, the areas stated above can be present on different floors. For example, for the frequency of 40.682 Hz, the maximal displacement of the floor is formed on the 9th floor, and for the frequency of 40.721 Hz is on the 3rd floor (Fig. 13).

The calculation has shown that occurrence of such areas is possible for any range of frequencies, even in the areas limited by rigid elements (low deformable elements in the vertical plane relatively to the bending of the floor): staircase, shear wall, column.

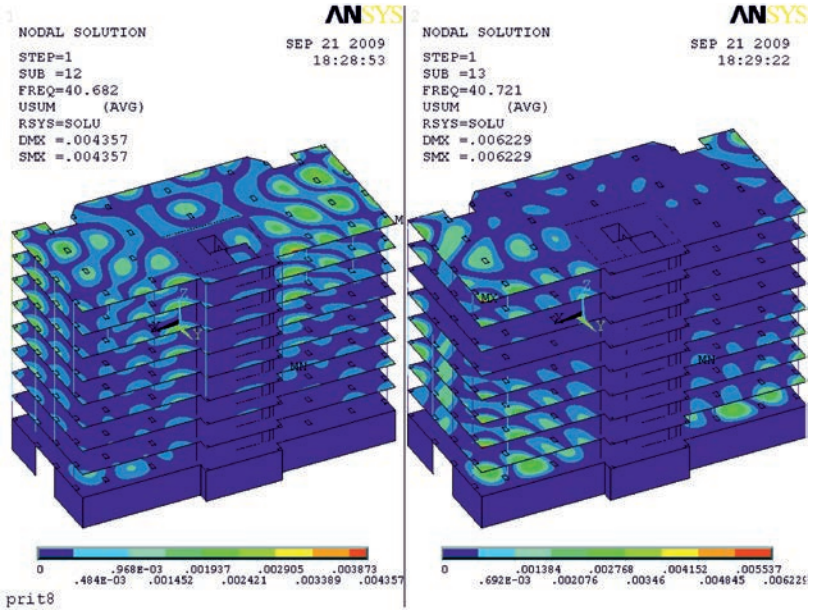

FIG. 13. Location of areas with the maximal vibration accelerations on different floors, corresponding to different forms of vibration.

The vibration of construction elements for the same nodes, located on the vertical line between the 1st and 9th floors and caused by random acceleration of the foundation from the external impact with a set function of spectral density for various frequency ranges, has been investigated. Results of calculation are presented in the Fig. 14.

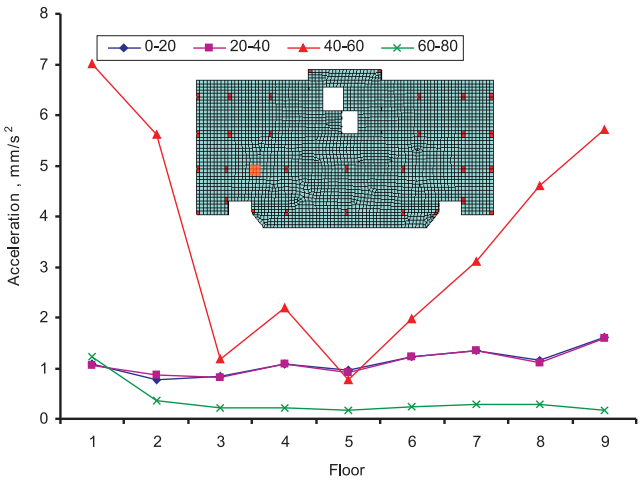

FIG. 14. The graph of change of the acceleration amplitude by the floors in the nodes, coinciding vertically.

The graphs of maximal amplitude of constructions acceleration for the floor disk and shear wall, calculated for the different ranges of frequencies, are presented in Figs. 15 and 16 accordingly. The levels of vibration essentially differ only for the range of frequencies from 20 to 60 Hz; for the range of frequencies from 0 to 20 Hz, the acceleration of the floor disks between 1st and 9th stories changes insignificantly and, on the whole, is presented by a horizontal line.

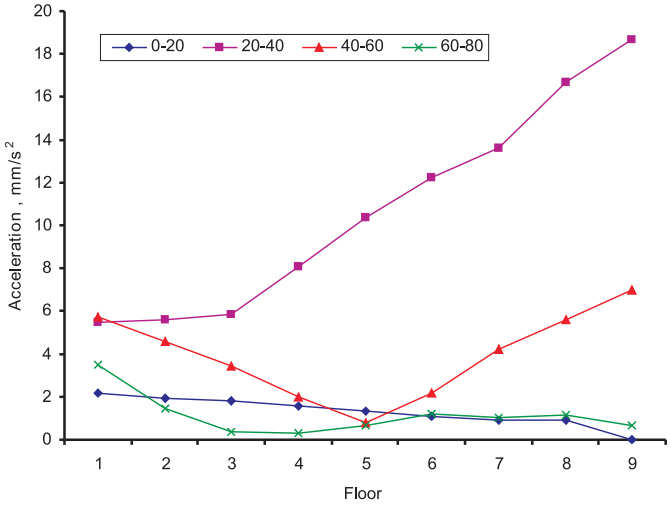

FIG. 15. The graph of change of acceleration amplitude by the floors in nodes with the maximal amplitude of acceleration.

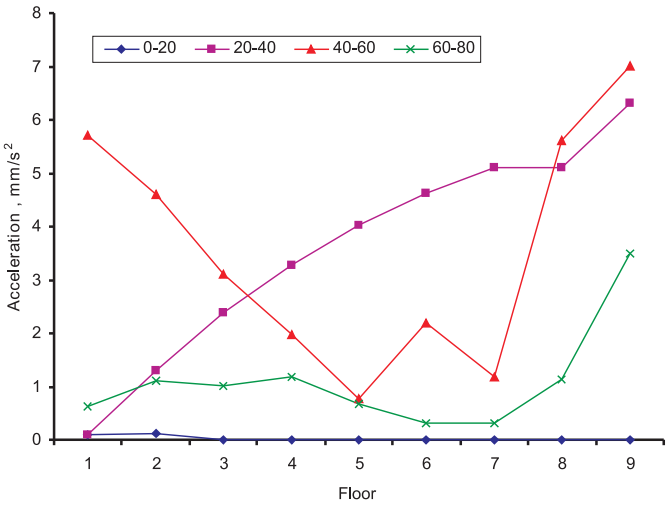

FIG. 16. The graph of change of acceleration amplitude by the shear wall in nodes with the maximal amplitude of acceleration.

8. Conclusions

A mathematical model and algorithm for solving of the problems of bearing capacity of shock- or seismic-protected systems with destructible elements are suggested.

A technique of minimax to evaluate dynamic elastic modules of concrete for the skeleton 9-storied building, which is located nearby Minsk subway tunnel, was used.

The greatest acceleration obtained for the shear wall of the investigated 9-storied building corresponds to the range of frequencies of 20–60 Hz, practically for all floors. The highest levels of acceleration of the floor disk are obtained for the 1st, 8th and 9th floors, and therefore at measurements, modal analysis and development of constructive actions, it is advisable to perform a more complete investigation on distribution of vibration over the construction elements in the above-mentioned range of frequencies.

The changes of model parameters as a result of identification for concrete elasticity modules are equal to about 20% for the slabs and columns, whereas for the joints of slabs with columns this change comes to more than 5 times. Consequently, the initial design model of the structure has to be modified, for example, by installing rigid inclusions in the joints of slabs and columns.

References

1. M. Y. H. Bangash, T. Bangash, *Explosion-resistant buildings: Design, analysis and case studies*, Springer, Berlin, Heidelberg, New York, 2006.

2. *Handbook on Vibration Induced Deformations and Accidental Loads*, Boverket, Swedish Board of Housing, Building and Planning, 1994.

3. U. Starossec, M. Wolf, *Design of collapse-resistant structure*, *Robustness of Structures*, Proceedings of Workshop, JCSS & IABSE, 1, Garston, Watford, UK, 2005.

4. P. Aliawdin, Y. Muzychkin, *Vibration of skeleton constructions elements caused by trains of the shallow subway*, Proceedings of the 9th International Conference Modern Building Materials, Structures and Techniques, Vilnius, Lithuania, Technika, **3**, 865–872, 2007.

5. A. Cunha, E. Caetano, *Experimental modal analysis of civil engineering structures*, Journal of Sound and Vibration, **40**, 6, 12–20, 2006.

6. H. H. Hung, Y. B. Yang, *A review of researches on ground-borne vibrations with emphasis on those induced by trains*, Proceedings Nat. Sci. Council. Part A. Physical Science and Engineering, **25**, 1, 1–16, 2001.

7. M. Mickaitis, V. J. Stauskis, *Vibration transmission through joints of walls and columns in frame buildings*, Journal of Civil Engineering and Management, **11**, 3, 185–191, 2005.

8. W. Mironowicz, J. Rządkowski, W. Sawicki, *Application of dynamic diagnostics in the analysis of damage of historic building* [in Polish], Inżynieria i Budownictwo, **2**, 92–96, 2010.

9. M. D. Trifunac, S. S. Ivanovic, M. I. Todorovska, *Wave propagation in a seven-story reinforced concrete building: III. Damage detection via changes in wavenumbers*, Soil Dynamics and Earthquake Engineering, **23**, 1, 65–75, 2003.

10. T. Uhl, *Computer-Aided Identification of Constructional Models* [in Polish], WNT, Warszawa, 1997.

11. T. Uhl, W. Lisowski, W. Bochniak, *Problems of tuning the finite element models* [in Polish], Akademia Górniczo-Hutnicza, Kraków, 2000.

12. R. Ciesielski, A. Kwiecień, K. Stypuła, *Wave propagation in surface layers of foundation soil: experimental data "in situ"* [in Polish], Politechnika Krakowska, Kraków, 1999.

13. J. Kawecki, K. Stypuła, *Errors in vibration forecasts and diagnoses concerning evaluation of dynamic influences on buildings* [in Polish], Technical Journal, Wyd. Politechniki Krakowskiej, Poland, Kraków, 1-M, 127–136, 2008.

14. K. Stypuła, *Vibrations caused by operation of urban rail transport – investigations and prevention* [in Polish], Transport Miejski i Regionalny, **10**, 2–11, 2006.

15. L. Kruszka, R. Rekucki, *Experimental analysis in situ of structural-building elements response on random excitation* [in Polish], Proceedings of the 12th Theoretical Foundation of Civil Engineering, pp. 257–268, Warsaw, Poland, 2004.

16. M. Nader, J. Różowicz, J. Korzeb, E. Purta, *Selected problems of Warsaw subway action on buildings* [in Polish], Politechnika Radomska, Transport, **23**, 3, 361–366, 2005.

17. *SNB 3.01.04-02. Urban planning. Design and building of settlements* [in Russian], Design Code of Belarus, 2003.

18. I. A. Kudryavcev, *Influence of vibrations on building foundations* [in Russian], Homel, BelGUT, 1999.

19. A. V. Minasian, *Bearing capacity reserves of seismic-protected systems in terms of energy viewpoint* [in Russian], Proceedings of the International Conference "Actual problems of research on the theory of structures", Moscow, V. A. Kucherenko, TSNIISK, **1**, 270–276, 2009.

20. P. Aliawdin, *Limit analysis of structures under variable loads* [in Russian], Technoprint, Minsk, 2005.

21. J. A. König, *Shakedown of elastic-plastic structures*, PWN, Warszawa, Elsevier, Amsterdam, 1987.

22. G. Maier, *Upper bounds on deformations of elastic-workhardening structures in the presence of dynamic and second-order effects*, J. Struct. Mech., **2**, 265–280, 1973.

23. P. Alyavdin, *Shakedown analysis of effective bearing structures with unsafe members under dynamic loading*, Proceedings of the 5th International Conference Modern Building Materials, Structures and Techniques, Vilnius, Technica, **2**, 167–172, 1997.

24. G. A. Geniev, V. I. Kolchunov, N. V. Klyueva, A. I. Nikulin, K. P. Pyatikrestovsky, *The strength and deformability of reinforced concrete structures under over-design influences* [in Russian], Moscow, Izd-vo of Association of Building Universities, 2004.

25. B. R. Ellingwood, R. Smilowitz, D. O. Dusenberry, D. Duthinh, H. S. Lew, N. J. Carino, *Best practices for reducing the potential for progressive collapse in buildings*, National Institute of Standards and Technology, Technology Administration, U.S. Department of Commerce, 2007.

26. J. Kawecki, *Diagnostics of communication vibration on the buildings and people in the buildings* [in Polish], Transport Miejski i Regionalny, **11**, 17–27, 2006.

27. V. F. Dem'anov, G. E. Stavroulakis, L. N. Polyakova, P. D. Panagiotopoulos, *Quasidifferentiability and Nonsmooth Modelling in Mechanics, Engineering and Economics*, Nonconvex Optimization and Its Applications, 10, Kluwer Academic Publishers, Dordecht/Boston/London, 1996.

28. A. Tarantola, *Inverse problem theory and methods for model parameter estimation.* Library of Congress Cataloging-in-Publication Data, Society for Industrial and Applied Mathematics, Philadelphia, 2005.

29. A. N. Tikhonov, V. A. Arsenin, *Solution of ill-posed problems*, Winston & Sons, Washington, 1977; [in Russian], Moscow, 1974.

Received December 18, 2010; revised version June 10, 2011.

ENGINEERING TRANSACTIONS • *Engng. Trans.* • **59**, 3, 161–196, 2011
Polish Academy of Sciences • Institute of Fundamental Technological Research (IPPT PAN)
National Engineering School of Metz (ENIM)

REVERSE BALLISTIC IMPACT STUDIES OF THIN PLATE PERFORATION

L.C. Forde[1,2)], W.G. Proud[1)], S.M. Walley[1)], P.D. Church[3)], R. Cornish[3)]

[1)] **Fracture and Shock Physics Group**
Cavendish Laboratory
J.J. Thomson Avenue, Cambridge CB3 0HE, United Kingdom

[2)] **Measurement Standards Laboratory**
New Zealand

[3)] **QinetiQ**
Fort Halstead
Sevenoaks, Kent TN14 7BP

Full-scale ballistic experiments using tungsten rods and rolled homogeneous armour (RHA) steel plates are expensive to perform. For this reason, a study has been performed into the possibility of using less expensive, more easily available metals in small-scale laboratory experiments. The metal pairs chosen listed in order as armour/penetrator materials were: RHA steel/tungsten, dural/mild steel, and copper/aluminium. In order to be able to use as many diagnostics as possible (including high speed photography, VISAR, stress gauges) the reverse ballistic configuration was used. This configuration also allowed the determination of the high rate, low strain mechanical properties of mild steel to be determined. Finally, a comparison was made between experiment and numerical predictions made using a modified Armstrong-Zerilli constitutive model for the RHA steel/tungsten pair. The model was found to underpredict the penetration, probably because failure mechanisms were not incorporated.

1. Introduction

1.1. Background to this study

A vast literature with a long history exists on the subject of terminal ballistics, and publications in this area show no sign of slowing, particularly with the recent improvements in hydrocode modelling.

The experimental data obtained in the field of terminal ballistics generally consists of the following parameters:

(i) velocity and trajectory of projectile prior to impact,
(ii) velocity and trajectory of projectile after impact,
(iii) masses, velocities and trajectories of fragments generated by the impact process,
(iv) motion imparted to the target,
(v) hole size in and mass loss from the target,
(vi) shape and dimensions of the recovered projectile.

From these observations the nature of the penetration mechanisms and projectile deformation can be inferred. These can be plotted as a mechanism map [1] in a manner similar to Ashby deformation maps [2]. The ballistic limit velocity (i.e., that required for perforation) may also be determined from such experiments. Penetration mechanics is complicated when the deformation due to impact includes the rear surface of the target [3].

1.2. Methods of study

Because we wished to use as many diagnostics as possible in order to constrain and exercise material constitutive models, we decided to perform reverse ballistics studies on instrumented rods. Despite its many advantages in terms of ease of instrumentation, the reverse ballistic configuration has a number of drawbacks, including limitations on (i) the diameter of the target to that of the available gun barrel, and (ii) the mass of the target (the heavier the target the slower it can be fired). Also the movement of the target plate across the field of view inevitably creates parallax.

The technique we used in all the experiments reported here was high-speed photography. As debris clouds and fracture can obscure the target to optical photography, we also performed single-frame X-ray flash radiography (sometimes combined with speckle analysis). These studies have been reported elsewhere [4, 5].

Instrumentation of reverse ballistic impacts by, for example, foil stress gauges permits the acquisition of a force history [6]. Stress histories may also be recorded using VISAR (Velocity Interferometer System for Any Reflector), a laser interferometer system that measures the particle velocity produced by an in-material stress pulse incident on a free surface [7]. Depending on the application, this may be more convenient than embedded foil gauges. We used both techniques in this study.

1.3. Why perform model ballistic experiments?

Penetration models are necessary in the development of both armour and projectiles. In seeking to conduct experiments to enhance understanding, the

designers of projectiles or targets can change: (a) the configuration, e.g., plate thickness, plate spacing, reactive armour, projectile length, projectile nose shape, segmentation of rod; (b) the material, e.g., ductility, toughness, yield strength; and (c) the magnitude and direction of motion.

For example, some strategies used to protect a space include:

(i) deflecting the penetrator by angling the armour [8, 9] (this also has the effect of increasing the target thickness along the projectile trajectory);

(ii) fracturing or eroding the penetrator by (a) placing very hard ceramic plates at the front [10] or (b) moving the front plate very fast across the projectile trajectory using explosives (reactive armour) [11];

(iii) dispersing the rod fragments by spacing the target plates [12–14].

Attempts to counter these strategies include:

(i) increasing the penetrator length so that a sufficient length remains after erosion to perforate the target [15];

(ii) designing the penetrator so that different sections have different properties [16], e.g., making the nose hard, dense and blunt so as to load the target as severely as possible on impact while making the rear more ductile to reduce the likelihood of fragmentation due to bending stresses;

(iii) increasing the impact velocity so as to stress the target more severely [17].

The wide variety of types of ballistic impact means that there is no optimum configuration of materials to suit all situations [18]. Hence, the best armour design for defeating shaped-charge jets will probably not be the most efficient at resisting long rod penetrators [19, 20].

Experimental testing can be performed in three different ways:

(i) full-scale – this is expensive and not ideal for exploring a large set of experimental parameters. The diagnostics that can be deployed may also be limited on an outside range;

(ii) small-scale – the main advantages being that fabrication, machining and assembly of equipment are much easier on a small scale. Experiments are also easier to perform within a laboratory where the experimental parameters can be more easily explored and a wide range of diagnostics used. The main disadvantage is that scaling up to full-scale may not be straightforward [21, 22];

(iii) material property testing – since the penetration process takes place in several different phases [23–25], experiments characterising the material response to each of the various different modes of loading (e.g., shock propagation, adiabatic shear, dynamic fracture) need to be carried out. Such experiments should be compared with appropriate constitutive models using numerical modelling.

2. Experimental

The experiments reported in this paper consisted of impacts between long rods and thin metal plates. Such plates allow the behaviour of the rear face of the target to be observed using high-speed photography, but other aspects of penetration (such as ricochet, ballistic limits, rod erosion and the influence of the length/diameter (L/D) ratio on penetration depth) cannot be studied. Also deformation of a thin plate is restricted to a small region surrounding the impact point. The holes formed in the plates were found to be cylindrical and to have contracted after impact as rods recovered after impact were unable to fit through them.

The aspect ratio of the rods studied ($L/D \geq 10$) was determined by the requirement to be able to instrument them with stress gauges. Previous studies have shown that gauges should be placed at least ten diameters from the impact end to improve the approximation to uniaxial stress conditions [26, 27]. In order to instrument the rods, the target had to be fired at the rods (reverse ballistics) [28] (see Fig. 1). The gun used was primarily built for plate impact studies [29].

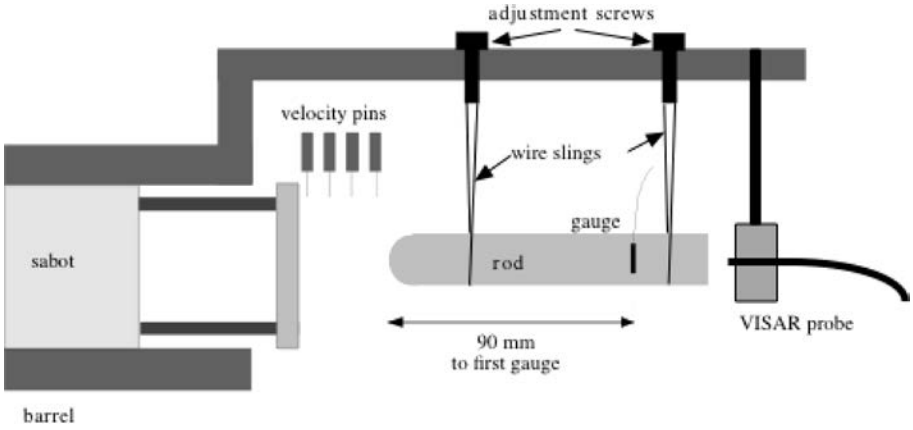

Fig. 1. Schematic diagram of the reverse ballistic set-up used in these experiments [28].

Annealed copper and tungsten alloy rods with hemispherical ends and with diameter 10 mm and length 100 mm were supplied by QinetiQ. 9.5 mm diameter mild steel rods were sourced locally and typically used in lengths of 215 mm (or occasionally 340 mm) with either hemispherical or flat ends. The properties of all the materials used are listed in Table 1. Pure aluminium and RHA steel plates were supplied by QinetiQ for impact by the copper and tungsten alloy rods respectively, whereas a work-hardened aluminium alloy (dural) was used with the mild steel rods. The ratios of the rod-to-plate densities and rod-to-plate yield strengths are given in Table 2.

Table 1. Properties of the materials used in these experiments.

	Tungsten alloy (Densimet 176 FNC)	Pure copper (XM C103)	Mild steel (EN3B)	Dural (AA6082-T6) fully hardened	Rolled Homogeneous Armour (RHA) Steel (UK 100)
Chemical composition [wt. %]	W: 92.3, Ni: 4.92, Fe: 1.45, Co: 1.40		Fe: 98.9, Cu: 0.2, Mn: 0.9		
Density $\widetilde{\rho}$ [kg m^{-3}]	17560 ± 20	8924 ± 1	7818 ± 6	2703 ± 5	7824 ± 5
Longitudinal elastic wave speed c_L [m s^{-1}]	5190 ± 5	4760 ± 5	5913 ± 5	6400 ± 5	5905 ± 5
Transverse elastic wave speed c_T [m s^{-1}]	2850 ± 5	2330 ± 5	3248 ± 2	3150 ± 5	3239 ± 5
Rod elastic wave speed c_R [m s^{-1}]	4570 ± 20	3820 ± 20	5200 ± 10	5160 ± 20	5190 ± 30
Bulk elastic wave c_B [m s^{-1}]	4010 ± 10	3930 ± 10	4571 ± 8	5270 ± 10	4570 ± 10
Young's modulus E [GPa]	366 ± 2	130.1 ± 0.7	211.8 ± 0.6	71.9 ± 0.3	211 ± 1
Shear modulus μ [GPa]	142.6 ± 0.4	48.5 ± 0.1	82.5 ± 0.1	26.82 ± 0.08	82.1 ± 0.2
Bulk modulus K [GPa]	283 ± 1	137.6 ± 0.5	163.4 ± 0.5	75.0 ± 0.2	163.4 ± 0.6
Poisson's ratio ν	0.284 ± 0.006	0.342 ± 0.006	0.284 ± 0.004	0.340 ± 0.005	0.285 ± 0.006
Dynamic yield stress σ_y [GPa]	2.05 ± 0.1	0.4 ± 0.1	0.93 ± 0.02	0.30 ± 0.05	1.44 ± 0.05

Notes on the provenance of this data: The yield stresses of all materials were measured in-house using a split Hopkinson pressure bar. The longitudinal and transverse sound speeds as well the density and yield stress were measured in- house for all the materials except copper, the data for which were obtained from the LASL Shock Hugoniot Data Book [30]. Other properties that depend on these were calculated.

Table 2. Ratios of properties of rods to properties of plates.

Plate/rod pairs	Rod density/plate density	Rod yield stress/plate yield stress
Pure aluminium/copper	3.3	2.1
RHA steel/tungsten alloy	2.2	1.4
Dural/mild steel	2.9	3.2

A consequence of the rod lengths chosen was that the time taken for an elastic wave to travel to the far end of the rod and return was often long compared to the duration of the high-speed photographic sequences taken. This meant that the nose of the rod remained nearly stationary during photographic observation except for when significant plastic deformation (shortening) occurred in the rod.

As the diameter of the gun barrel used is 50 mm the rod diameter needed to be significantly less than this so as to reduce edge effects during impact. The minimum time before the edge of the metal target plate could have an influence is the time for an elastic wave to travel from its centre out to the mounting pillars and back (a distance of about 20 mm; see Fig. 2), i.e., around 6 μs. The diameter of the rods also needed to be larger than the stress gauges used (*ca.* 3 mm) and to be large enough to give reasonable photographic resolution. A diameter of 10 mm was settled on as meeting these various requirements.

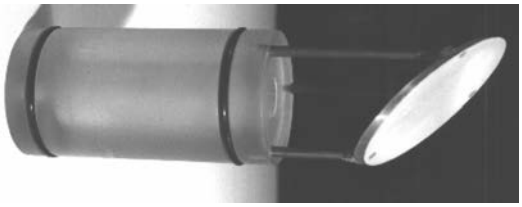

FIG. 2. Photograph of a 3 mm thick plate mounted at 45° on the front of a 50 mm diameter polycarbonate sabot.

The parameters investigated were: velocity, plate thickness, angle of impact, nose shape, and material. The choice of materials was influenced by the desire to observe the effect of a range of properties (ductility, density, work-hardening) while also trying to keep the ratio of the projectile/target properties as close as possible to that of tungsten/RHA armour steel. This led to the choice of the following pairs: annealed copper with annealed aluminium, mild steel and work-hardened dural, tungsten/RHA steel. For these pairs, the ratio of rod density to plate density varied between 2.2 and 3.5 and the ratio of yield strengths varied between 1.4 and 3.2 (see Tables 1 and 2). These combinations ensured a variety of perforation mechanisms could be observed.

The plates were thin enough that their rear surface exerted a mechanical influence for most of the perforation process. Specifically, the thicknesses of the

aluminium plates used were 5 mm and 10 mm, the RHA plates 5 mm, and the dural plates 3, 6 and 10 mm. The plates were mounted at three different angles to the rod axis (90°, 45° and 30°) onto a polycarbonate sabot using three slender steel pillars near the edges (Fig. 2). The plates were glued onto the pillars with metal-filled epoxy. The centre of the forward-facing face of the sabot was recessed to reduce post-impact damage.

All the high-speed sequences were taken using an FS501 Ultranac camera using back illumination from a flash tube. There are a number of issues to be considered in the interpretation of the sequences. First, the motion of the plate in the field of view means that the viewing angle changes (parallax). Also because the images were taken in silhouette, the front and back surfaces were not illuminated and thus the plate appears to change thickness during the sequence (compare the beginning and end of the sequence shown in Fig. 3). This reduces

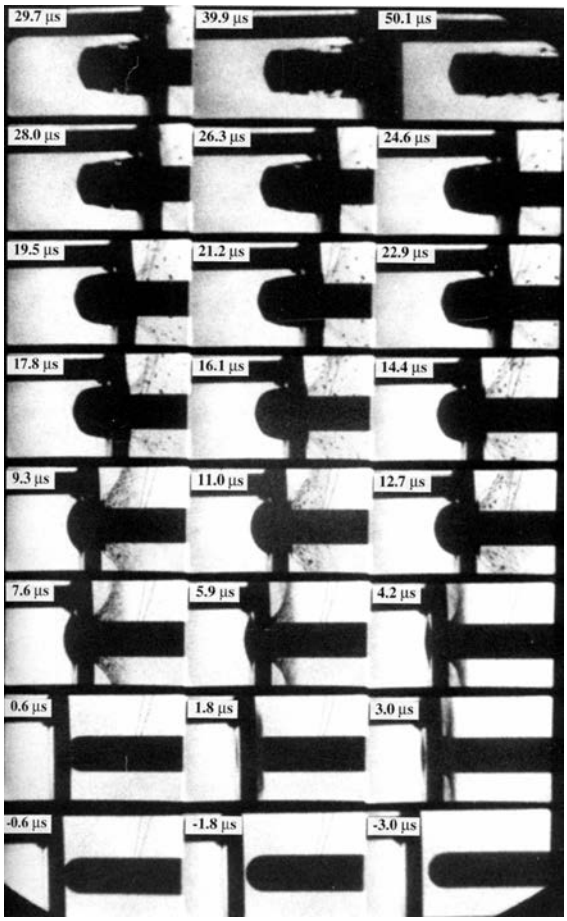

FIG. 3. High speed photographic sequence of reverse ballistic normal impact of a round nosed copper rod by a 4.8 mm thick annealed aluminium plate at 855 m s^{-1}.

the measurement accuracy of times when events take place. The rod diameter is, however, a reliable alternative distance scale marker. Second, for angled impact, any rotation of the plate during launch also obscures events on the surface. However, sabot rotation was never found to amount to more than 8°, and was usually much less. Third, because a dove prism was used to rotate the image by 90° so as to make best use of the frames output by the camera, shear distortion was introduced into the photographs. This distortion can make a plate oriented at 90° to the rod appear to be slightly angled (see, for example, Fig. 5).

3. Impact phenomenology

3.1. Characteristic times

The thickness of the plate determines, among other things, the fraction of the perforation time before the rod is significantly affected by the rear free surface. The effects of the relative dimensions of the plate thickness and nose radius may be characterised by comparing the time when the nose of the rod reaches a certain location with the time it would take to reach the same place if the plate were not present (see Fig. 4). It is best to think of this procedure as a guide to interpretation since errors are introduced into this scheme due to acceleration of the rod caused by the impact.

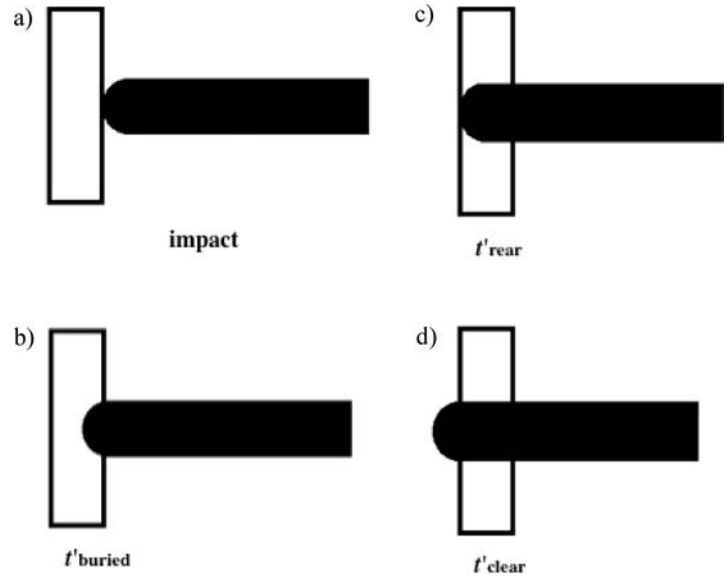

Fig. 4. Diagram illustrating the times after impact, calculated from the impact velocity and plate thickness, when the rod nose would (a) be just buried t'_{buried} (b) have just reached the rear surface t'_{rear} (c) have just cleared the rear surface of the plate $t_{\text{clear}'}$.

3.2. Round-nosed rods

The sequence of events typically seen in the normal impact of round-nosed rods are as follows: for the first microsecond or so, the load is applied over a small area which expands supersonically as more of the nose comes into contact with the plate surface [31–33]. This produces rapid radial flow of target material which jets laterally in a liquid-like manner (see Fig. 5). The geometry of the impact means that the angle of jetting changes continuously as the rod penetrates the plate. Thus the jets of material appear curved (Fig. 5d). Inspection of recovered rods showed that rod material did not form part of the ejecta for this material combination at this impact speed.

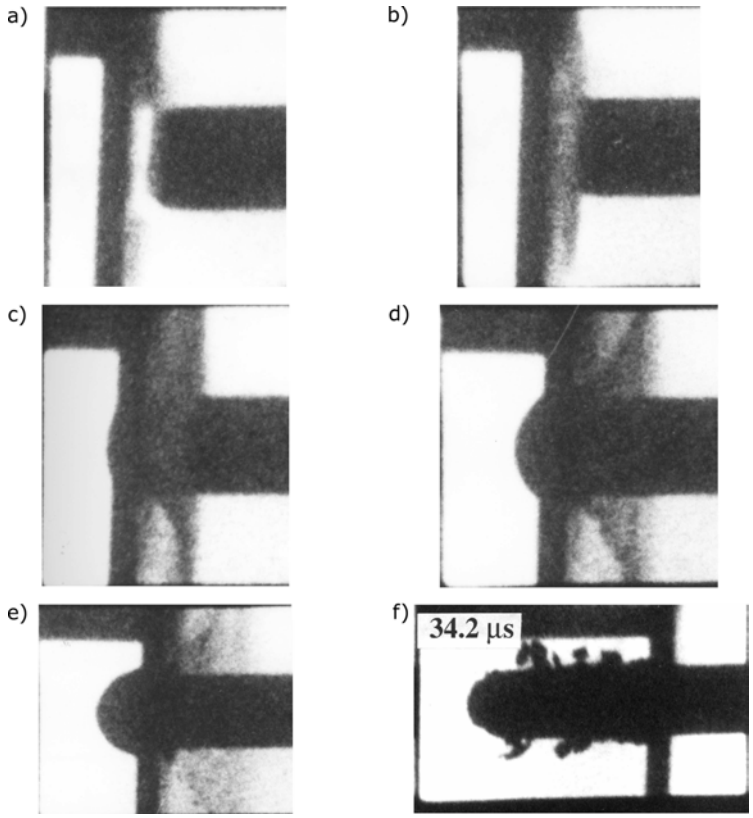

FIG. 5. Selected frames from the high-speed photographic sequence of the normal impact of a 9.5 mm diameter round-nosed mild steel rod by a 3 mm thick dural plate at 835 m s^{-1}: a) light flash seen 0.5 μs after impact; b) 1.7 μs after impact; c) 4.1 μs after impact; d) 6.5 μs after impact; e) 10.1 μs after impact; f) 34.2 μs after impact.

The rear surface of the plate will start to decelerate when the elastic stress wave generated by the impact first reflects off it. However, visible bulging does

not start until the plastic zone ahead of the rod reaches that surface (just before 1.8 μs in Fig. 3, for example). If the plate is sufficiently thin (as it is in the impact shown in Fig. 3) this will occur before the nose of the rod has fully penetrated the front surface. Plate material was pushed out by the rod eventually detaching as a plug attached to the front of the rod. A narrow shear zone is required for plugging, so plugging does not occur in metals which work-harden as this process suppresses the formation of adiabatic shear bands (ASBs) [34, 35]. Hence work-hardening materials flow uniformly to large strains. In these cases, a bulge forms whose diameter larger than the rod and which eventually tears away. This had certainly happened by 40 μs in Fig. 3.

Occasionally a brief flash of light was recorded at impact (Fig. 5a). The probable reason this was only rarely seen is that the duration of such flashes is substantially shorter than the interframe time of the camera, set to 0.3 μs in this case. Possible origins for these light flashes include: (i) the thermite reaction, if metals like copper and aluminium are used, or (ii) adiabatic compression of trapped gas between the surfaces [36]. As steel and aluminium were used in the experiment shown in Fig. 5, the latter explanation is more likely. In the sequence shown in Fig. 5, jets of material were visible by 1.7 μs, reaching their final angle to the surface by 6.5 μs and beginning to die off by around 9 μs. The bulge began to be visible around 3 μs. The diameter of the bulge was nearly the same as the rod diameter, a characteristic of thin plates. The plate bulged out to a distance of three plate thicknesses before any notches appeared (the first sign of plug failure) at around 14 μs, Subsequently, there were multiple failure points leading to the break-up of the plug into small pieces (Fig. 5f).

In a similar experiment performed on a 6 mm thick plate, the bulge appeared at around 7.0 μs. This is a significantly smaller fraction of t'_{rear} than for the thinner plate (7.0 μs is about 65% of 10.8 μs whereas 2.9 μs is 81% of 3.6 μs). The thicker plate also bulged less (one plate thickness) before notches appeared.

3.3. Flat-ended rods

Figure 6 presents a typical high-speed sequence for normal impact on a flat-ended rod. The major difference with the hemispherical-nose rod case is that the full width of the rod enters the target on impact. This means there is little lateral displacement of plate material and no jetting. There is, however, intense shear around the circumference of the rod, increasing the likelihood of plug formation. During the breakout phase little lateral flow of the plug material would be expected (which causes plug thinning). The initial failure of the rear face favours pieces of target material around the rod circumference breaking away. This can be seen happening late on the sequence.

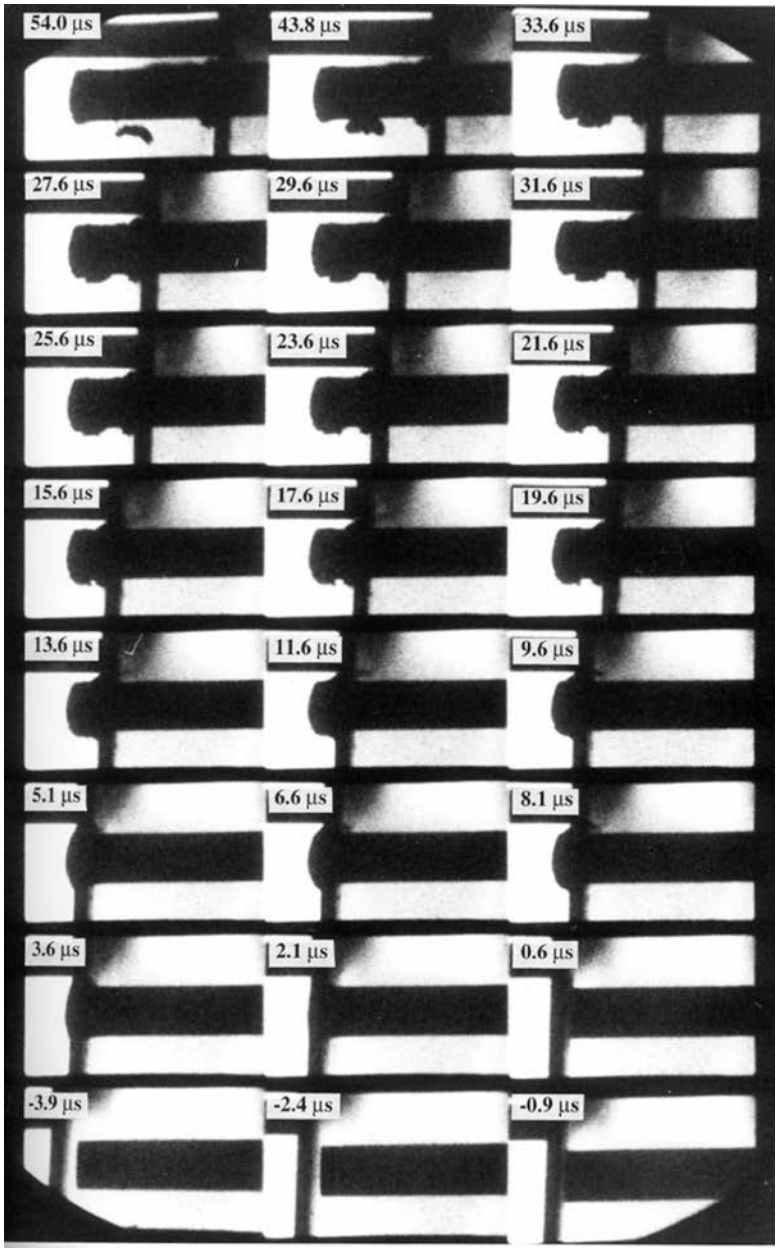

FIG. 6. High speed photographic sequence of the normal impact of a flat-ended mild steel rod by a 3.0 mm thick dural plate at 533 m s^{-1}.

Tables 3 and 4 present data obtained from high-speed photographic sequences of the normal impact of hemispherical and flat-ended steel rods struck by dural plates.

Table 3. Data obtained from high-speed photographic sequences for hemispherical-nosed steel rods struck normally by 3 mm thick dural plates.

Impact velocity [m s^{-1}]	Time the plate first deviates from constant velocity [μs]	Time for rear of plate to become stationary [μs]	Time jets appear [μs]	Time rear bulge appears [μs]	Time rear notch appears [μs]	Extent of bulge at failure [%]*	Final plug thickness [mm]	t'_{rear} [μs]
556	2.4	21.6	3.6	3.6	16.8	300–400	0.8	5.4
561	2.0	9.2	3.2	3.2	15.2	≥ 300	1.3	5.3
549	2.4	4.8	2.4	2.4	13.2	300	1.7	5.5
543	2.3	10.2	1.7	2.9	12.5	≥ 300	1.6	5.5

* Note that '200%' means one extra plate thickness, '300%' two extra plate thicknesses and '400%' three extra plate thicknesses.

Table 4. Data obtained from high-speed photographic sequences for flat-ended mild steel rods struck normally by dural plates of various thicknesses.

Dural plate thickness [mm]	Impact speed [m s^{-1}]	Time of first deviation from constant velocity [μs]	Time for rear of plate to become stationary [μs]	Time rear bulge appears [μs]	Time notch first appears in rear of plate [μs]	Extent of bulge at failure [%]	Final plug thickness [mm]	t'_{rear} [μs]
3	533	1.25	2.75	2.1	8.1	200	2.4	5.6
6	556	2.0	15.2	3.2	15.2	200	2.75	10.8
10	550	8.8	29.7	6.9	24.0	< 200	2.5	18.2

3.4. Oblique rod impacts

Oblique impact requires an extra characteristic time to describe it, i.e., where the centre of nose of the rod reaches the plate rear (see Fig. 7). The plate angle, plate thickness and nose radius determine the order the events identified in this figure occur in.

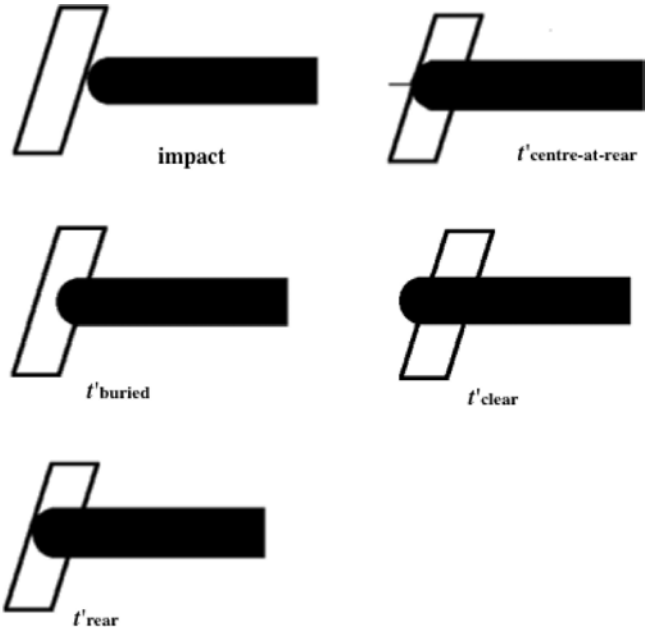

FIG. 7. Schematic diagram showing how the characteristic times are defined for oblique impact.

An angled plate has more resistance to penetration than the same plate oriented at 90° to the rod axis simply because of the greater thickness of material in the direction of motion. This concept may be quantified by the 'effective path length' (*EPL*) which is the distance that must be traversed by a rod through a plate before its nose is completely clear of the original rear surface. In normal impact of a hemispherical-nosed rod, the *EPL* will be the sum of the plate thickness and the rod radius. In angled impact, the width of the rod becomes important because the trailing edge of the nose reaches the original rear surface later than the leading edge.

The mechanics of oblique impact are also more complex than normal impact (see Fig. 8) as bending waves as well as longitudinal waves are generated [37]. Consider first a hemispherical-nosed rod (see Fig. 8). The initial phase can be seen to be the ejection of plate material, mostly in the direction of impact. In Fig. 9, 'backward' ejection of material can be seen to cease after about 6–7 μs.

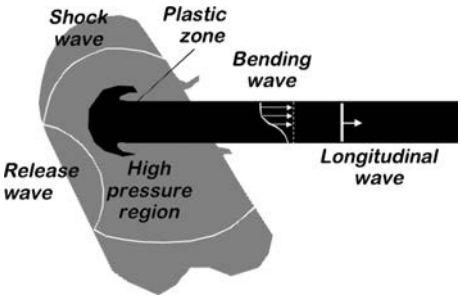

FIG. 8. Schematic diagram of wave phenomena due to ballistic impact of a rod on an angled target. Adapted from reference [18] p. 299.

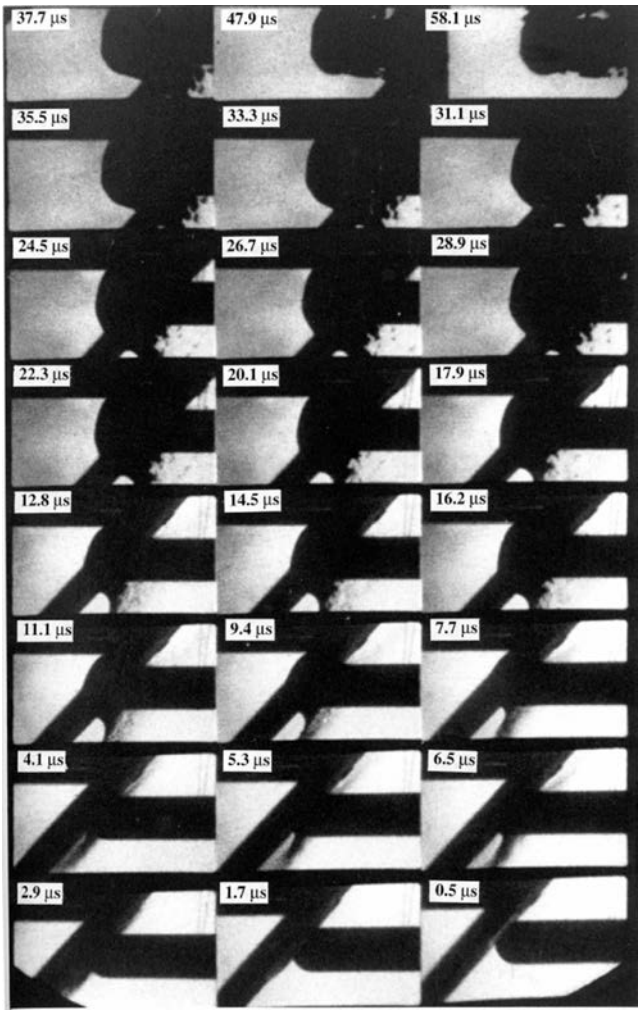

FIG. 9. High-speed photographic sequence of the impact of a 4.8 mm thick aluminium plate at 45° on a round-nosed copper rod at 830 m s^{-1}.

In this experiment, very little sliding of the rod on the plate took place and the rod started perforating the plate close to the impact point around 30 μs after impact.

The craters due to oblique impact are usually symmetric in the plane. For small amounts of slip, they are oval in shape. For large amounts of slip, they have the form of long shallow grooves terminating where perforation occurs. Elongated craters are often associated with bending of the rod, raising the frictional forces between the rod and the plate. An example of this can be seen in Fig. 10 where the bulge can be seen moving at a constant velocity along the rear

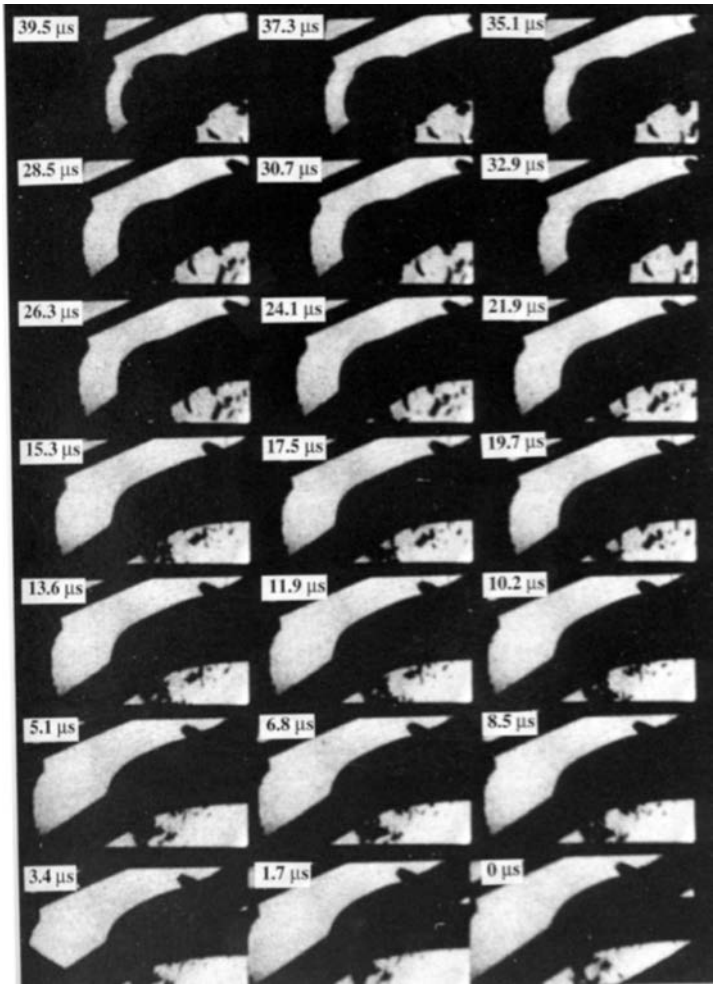

FIG. 10. Selected frames from the high-speed photographic sequence of the impact of a 5 mm thick RHA steel plate at 60° on a round-nosed tungsten alloy rod at 645 m s^{-1}. Note that in this sequence the time at which impact occurred is not known, so the first frame (bottom right) is set as time zero.

surface of the plate for some time before perforation finally occurred at around 35 μs. This experiment was performed quite close to the ricochet angle.

For oblique impact it is not possible to predict where on the rear surface the bulge will first appear. Often it is laterally displaced beyond the projection of the rod cross-section. The resulting bulge subsequently lengthens along that surface back towards the rod axis and then past it and a plug of material will be pushed out as for normal impact.

Figure 11 presents a comparison at similar times between the oblique impact of round-nosed and flat-ended steel rods by 6 mm thick dural plates. The main difference is that the flat-ended rod produces a hinge of material in the target that breaks off as a few (possibly even one) large pieces (Fig. 11d) whereas the round-ended rod generates many small fragments in the dural plate (Fig. 11b).

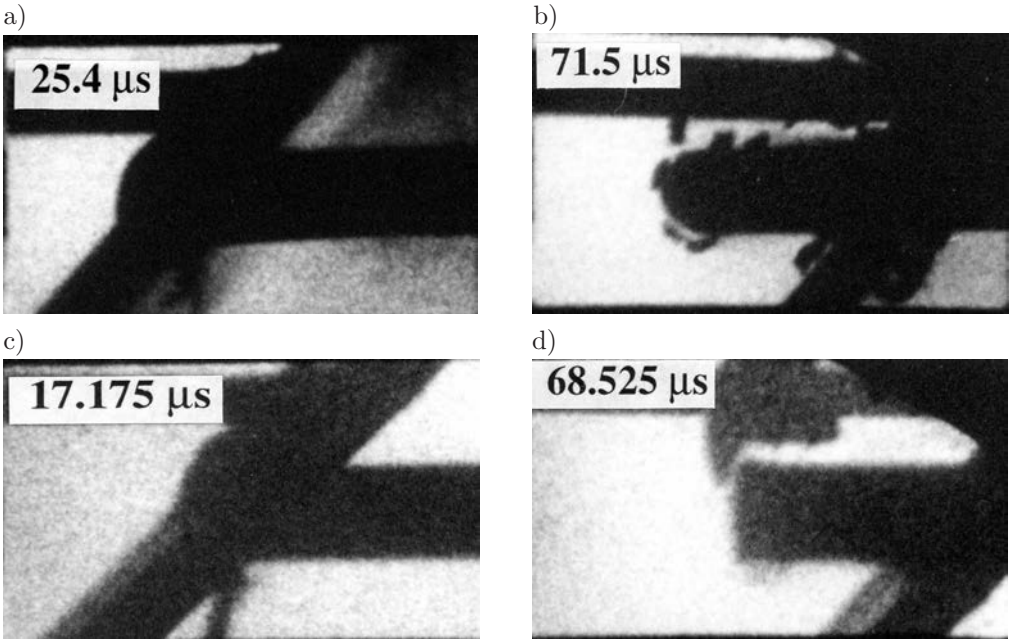

FIG. 11. Comparison of 45° oblique impact of two types of mild steel rods by dural plates: a) and b) impact conditions: 9.5 mm diameter, 215 mm long hemispherical-ended rod, 6 mm thick plate at 550 m s^{-1}; c) and d) impact conditions: 9.5 mm diameter, 215 mm long flat-ended rod, 5.9 mm thick dural at 549 m s^{-1}.

Figures 12 and 13 show up some of the similarities and differences between the normal and oblique impact of dural plates on round-nosed mild steel rods with that of RHA steel plates on a tungsten rod at similar impact speeds. Recall that the reason for choosing the materials of the plate/penetrator pairs studied was that the ratios of density and yield strength were similar to RHA/tungsten (see Table 2). It can be seen from Fig. 13 that the RHA plate produces larger

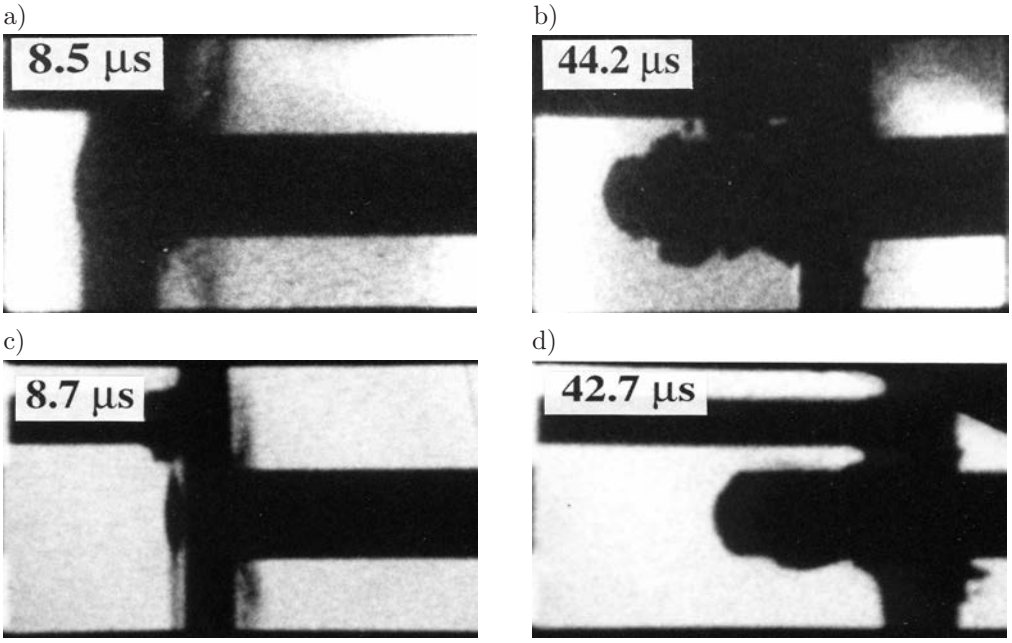

FIG. 12. Comparison of images taken at similar times after normal impact from high speed photographic sequences of the impact of 9.5 mm diameter mild steel rod by a 6 mm thick dural plate at 555 m s^{-1} (frames a) and b)) and a 10 mm diameter tungsten alloy rod by a 5 mm thick RHA steel plate at 533 m s^{-1} (frames c) and d)).

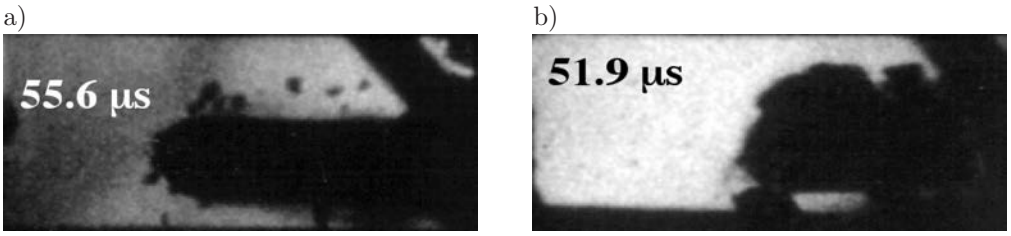

FIG. 13. Comparison of the impact of (a) a 5.9 mm thick dural plate against a 9.5 mm diameter, 215 mm long round-nosed mild steel rod at 823 m s^{-1}, 45° impact angle; b) a 5 mm thick RHA steel plate against a 10 mm diameter, 100 mm long round-nosed tungsten alloy rod at 810 m s^{-1}, 45° impact angle.

fragments than the dural. It was also observed that the tungsten rods deformed more than the mild steel rods and sometimes shattered, particularly in oblique impact. Both RHA and tungsten are more brittle than either dural or mild steel. So although dural/mild steel experiments can provide information useful to the RHA/tungsten problem, there are important differences particularly with respect to rod deformation and fracture of both target and penetrator. The main advantage of using mild steel and dural in preliminary experiments is that these materials are much cheaper and more readily available. Such experiments can

provide an indication of expected events along with timings and outcomes of various geometries. They can also provide useful results before committing to more expensive, full-scale experiments [22].

Considering the other pair of metals studied (aluminium/copper), we see from Fig. 14 that the main visual difference is that the aluminium deforms without fracture to much larger strains than mild steel (compare Figs. 14b and 14d). Copper and aluminium also strain-harden much more than the other pairs of materials considered. The impact stresses (normalised by the plate yield stress) for the impact velocities studied were largest for the aluminium/copper pair, ranging from 32–53. Those for dural/mild steel ranged from 20–30 and that for RHA steel/tungsten ranged from 8–14. Thus we conclude that the aluminium/copper combination is less useful for performing cheaper preliminary studies of RHA steel/tungsten impacts than dural/mild steel.

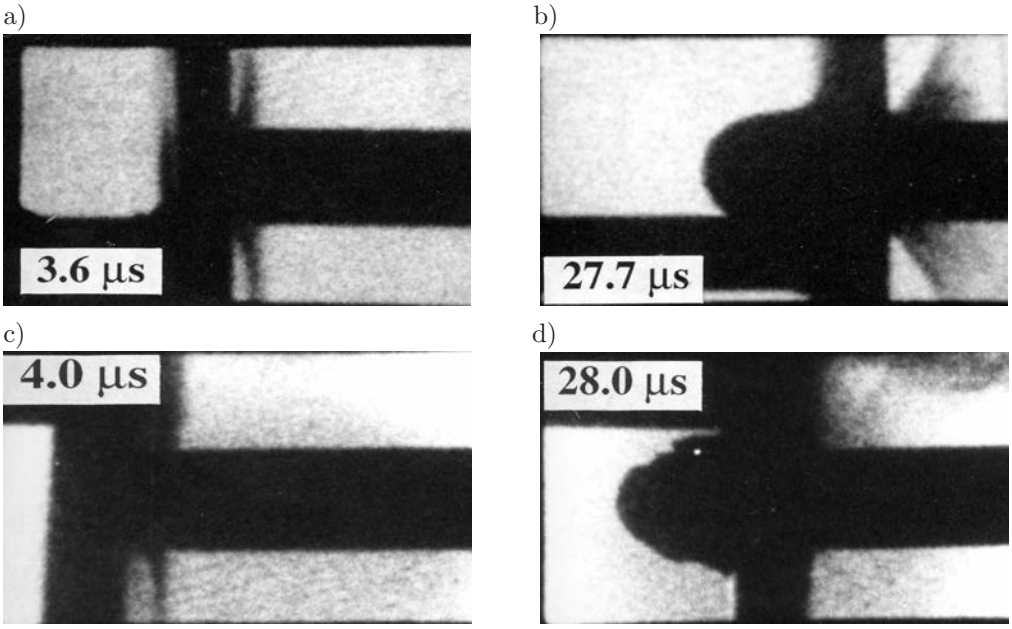

FIG. 14. Comparison of selected frames from a high-speed photographic sequence taken of the normal impact between a 4.8 mm thick pure aluminium plate and a 10 mm diameter, 99 mm long annealed round-nose copper rod at 549 m s^{-1} (frames a) and b)) with those at similar times (frames c) and d)) from the impact of a 6 mm thick dural plate on a 9.5 mm diameter, 215 mm long round-nosed mild steel rod at 554 m s^{-1}.

4. Impact instrumentation

In order to decide what instrumentation to use, it is necessary first to consider what stress-wave activity we might expect. On first impact, shock waves are

launched into both the rod and the plate [38]. For a flat-ended rod struck by a plate at normal incidence, those two waves are both initially planar. For other geometries the shock structures are more complex. Behind the shock wave in the rod, material flows plastically. Rarefaction waves also travel inwards from the free surfaces modifying the shock structure and sometimes producing internal fractures [39]. Elastic compression and shear waves meanwhile run ahead of the plastic deformation front and reflect from any free surfaces they encounter.

As the stationary rod penetrates the moving plate, both the rod and plate deform plastically. The stress at the boundary of the rod and the plate has the effect of accelerating material within the rod up towards the velocity of the impacting plate (Fig. 15). As this happens, the stress at the rod-target interface decreases. When this drops below the flow stress, the rod starts to behave rigidly. As the rod nears the rear surface of the plate, a bulge appears. A plug may also form if the plate material is susceptible to ASB formation. When removed from the constraint of the surrounding material, the plug may detach as a solid disc or fracture into pieces, depending upon the plate thickness, ductility and strain-to-failure etc. Blunting of the projectile nose is common. In addition, plastic distortion may reach some considerable distance back into the rod.

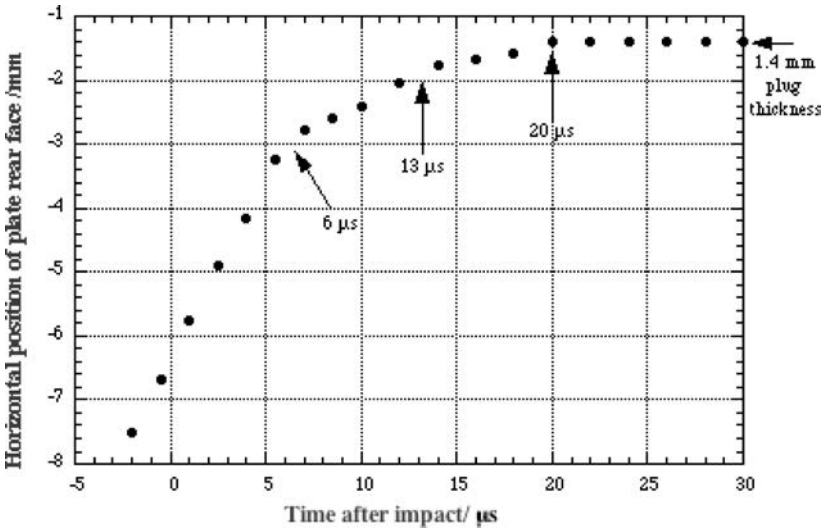

FIG. 15. Plot of the rear surface of a 3 mm thick dural plate impacted normally by a 9.5 mm diameter mild steel rod at 554 m s^{-1}. Data were measured from the high-speed photographic sequence taken. Visible plate bulging began around 6 μs.

Stress wave effects due to plate penetration and perforation make the rod response more complex than in Taylor impact (Fig. 16). However, as in Taylor impact, an elastic wave propagates to the end of the rod and returns to interact repeatedly with the plastic front (Fig. 17), lowering the stress in the process.

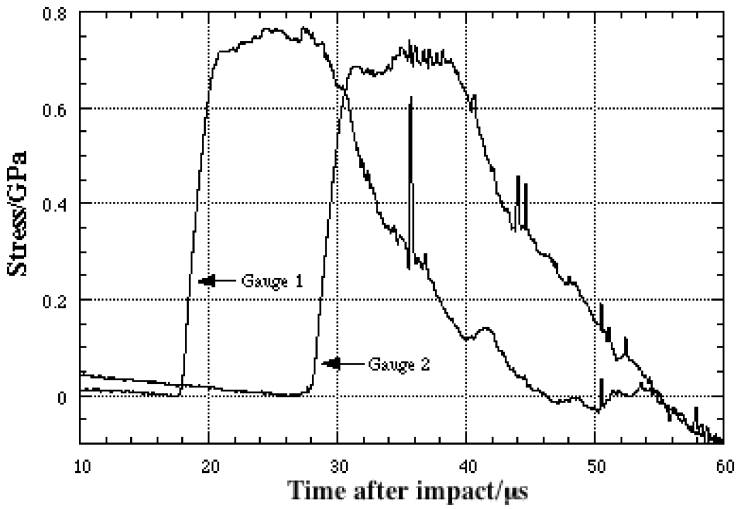

FIG. 16. Stress pulses from manganin pressure gauges embedded in a round-nosed mild steel rod impacted by a 6 mm thick dural plate at 554 m s^{-1}.

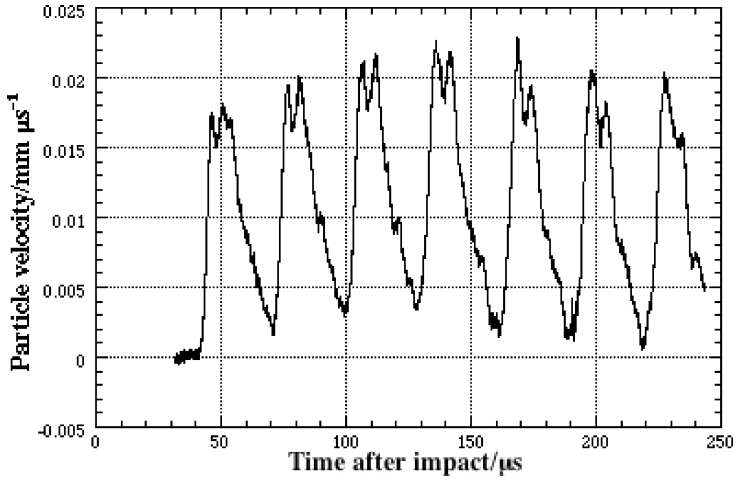

FIG. 17. VISAR trace for the rear of a round-nosed mild steel rod impacted by a 6mm thick dural plate at 554 m s^{-1}.

Because of the complexity associated with interpreting waves in rods generated by the impact and perforation of thin metal plates, some instrumented experiments were performed using thin alumina plates (Fig. 18). These plates maintain a high stress on the end of the rod for a relatively long period of time producing a more flat-topped stress pulse allowing the effects of elastic wave dispersion to be assessed without the complexities introduced by early perforation. Such experiments also allow the high rate, low strain mechanical properties of the mild steel rods to be determined [40, 41].

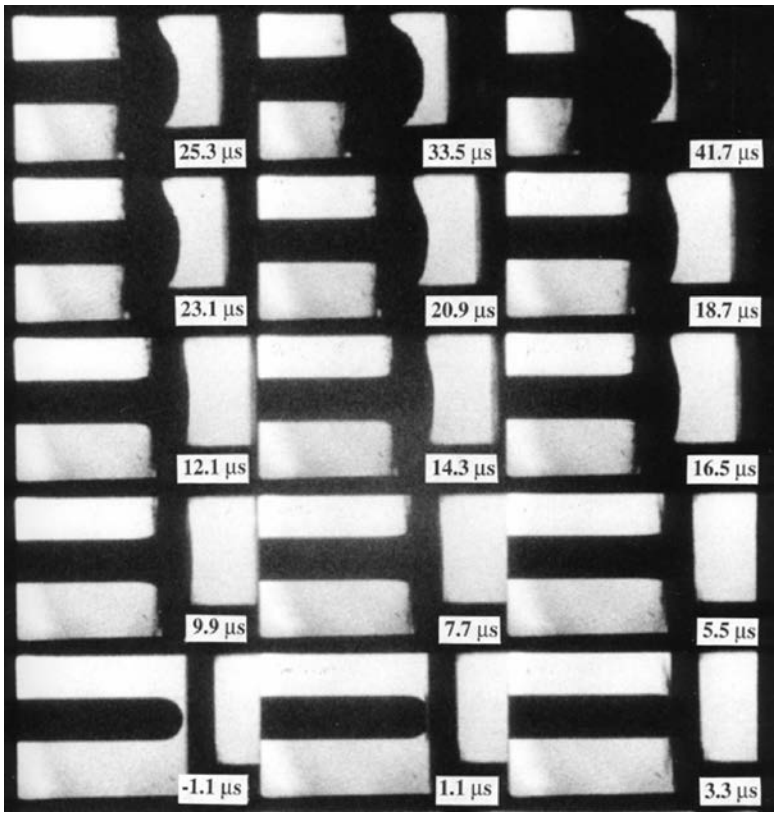

FIG. 18. High speed photographic sequence of the normal impact of a 9.5 mm diameter round nosed mild steel rod by a 6.5 mm thick alumina plate moving from right to left at 525 m s^{-1}.

Elastic wave dispersion in rods is well-known not only to reduce the slope of the rise up to maximum stress but also to introduce oscillations into the measured signal. The major source of distortion is that the velocity of stress waves in rods depends upon frequency. These effects were shown by both POCHHAMMER [42] and CHREE [43] to be intrinsic to infinitely long, but finite diameter, rods. They are, therefore, not artefacts specific to rods of finite length. However, dispersion is considerably more complicated for finite-length rods and generally agreed to be mathematically intractable [44].

Three experiments were performed, two with hemispherical-nosed ends and one with flat. Figure 19 presents the two stress gauge traces produced by the impact on a round-nosed steel rod of a 3 mm thick alumina plate moving at 541 ± 5 m s^{-1} and mounted directly on the front of the sabot. The underlying slew rate of the gauge power supply can be seen as a negative slope before the arrival of the pulses. The time of impact was determined to an accuracy of ± 0.7 μs from the high-speed photographic sequence taken.

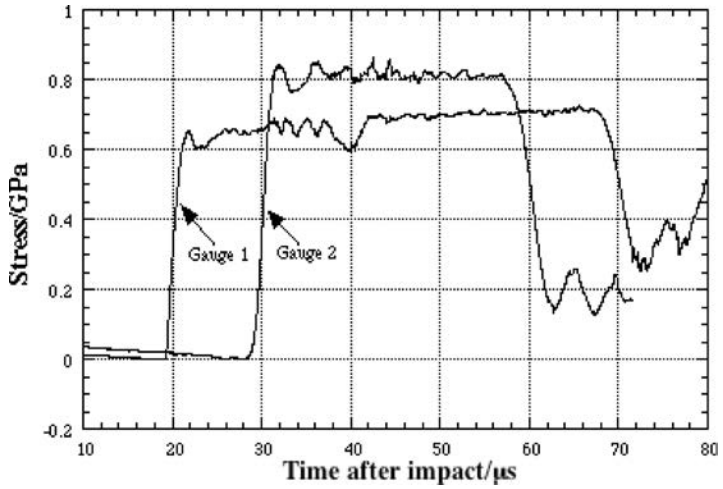

FIG. 19. Stress pulses recorded by two manganin stress gauges located at 90 mm (gauge 1) and 140 mm (gauge 2) from the impact point of a 9.5 mm diameter, 215 mm long round-nosed mild steel rod struck by a 3 mm thick alumina plate mounted on the front surface of a polycarbonate sabot and travelling at 541 m s^{-1}.

The stress can be seen to rise up to an initial overshoot followed by a 'plateau' region with some oscillations. These oscillations are due to dispersion and therefore do not occur at the impact face. They are, however, real at the gauge location and not an artefact of the gauges. The stress pulses end when the tensile release wave from the rear of the rod reaches the gauge locations. The time from the start of the rise until the start of the decay gives a measure of the velocity of the fastest elastic wave in the rod. The wave velocity calculated in this way was 5200 m s^{-1} for the signal from gauge 1 and 5170 m s^{-1} for the signal from gauge 2 which agree very well with the value of 5200 m s^{-1} measured using an acoustic wave generator. The velocity calculated from the transit time between the two gauges was 5520 m s^{-1}, 5% different to the other values.

Note that in this particular experiment there was a discrepancy in the maximum stress reached that was greater than the variation in the gauge factor (typically 2%). Gauge 1 recorded a stress of 0.65 GPa at the end of the rising phase creeping up to 0.70 GPa by the end of the pulse, whereas gauge 2 recorded a stress rising directly to 0.80 GPa. It is not known why this was so and this difference was not seen in other experiments (see, for example, Fig. 20).

The rise time for the pulse recorded by gauge 1 was 2.1 μs and that for gauge 2 was 3.1 μs. These times are in reasonable agreement with the 4 μs rise time measured by ROSENBERG and BLESS [41] at a distance of 127 mm along mild steel rods impacted at about half this velocity. Dispersion sets a lower limit to the rise time and depends upon the distance the pulse has travelled along the rod (see Fig. 21).

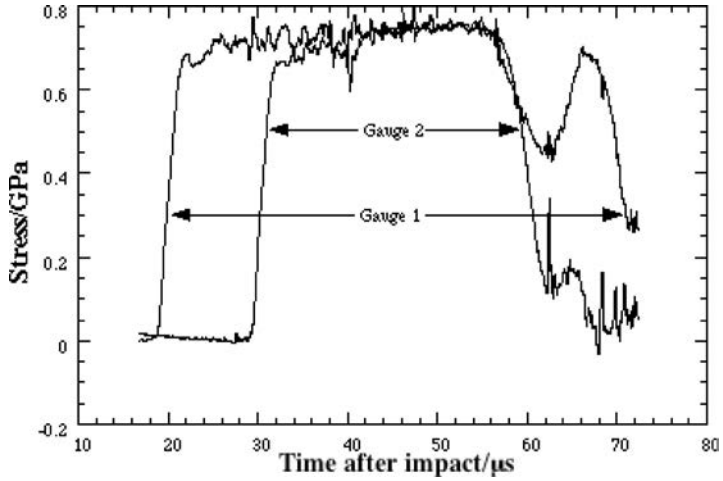

FIG. 20. Stress pulses recorded by two manganin stress gauges located at 90 mm and 140 mm from the impact point of a 9.5 mm diameter, 215 mm long round-nosed mild steel rod by a 6.5 mm thick alumina plate mounted on pillars on a polycarbonate sabot travelling at 525 m s^{-1}.

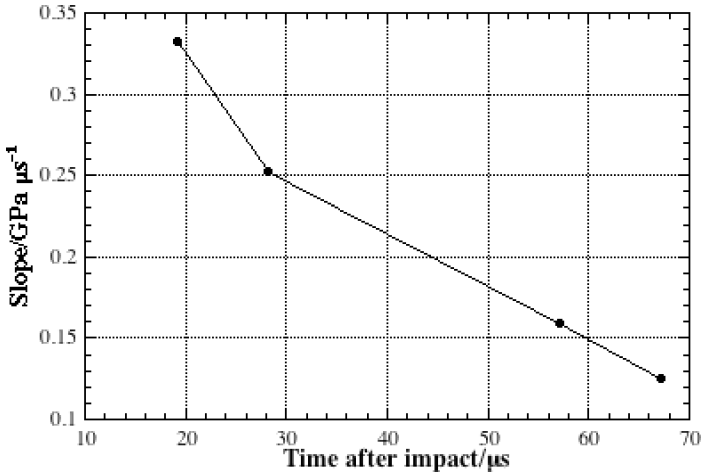

FIG. 21. Graph of the gradients of the rise and decay portions of the stress pulses shown in Fig. 19 versus time from impact.

A VISAR measurement (see Fig. 22) was also performed on the rear end of the rod. This trace confirms many features of the stress pulses shown in Fig. 19. The velocity can be seen to rise to 0.033 mm μs^{-1}, equivalent to 0.66 GPa using the following relation:

$$\sigma = 0.5\rho c v, \tag{4.1}$$

where ρ is the density, c is the elastic wave speed of mild steel (see Table 1) and v is the particle velocity.

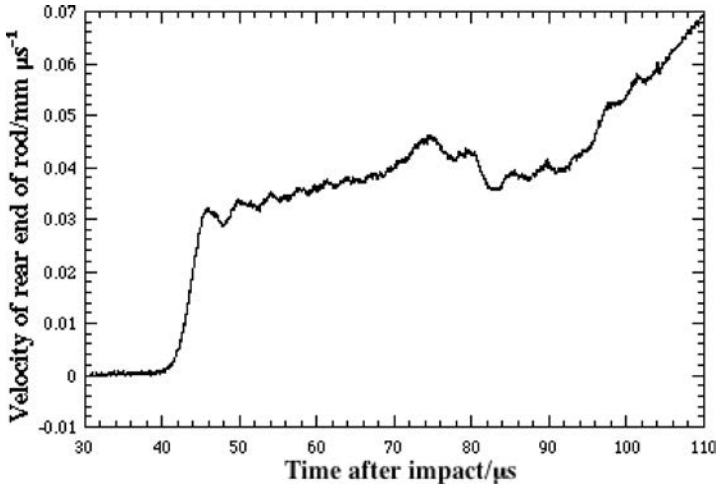

FIG. 22. VISAR trace recorded at the rear end of the round-nosed mild steel rod impacted by a 6.5 mm thick alumina plate at 525 m s^{-1} (same impact as Figs. 18 and 20).

The initial rising slope is 0.009 mm μs^{-2}, equivalent to 0.18 GPa μs^{-1}. This value lies between those for the two rises (0.28 and 0.30 GPa μs^{-1}) and the two decays (both 0.16 GPa μs^{-1}) recorded by the stress gauges, consistent with the fact that the pulse reached the end of the rod midway between the rise and decay of the stress recorded at gauge 2. Since the loading at the impact face continues for an extended period, the velocity of the rear of the rod does not decrease during the course of the trace presented in Fig. 22, rather the velocity creeps up steadily from the top of the initial rise. Then, there is a slight peak followed by a dip of short-duration at around 80 μs after which the velocity rises again. This peak occurs close to the time it would take for the elastic wave to return from the rear of the rod to the location of gauge 2. So the dip may represent a partial release of the gauge package. The velocity eventually rises significantly beyond that expected on the basis of the stress gauge readings. This may be due to the rear of the rod approaching the position of the duplex optical fibre which brings laser light to and from the VISAR. As this happens, the VISAR system compensates for the change in intensity of the beam reflected from the rod, losing accuracy in the process.

The high-speed photographic sequence for this experiment (Fig. 18) confirms the relatively long time that the alumina plate resisted penetration. During this time the front of the rod can be seen to deform plastically and increase in diameter (see, for example, the frame labelled 5.5 μs). Note also the jetting of material visible about 3 μs into the impact. The angle of jetting is similar to that for a ductile plate at about the same time (see Fig. 23), though as penetration proceeds, the angle of jetting increases for a ductile material (Fig. 23d).

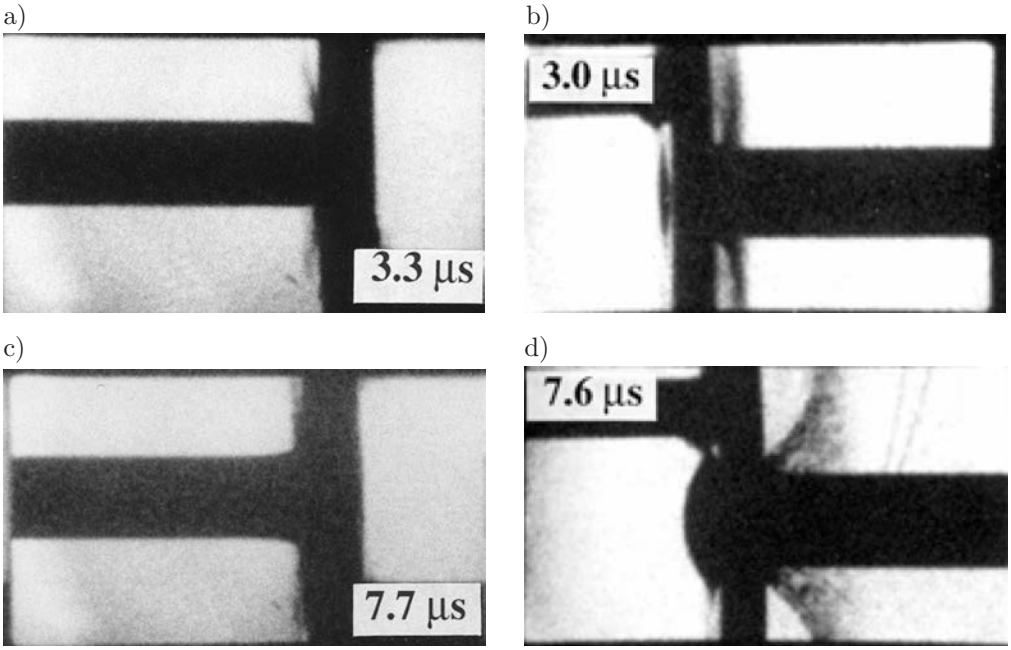

FIG. 23. Comparison of impacts at similar times on a rod by (a) and (c) – an alumina plate and (b) and (d) - a metal plate. Experimental conditions: a) and c) 9.5 mm diameter round-nosed mild steel rod, 6.5 mm thick alumina plate moving from right to left at 525 m s^{-1}; b) and d) 10 mm diameter round-nosed copper rod, 4.8 mm thick aluminium alloy plate, moving from left to right at 855 m s^{-1}.

Apart from the direct photographic evidence the rod deforming laterally between about 5 and 10 μs into the impact (Fig. 23c), there is also indirect evidence of rod deformation in that the position of the plate rear surface at the end of the high-speed sequence (41.7 μs; not shown) is actually to the left of the initial point of the rod nose by more than 1 mm, implying a negative thickness for the ceramic material pushed ahead of the rod. However, if the double transit time of the elastic wave in the rod (41.5 μs) is taken into account, the rod would only just have begun to move bodily by this point. Thus, the rod must have shortened. Another piece of evidence for this is that the time measured from the photographs for the bulge to protrude a distance equal to a single plate thickness is 25.3 μs. The implication of this is that the rear of the plate took the same time to move out to one plate thickness as the rod would have done had it been unimpeded, yet there appears still to be plate material ahead of the rod. But since the rod had not yet begun to accelerate bodily, the rod must have shortened.

The third experiment in this series involved firing a 6.5 mm thick alumina plate (mounted on rods) at 523 m s^{-1} against a flat-ended mild steel rod. Figure 24 presents the two resulting stress gauge traces along with the VISAR data

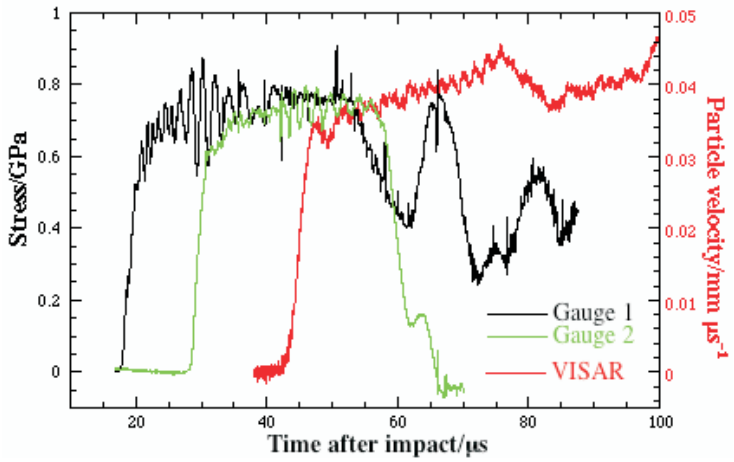

FIG. 24. Stress pulses recorded by two manganin stress gauges located at 90 mm and 140 mm from the impact point of a 9.5 mm diameter, 215 mm long flat-ended mild steel rod along with the particle velocity of the far end of the rod measured using VISAR. The rod was impacted by a 6.5 mm thick alumina plate mounted on pillars on a polycarbonate sabot travelling at 523 m s^{-1}.

plotted on the same time axis. It is noticeable that the pulse from gauge 1 also shows the same break in the plateau stress at approximately the same time as for the second shot against a round-nosed rod (see Fig. 20). The stress oscillations are of much greater amplitude in these traces compared to those in the round-nosed rod, particularly for gauge 1. Only the highest frequencies, with reduced amplitude, are still seen by gauge 2. The periods of these oscillations have values that are both longer and shorter than the time taken for an elastic wave to traverse the rod diameter once (1.8 μs).

The technique of impacting a long rod with a strong target provides a method of measuring the elastic wave amplitude under conditions of one-dimensional stress at strain rates of 10^2–10^3 s^{-1} and small strains. The data generated is therefore more directly comparable to plate impact (strain rates in excess of 10^5 s^{-1}) than that obtained from the split Hopkinson pressure bar (SHPB) which is normally used for the 10^3–10^4 s^{-1} strain rate regime. The other major difference between the SHPB and plate impact is that the SHPB can only be used to measure flow stresses in one-dimensional stress for plastic strains greater than about 5% [45] whilst plate impact gives the yield stress under one-dimensional strain (the Hugoniot elastic limit or HEL). This can make it difficult to compare results from the two techniques in rate dependent or work-hardening materials. We found the rod technique worked best using thin alumina plates and round-nosed rods since a flat-ended rod (equivalent to reverse Taylor impact) produces a stress pulse with higher amplitude oscillations (compare Fig. 20 and 25). In the light of the above considerations, all the rods were instrumented

by embedding manganin foil stress gauges within them 90 mm from the nose (gauge 1). For the longer steel rods, additional gauges were placed 140 mm from the nose (gauge 2).

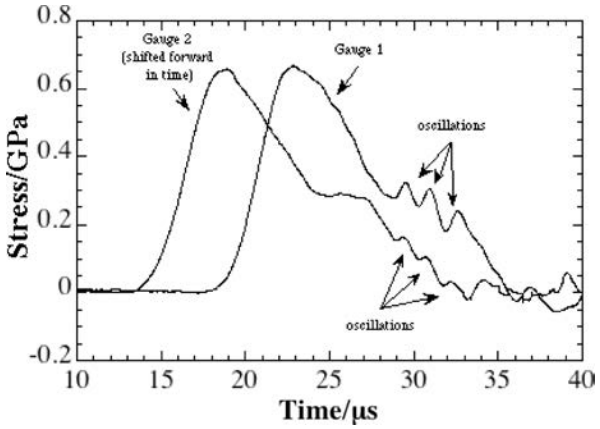

FIG. 25. Plot of the outputs of the manganin gauges located 90 and 140 mm from the impact point of a round-nosed mild steel rod struck by a 3mm thick dural plate at 556 m s^{-1}. The traces have been time-shifted so that the oscillations on the descending part of the pulses coincide in time.

For accurate measurement of the stress, the epoxy layer used to embed the gauge must be thin enough that the stress in the gauge package 'rings up' in a small fraction of the timescale of the experiment. Also the gauge must be positioned sufficiently far from the impact end so that three-dimensional end effects have died away. Ten rod diameters have been found to be sufficient [27, 44]. This was confirmed by modelling results (presented later in this paper in Figs. 29 and 30) which showed that in most cases the stress profile equilibrates by a distance equal to nine diameters of travel. Time-shifting the traces obtained from gauges placed at different positions in the rods shows that the oscillations travel at a lower speed than the bulk of the stress wave, and, hence, appear at a later stage of the pulse recorded from gauge 2 (Fig. 25).

Checks were also made both on the reproducibility and accuracy of the gauges. Reproducibility was checked by repeating experiments (Fig. 26). Accuracy was checked by comparing the gauge trace with the output of a VISAR (Fig. 27). As agreement was found to be satisfactory, most experiments were performed with gauges only as this is easier to do.

A check was also made of the amount of lateral strain at the first gauge location (nine bar diameters from the impact point) by replacing the stress gauge at that point in one experiment by a constantan foil strain gauge. The maximum strain recorded was only 0.17%, which is sufficiently small to imply that lateral strain has a negligible effect on the output of the stress gauges.

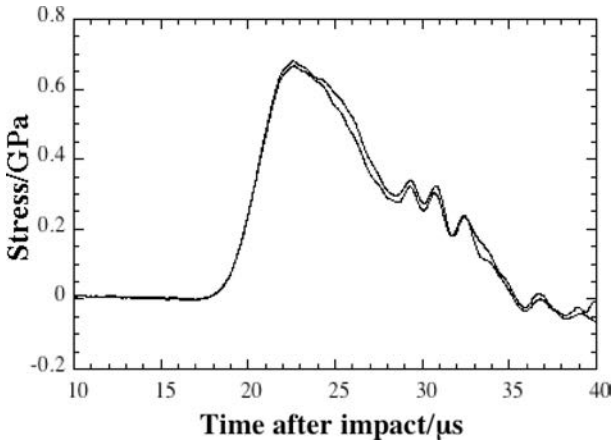

FIG. 26. Demonstration of the reproducibility of outputs of manganin gauges located 90 mm from the impact points of two round-nosed mild steel rods impacted by 3 mm thick dural plates at 556 and 561 m s^{-1}.

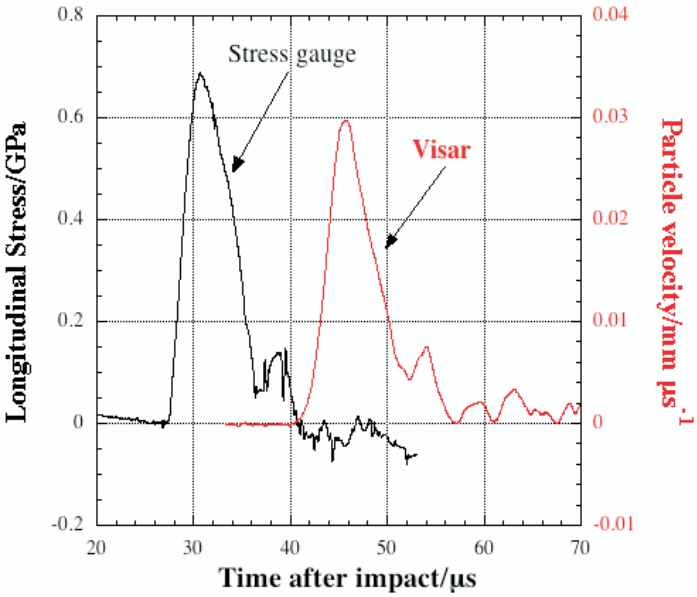

FIG. 27. Comparison of the output of the manganin stress gauge at location 2 with VISAR from the end of the rod for the impact of a 9.5 mm diameter round-nosed mild steel rod by a 3 mm thick dural plate at 835 m s^{-1}.

5. Modelling of tungsten rods perforating RHA plates

A modelling study of some of the round-nosed tungsten rod impacts on 5 mm thick RHA steel plates was performed using the second generation Eulerian hydrocode GRIM, which was developed by researchers in QinetiQ in order to

investigate general problems in explosive technology and penetration mechanics [46–50]. This hydrocode is capable of multi-material interaction in both 2D and 3D.

Three experiments were chosen for modelling: two at normal impact, 533 m s^{-1} (shot 41) and 833 m s^{-1} (shot 42), and one at 45°, 810 m s^{-1} (shot 46). The two normal impacts were treated as two-dimensional axisymmetric problems, whereas the oblique shot required three-dimensional treatment. The Zerilli-Armstrong (ZA) constitutive models (modified for the temperature variation of shear modulus) were used for the two materials (Eq. (5.1) and Table 5):

$$\sigma = (C_0 + C_1\varepsilon^n)\mu_T/\mu_{293} + C_2 \exp\left(-C_3T + C_4T\log(\partial\varepsilon/\partial t)\right), \tag{5.1}$$

where C_0 to C_4 and n are constants and σ, ε, $\partial\varepsilon/\partial t$ and T are respectively stress, strain, strain rate and absolute temperature, μ_{293} the shear modulus at 293 K and μ_T the shear modulus at the current temperature. The constants were directly measured from interrupted tensile tests and are obtained by rearranging Eq. (5.1) and calculating slopes and intercepts. The modified Armstrong-Zerilli model was run in conjunction with a Mie-Grüneisen equation of state to describe the hydrostatic response.

Table 5. Parameters of the modified Armstrong-Zerilli constitutive model for the RHA steel and tungsten alloys used.

Parameter	FNC tungsten	RHA steel
Shear modulus [GPa]	13.4	9.545
C_0 [MPa]	600	780
C_1 [MPa]	750	715
C_2 [MPa]	2700	950
C_3 [K^{-1}]	0.0043	0.0052
C_4 [K^{-1}]	0.00017	0.00026
n	0.65	0.65

The rods that supported the plates (see Fig. 2) were not included in the simulations. Any influence of the plate mounts on the impact cannot occur until approximately 7 μs after impact since they are located 10 mm from the plate centre and an elastic double-wave transit of 20 mm in RHA steel takes 6.8 μs. This would be seen at the gauge position some 25 μs or more after impact, just after the peak stress. Their influence on the measured signal is likely to be minor.

A mesh resolution study involving three mesh sizes of 1 mm, 0.5 mm and 0.25 mm was performed for each experiment to ensure that convergence was achieved.

The simulation technique was first used to calculate the axial stress in the rod at a Lagrangian gauge position 90 mm from the rod end corresponding to the measurements taken at gauge location 1 (Fig. 28). The simulated peak stresses can be seen to match the experiments quite well (∼0.95 GPa), being most similar to shot 46, but a little higher than the mean stress of 0.88 GPa.

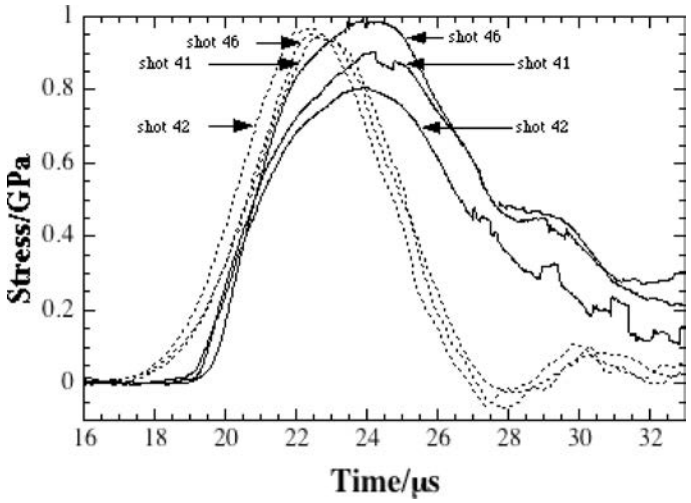

FIG. 28. Comparison of modelling with experiment for the output of manganin stress gauges 90 mm from the impact end for three hemispherical-ended 10 mm diameter tungsten rods impacted by 5 mm thick RHA steel plates. The solid lines are the experimental results; the dotted lines are the simulations. Experimental conditions: shot 41: normal impact, 533 m s^{-1}; shot 42: normal impact, 833 m s^{-1}; shot 46: 45°, 810 m s^{-1}.

The elastic wave velocity used in the model was determined from ultrasonic measurements on a plate made from the same tungsten alloy. This value appears to be a little higher than the elastic wave velocity in the rod, leading to a slightly early arrival (about 2 μs) of both the compression wave and subsequent release wave, and thus to shorter pulse durations. The simulations also show more gradual and prolonged rises at the start, and the experiments exhibit more gradual ends to the rising phase. However, the maximum rates of stress rise are similar in both the simulations and experiments, indicating wave dispersion has been modelled quite well. The simulated pulses are more symmetrical with time than the experimental ones, but then the latter appear disturbed and noisy after about 27 μs and are, hence, probably unreliable after this, so the experimental pulse shape is not certain after this time.

However, unlike gauges, modelling can give information about the stresses at many points within the rod. Figure 29 shows the predicted stress distribution within the rod and plate for shot 41 for three times after impact. The top section of each frame is the simulation corresponding in time to the frames selected

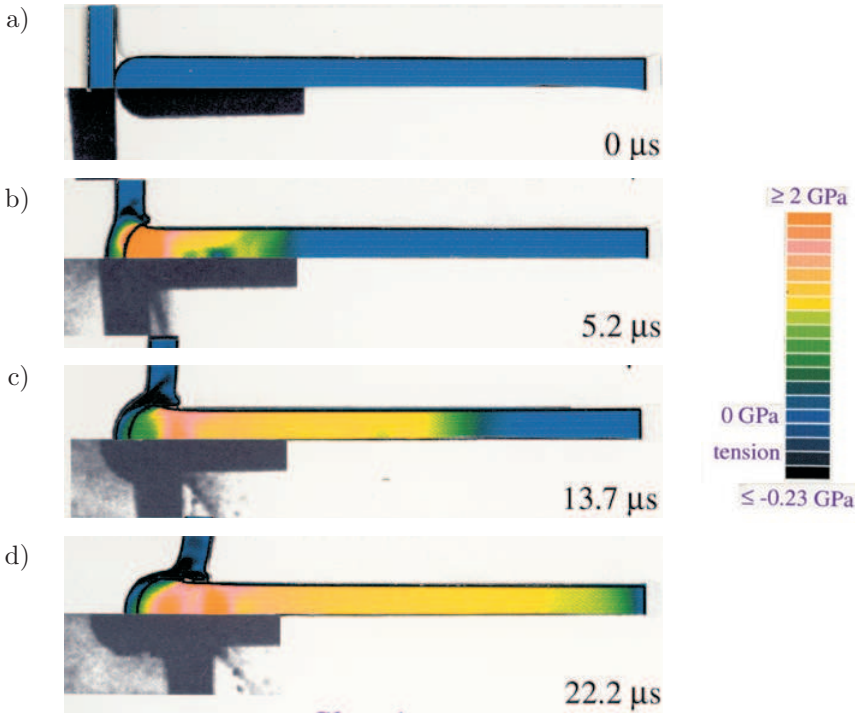

FIG. 29. Comparison of the simulated and experimental rod profiles of shot 41 (round-nosed tungsten alloy rod impacted normally by 5 mm thick RHA steel plate at 533 m s^{-1}. The colours indicate the stress levels (key given in right part of figure).

from the high-speed photographic record (bottom section). Only part of the rod lengths is shown. The elastic wavefront structure can be seen to become more planar in each successive frame and appears to be almost flat in profile by nine diameters (the location of gauge 1). As may be seen from Fig. 23, the high-speed photographs show the plate obliquely. Hence, the plate appears thicker than it truly is.

Note that when making a visual comparison between experiment and simulation the rear face of the plate can be seen in the photographs presented in frames (*a*) and (*b*). Note also that jetting of material was not incorporated in the simulation. The simulation overestimated the penetration time, probably because failure by ASBs and fracture was not incorporated. The simulation also overpredicted the extent of plate dishing (see particularly frame (*d*)). The reason failure mechanisms were not incorporated in the modelling was that the aim was to compare the simulations with the experimentally determined deformation of the rod and plate at early times. Since the Euler codes feature more than one material in a cell, then a manifestation of failure can be observed when the volume of the material falls below a set tolerance level in that cell.

Figure 30 presents a similar comparison between experiment and modelling for an oblique impact experiment (shot 46). One obvious difference to the normal impact case is the complexity of stress wave activity close to the nose of the rod even at short times. However, the stress wave again settles down to a more planar shape by the position of the first gauge location giving confidence that the stress pulses were recorded accurately. By frame (*d*) the elastic wave has returned to the nose, reflected, and is travelling back towards the rear a second time. In frames (*b*) and (*c*) the stress in the plate has concentrated on one side of the rod. Also the rod has flattened asymmetrically. However, by frame (*d*) the rod has self-sharpened. RECHT [51] suggested that deformed rods typically shear off material so that their final diameter is no greater than 125% of the original. Again the simulation predicts a faster penetration than actually occurred, though much of the detail as to what is going on is hidden by debris in the photographic sequences.

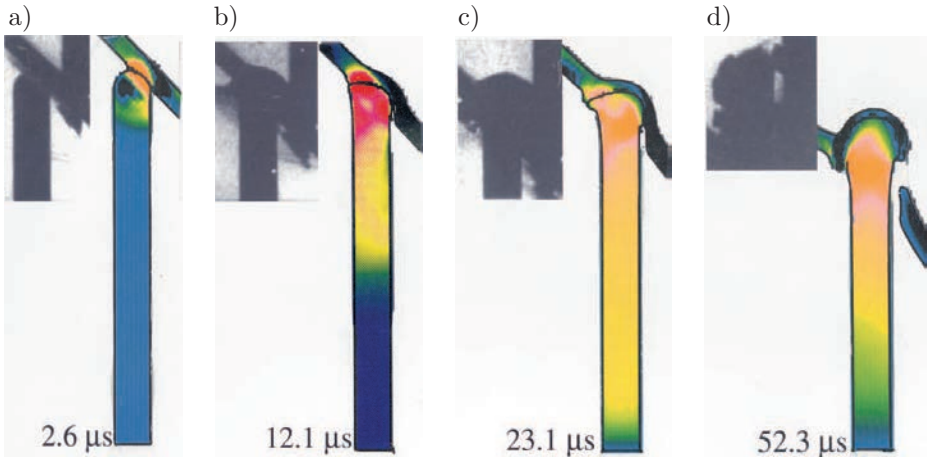

FIG. 30. Comparison of the simulated and experimental rod profiles of shot 46 (round-nosed tungsten alloy rod impacted at 45° by 5 mm thick RHA steel plate at 810 m s^{-1}. The same colour coding of stress was used as for Fig. 29.

To summarise, modelling is invaluable for giving insight into wave structures within the rod whereas experiments aid in 'tuning' the parameters of the constitutive model. They thus complement each other well.

6. CONCLUSIONS

Small-scale reverse ballistics experiments proved their worth in allowing the use of a wide range of diagnostics such as stress gauges, high-speed photography, and velocity interferometry (VISAR). These diagnostics provided a great

deal of information about plate perforation mechanisms. As the real materials used on the battlefield (RHA steel and tungsten) are expensive, we performed a study where less expensive pairs of materials with similar ratios of density and yield stress to determine whether these could be used in preliminary experiments to study the phenomenology of impact. We found that the less expensive materials were more ductile. Hence, the fracture behaviour of the real materials was not reproduced well, particularly in oblique impact. Even so, we found that the cheaper experiments can provide useful results before committing to more expensive, full-scale trials.

We also confirmed that it is possible to use stress gauges embedded in rods to measure dynamic mechanical properties of materials at low strains and at strain rates of between 10^2 and 10^3 s^{-1}. We found this was best done using thin ceramic plates and round-nosed rods. The patterns in the stress pulses often allow the impact parameters to be inferred as does high-speed photography of plate bulging or the deformation of in-plane grids. The results of stress gauge measurements were confirmed to be reproducible by performing repeat experiments and to be accurate by using VISAR. VISAR has a number of advantages over gauges in that it is more sensitive to low stress levels, has a faster response time, and can measure tensile release as well as compression. Dispersion of elastic waves affects both methods of measurement. Stress gauges are, however, cheaper and easier to use. They can also detect the exact time of impact if an electric pulse is given out by the impact process.

The numerical modelling that was performed confirmed the importance of including fracture if a predictive capability is required. This was particularly true for oblique impacts.

Acknowledgment

The research reported in this paper was funded by the British Ministry of Defence. We would like to thank Dr I.G. Cullis for providing guidance and computer modelling expertise. We would also like to thank past and present members of the Cavendish Laboratory's mechanical and electronic workshops for assistance with the design and construction of apparatus and specimens required for these experiments. LCF was supervised initially by Dr (now Professor) N.K. Bourne and then by Professor J.E. Field and Dr W.G. Proud.

References

1. M. E. Backman, W. Goldsmith, *The mechanics of penetration of projectiles into targets*, Int. J. Engng. Sci., **16**, 1–99, 1978.
2. M. F. Ashby, *A first report on deformation-mechanism maps*, Acta Metall., **20**, 887–898, 1972.

3. W. Goldsmith, S. A. Finnegan, *Penetration and perforation processes in metal targets at and above ballistic limits*, Int. J. Mech. Sci., **13**, 843–866, 1971.

4. S. G. Grantham, H. T. Goldrein, W. G. Proud, J. E. Field, *Digital speckle radiography: A new ballistic measurement technique*, Imaging Sci. J., **51**, 175–186, 2003.

5. L. C. Forde, W. G. Proud, S. M. Walley, P. D. Church, I. G. Cullis, *Ballistic impact studies of a borosilicate glass*, Int. J. Impact Engng., 37, 568–578, 2010.

6. J. I. Bluhm, *Stresses in projectiles during penetration*, Proc. Soc. Exptl. Stress Analysis, **13**, 2, 167–182, 1955.

7. L. M. Barker, R. E. Hollenbach, *Laser interferometer for measuring high velocities of any reflecting surface*, J. Appl. Phys., **43**, 4669–4675, 1972.

8. T. W. Burke, W. F. Rowe, *Bullet ricochet: A comprehensive review*, J. Forensic Sci., **37**, 1254–1260, 1992.

9. T. W. Bjerke, G. F. Silsby, D. R. Scheffler, R. M. Mudd, *Yawed long-rod penetration*, Int. J. Impact Engng., **12**, 281–292, 1992.

10. R. L. Landingham, A. W. Casey, *Final report of the light armor program*, Report no. UCRL-51269, Livermore, CA, Lawrence Livermore Laboratory, 1972.

11. H.-J. Ernst, K. Sterzelmeier, T. Wolf, R. Nüsing, *Reactive armor mechanisms against KE-threat: High explosives and electromagnetic forces*, [in:] Proc. 17th Int. Symp. on Ballistics, vol. 1, pp. 71–78, van Niekerk C. [Ed.], The South African Ballistics Organisation, Moreleta Park, South Africa, 1998.

12. G. Ben–Dor, A. Dubinsky, T. Elperin, *On the ballistic resistance of multi-layered targets with air gaps*, Int. J. Solids Structures, **35**, 3097–3103, 1998.

13. G. Ben–Dor, A. Dubinsky, T. Elperin, *Effect of air gap and order of plates on ballistic resistance of two layered armor*, Theor. Appl. Fract. Mech., **31**, 233–241, 1999.

14. T. J. Moynihan, J. C. LaSalvia, M. S. Burkins, *Analysis of the shatter gap phenomenon in a boron carbide/composite laminate armor system*, [in:] Proc. 20th Int. Symp. on Ballistics, National Defense Industrial Association, pp. 1096–1103, Carleone J., Orphal D. [Eds.], Lancaster, PA, 2002.

15. Z. Rosenberg, E. Dekel, *The relation between the penetration capability of long rods and their length to diameter ratio*, Int. J. Impact Engng., **15**, 125–130, 1994.

16. D. L. Orphal, R. R. Franzen, *Penetration mechanics and performance of segmented rods against metal targets*, Int. J. Impact Engng., **10**, 427–438, 1990.

17. G. Birkhoff, D. P. MacDougall, E. M. Pugh, G. I. Taylor, *Explosives with lined cavities*, J. Appl. Phys., **19**, 563–582, 1948.

18. J. A. Zukas [Ed.], *High Velocity Impact Dynamics*, Wiley, New York, 1990.

19. Z. Rosenberg, E. Dekel, *Strength effects in long-rod penetration*, [in:] Structures under Shock and Impact IV, pp. 137–148, Jones N., Brebbia C.A., Watson A.J. [Eds.], Computational Mechanics Publications, Southampton, UK, 1996.

20. Z. Rosenberg, E. Dekel, *On the role of material properties in the terminal ballistics of long rods*, Int. J. Impact Engng., **30**, 835–851, 2004.

21. T. Børvik, M. Langseth, O. S. Hopperstad, K. A. Malo, *Ballistic penetration of steel plates*, Int. J. Impact Engng., **22**, 855–886, 1999.

22. T. Børvik, S. Dey, O. S. Hopperstad, M. Langseth, *On the main mechanisms in ballistic perforation of steel plates at sub-ordnance impact velocities*, [in:] Predictive Modeling of Dynamic Processes, pp. 189–219, Hiermaier S. [Ed.], Springer, Berlin, 2009.

23. P. C. Chou, J. Hashemi, A. Chou, H. C. Rogers, *Experimentation and finite element simulation of adiabatic shear bands in controlled penetration impact*, Int. J. Impact Engng., **11**, 305–321, 1991.

24. J. Yu, X. Dong, J. Zhang, *A study of adiabatic shear plugging in Ti6Al4V alloy*, Key Engng. Mater., **177**, 387–392, 2000.

25. Y.-W. Lee, T. Wierzbicki, *Fracture prediction of thin plates under localized impulsive loading. 1: Dishing*, Int. J. Impact Engng., **31**, 1253–1276, 2005.

26. L. W. Kennedy, O. E. Jones, *Longitudinal wave propagation in a circular bar loaded suddenly by a radially distributed end stress*, Trans. ASME: J. Appl. Mech., **36**, 470–478, 1969.

27. D. A. Gorham, *Measurement of stress-strain properties of strong metals at very high strain rates*, Inst. Phys. Conf. Ser., **47**, 16–24, 1980.

28. L. C. Forde, N. K. Bourne, Z. Rosenberg, R. Cornish, N. J. Lynch, I. G. Cullis, P. D. Church, *Experimental investigation and analysis of penetration in oblique impact*, [in:] Proc. 16th Int. Symp. on Ballistics, vol. 3, pp. 641–649, American Defense Preparedness Association, Arlington, Virginia, 1996.

29. N. K. Bourne, Z. Rosenberg, D. J. Johnson, J. E. Field, A. E. Timbs, R. P. Flaxman, *Design and construction of the UK plate impact facility*, Meas. Sci. Technol., **6**, 1462–1470, 1995.

30. S. P. Marsh, *LASL Shock Hugoniot Data*, University of California Press, Berkeley, CA, 1980.

31. M. B. Lesser, *Analytic solutions of liquid-drop impact problems*, Proc. R. Soc. Lond. A, **377**, 289–308, 1981.

32. D.R. Andrews, J.E. Field, *The erosion of metals by the normal impingement of hard solid spheres*, J. Phys. D: Appl. Phys., **15**, 571–578, 1982.

33. J. E. Field, M. B. Lesser, J. P. Dear, *Studies of two-dimensional liquid-wedge impact and their relevance to liquid-drop impact problems*, Proc. R. Soc. Lond. A, **401**, 225–249, 1985.

34. Y. L. Bai, B. Dodd, *Adiabatic Shear Localization: Occurrence*, Theories and Applications, Pergamon, Oxford, 1992.

35. S. M. Walley, *Shear localization: A historical overview*, Metall. Mater. Trans. A, **38**, 2629–2654, 2007.

36. J. P. Dear, *Use of high-speed photography in the evaluation of polymer materials*, Proc. SPIE, **1358**, 37–42, 1990.

37. W. G. Proud, N. Lynch, A. Marsh, J. E. Field, *Instrumented smallscale rod penetration studies: The effect of pitch*, [in:] Proc. 19th Int. Symp. on Ballistics, pp. 1289–1295, Crewther I.R. [Ed.], Interlaken, Switzerland, 2001.

38. G. R. Willmott, D. D. Radford, *Taylor impact of glass rods*, J. Appl. Phys., **97**, 093522, 2005.

39. D. J. Chapman, D. D. Radford, M. Reynolds, P. D. Church, *Shock induced void nucleation during Taylor impact*, Int. J. Fract., **134**, 41–57, 2005.

40. Z. Rosenberg, S. J. Bless, *Determination of dynamic yield strengths with embedded manganin gages in plate-impact and long-rod experiments*, Exper. Mech., **26**, 279–282, 1986.

41. Z. Rosenberg, S. Bless, *Stress wave measurements in impulsively loaded long steel rods with embedded manganin gauges*, [in:] Proc. Int. Symp. on Intense Dynamic Loading and its Effects, pp. 742–746, Zheng Z., Ding J. [Eds.], Pergamon, Oxford, 1988.

42. L. Pochhammer, *Über Fortpflanzungsgeschwindigkeiten kleiner Schwingungen in einem unbegrenzten isotropen Kreiszylinder*, J. reine angew. Math., **81**, 324–336, 1876.

43. C. Chree, *The equations of an isotropic elastic solid in polar and cylindrical coordinates: Their solution and application*, Trans. Cambridge Philos. Soc., **14**, 250–369, 1889.

44. N. A. Safford, Materials testing up to 10^5 s^{-1} using a miniaturised Hopkinson bar with dispersion corrections, [in:] Proc. 2nd. Int. Symp. on Intense Dynamic Loading and its Effects, pp. 378–383, Zhang G., Huang S. [Eds.], Sichuan University Press, Chengdu, P.R. China, 1992.

45. G. T. Gray III, *Classic split-Hopkinson pressure bar testing*, [in:] ASM Handbook. 8: Mechanical Testing and Evaluation, pp. 462–476, Kuhn H., Medlin D. [Eds.], ASM International, Materials Park, Ohio, 2000.

46. P. D. Church, I. Cullis, *Development and application of high strain rate constitutive models in hydrocodes*, J. Phys. IV France, **1**, (C3), 917–922, 1991.

47. P. D. Church, T. Andrews, B. Goldthorpe, *A review of constitutive model development within DERA*, [in:] Structures under Extreme Loading Conditions (PVP 394), pp. 113–120, Jerome D.M. [Ed.], American Society of Mechanical Engineers, New York, 1999.

48. E. C. Cameron, D. C. Barton, T. D. Andrews, P. D. Church, *An experimental and numerical study of the ductile fracture process for rolled homogeneous armour alloy steel*, J. Phys. IV France, **10** (Pr. 9), 209–214, 2000.

49. L. C. Forde, W. G. Proud, S. M. Walley, *Symmetrical Taylor impact studies of copper*, Proc. R. Soc. A, **465**, 769–790, 2009.

50. L. C. Forde, S. M. Walley, M. Peyton–Jones, W. G. Proud, I. G. Cullis, P. D. Church, *The use of symmetric Taylor impact to validate constitutive models for an fcc metal (copper) and a bcc alloy (RHA steel)*, [in:] Proc. 9th Int. Conf. on the Mechanical and Physical Behaviour of Materials under Dynamic Loading (DYMAT 2009), pp. 1245–1250, EDP Sciences, Les Ulis, France, 2009.

51. R. F. Recht, *Taylor ballistic impact modelling applied to deformation and mass loss determinations*, Int. J. Engng Sci., **16**, 809–827, 1978.

Received January 5, 2011; revised version July 19, 2011.

ENGINEERING TRANSACTIONS • *Engng. Trans.* • **59**, 3, 197–210, 2011
Polish Academy of Sciences • Institute of Fundamental Technological Research (IPPT PAN)
National Engineering School of Metz (ENIM)

STRAIN RATE BEHAVIOUR OF THREE ROCKS IN TENSION

E. Cadoni, S. Antonietti, M. Dotta, D. Forni

University of Applied Sciences of Southern Switzerland
DynaMat Laboratory
Switzerland

The paper presents the dynamic characterization in tension of three rocks under medium and high strain-rates. The tests have been carried out by means of the JRC-Split Hopkinson Tension Bar and an Hydro-Pneumatic Machine, installed in the DynaMat Laboratory of the University of Applied Sciences of Southern Switzerland. The dynamic direct tension tests have been performed at 3 different strain rates (0.1, 10, 100 strain/second) on an orthogneiss, for loading directions 0°, 45° and 90° respect to the schistosity, and two different types of marble. Results of the tests show a significantly strain-rate sensitive behaviour, exhibiting dynamic tensile strength increasing with strain-rate. In order to describe the strain rate behaviour of these rocks, the dynamic increase factors in function of the strain rates for tensile strength have been used.

1. Introduction

The mechanical response of rocks under high loading rates is of fundamental importance in tunnel constructions and mining works. The dynamic loading is generated by impact loading of the tools of specialized excavation machines and/or by controlled explosions. The knowledge of the real material constitutive relationships can allow the optimization of the explosive charge and consequent pressure wave amplitude and duration. This fact is important both for economic reasons, to obtain the desired effect with the lowest cost, and for safety measures, in order to avoid risks of heavy vibrations, especially in case of underground excavations in urban areas.

The modern tools used in design and assessment of constructions (i.e. FE codes) require more and more advanced data, as for example the complete stress versus strain curves, until fracture of the rock materials or the implementation of different material constitutive laws. These data have to be measured by means of specialized apparatus able to properly measure the characteristics of the materials. In particular, at high strain rates it is necessary to generate a stress wave pulse well controlled in amplitude and duration, as well as at medium strain rates, the vibration of the systems should be under control. The dynamic

tension test is normally obtainable by Split Hopkinson Pressure Bar (SHPB) device, in the strain range of 10^2–10^3 s^{-1}. With this apparatus only indirect measurement of the tensile strength can be available, because it works in compression (splitting test, spalling test, etc.). Some modifications were used by different authors in order to obtain direct pulse [1–4] for rock-like materials as concrete.

The dynamic direct tensile test has been obtained using a modification of the previous apparatus [5–7] for the characterization of concrete and rocks [8–10].

The dynamic direct tensile strength of an orthogneiss has been measured at 3 different strain rates (0.1, 10, 100 strain/second) for loading directions 0°, 45° and 90° with respect to the schistosity. The two marbles have been characterized at three strain rate regimes: quasi-static, medium and high strain rates.

The tests have been carried out by means of the JRC-Split Hopkinson Tension Bar and the JRC-Hydro-Pneumatic Machine, installed in the DynaMat Laboratory of the University of Applied Sciences of Southern Switzerland.

2. Experimental program

Static and dynamic loading tests have been conducted on cylindrical rock specimens (diameter = 20 mm, height/diameter = 1). In the case of orthogneiss, series of cores have been drilled out in three directions: the first parallel ($\theta = 0°$) and the second perpendicular ($\theta = 90°$) to the plane of schistosity, the third sampling direction oriented at $\theta = 45°$ to the plane of schistosity. As a result θ is then defined as the angle of schistosity with the loading direction, as shown in Fig. 1.

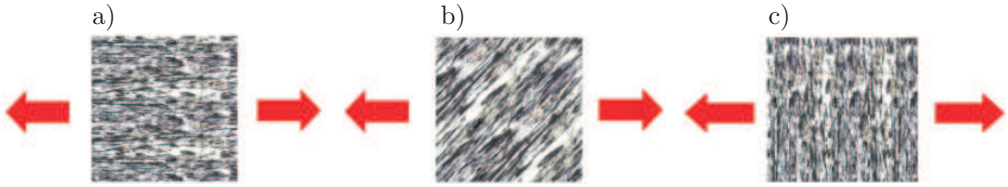

Fig. 1. Loading direction to the schistosity plane: a) $\theta = 0°$, b) $\theta = 45°$, c) $\theta = 90°$.

2.1. Materials

The rock materials used for testing are two rocks from the Swiss Alps and the well-known Carrara marble. The Swiss rocks are an orthogneiss from the Onsernone Valley and a Peccia marble from the Maggia Valley of the Canton Ticino (Switzerland). They belongs to the group of the metamorphous rocks.

The petrography of the Onsernone orthogneiss is characterized by the presence of white feldspar (albite) and transparent quartz appear in the light min-

erals, as well as are also included a relatively large quantity of white mica (muscovite) and dark mica (biotite), even if this is not evenly distributed. The mean grain size of the crystals is about 0.5 mm while the maximum grain size is 1 mm (see Fig. 2a).

The two marbles are characterized by a granoblastic structures, the Peccia marble (see Fig. 2b) present larger size of grain (about 1 mm) with respect to the Carrara marble (see Fig. 2c), having maximum grain size of about 0.2 mm.

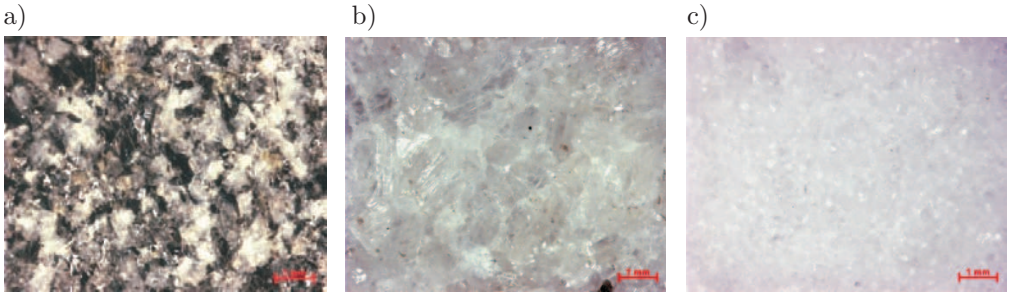

FIG. 2. Microcrystalline structure of the: a) Onsernone orthogneiss, b) Peccia marble, c) Carrara marble.

In order to compare dynamic and quasi-static regime directly, excluding the results of any size effect influence, tensile static tests has been measured on 20 mm diameter 20 mm high specimens (the same geometry of the dynamic tests).

The results of the material characteristics are summarized in Table 1.

Table 1. Mechanical characteristics.

Rock material	Apparent density [kg/m^3]	Absolute density [kg/m^3]	Young's modulus [GPa]	Compression strength [MPa]	Tensile strength [MPa]
Onsernone orthogneiss	2710	2740	39.3 ($\theta = 0°$)	189±8 ($\theta = 0°$) 203±7 ($\theta = 90°$)	12.6±0.5 ($\theta = 0°$) 6.1±0.8 ($\theta = 45°$) 2.6±1.1 ($\theta = 90°$)
Peccia marble	2706	2795	64.6	87±8	3.9±0.4
Carrara marble	2677	2720	–	79±1	2.0±0.5

3. Experimental set-ups for dynamic testing

3.1. The JRC-Split Hopkinson Tensile Bar (JRC-SHTB)

The JRC-SHTB used for rocks characterization at high strain rate consists of two circular aluminum bars, called input and output bars, having respectively the length of 3 m and 6 m, with a diameter of 20 mm, to which the specimen

is glued by using a bi-component epoxy resin. The input bar is connected with a high strength steel pre-tensioned bar 6 m in length, used as pulse generator with a diameter of 12 mm in order to obtain the same acoustical impedance of the input bar, so that the pulse reflection, due to the interface, is avoided.

With reference to Fig. 3, a test with the JRC-SHTB is performed as follows:

a) first a hydraulic actuator (1), of maximum loading capacity of 600 kN, is pulling the pre-tension high strength steel bar (2); the pre-tension stored in this bar is resisted by the blocking device (3);

b) second operation is the rupture of the fragile bolt in the blocking device which gives rise to a tensile mechanical pulse of 2.4 ms duration with linear loading rate during the rise time, propagating along the input (4) and output (7) bars, bringing to fracture the specimen (6).

The pulse propagates along the input bar with the velocity C_0 of the elastic wave with its shape remaining constant. When the incident pulse (ε_I) reaches the rock specimen, part of it (ε_R) is reflected by the specimen whereas another part (ε_T) passes through the specimen propagating into the output bar.

The relative amplitudes of the incident, reflected and transmitted pulses, depend on the mechanical properties of the specimen. Strain-gauges glued on the input and output bars of the device are used for the measurement of the elastic deformation (as a function of time), created on both half-bars respectively by the incident/reflected and transmitted pulses.

FIG. 3. High strain-rate tensile tests on specimen Ø = 20 mm.

This modified system still satisfies the condition of applicability of the uniaxial elastic wave propagation theory because the pulse wavelength (in order of a few meters) is much higher than the transverse length of the bar (20 mm), so the stress-strain history can be obtained by the following equations:

$$\sigma(t) = E_0 \frac{A_0}{A_s} \varepsilon_T(t), \tag{3.1}$$

$$\varepsilon(t) = -\frac{2 \cdot C_0}{L_s} \int_0^t \varepsilon_R(t) dt \tag{3.2}$$

where L_s – specimen length; A_s – specimen cross-section area; A_0 – output bar cross-section area; t – time.

3.2. The Hydro-Pneumatic Machine (HPM)

The medium strain rate tests have been carried out by means of a Hydro-Pneumatic Machine (HPM). The employed HPM is shown in Fig. 4. At the beginning of the test, a sealed piston divides a cylindrical tank in two chambers; one chamber (4) is filled with gas at high pressure (e.g. 150 bars), the other one (5) is filled with water. At the beginning, equal pressure is established in

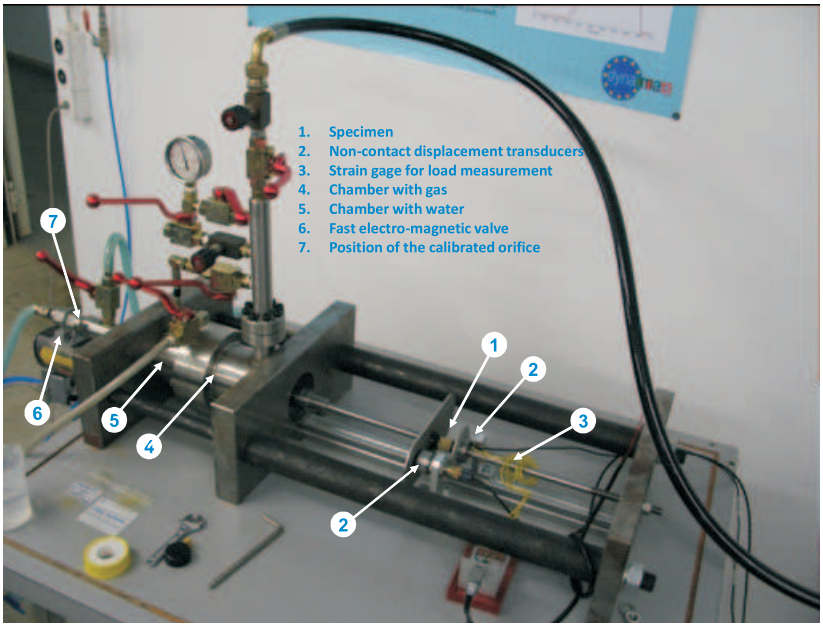

FIG. 4. Hydro-pneumatic machine used for medium strain-rate.

the water and gas chambers, so that forces acting on the two piston faces are in equilibrium. The test starts when the second chamber discharges the water through a calibrated orifice (7), activated by a fast electro-valve (6). Then, the piston starts moving expelling out the gas through a sealed opening; the end of the piston shaft is connected to the rock specimen (1); the specimen is linked to the piston shaft and to one end of an elastic bar (3), whose other end is rigidly fixed to a supporting structure. When the piston shaft moves, the specimen is pulled at a fixed strain-rate level, depending on the velocity of the gas expelling from the chamber. The elastic bar is instrumented with a strain-gauge (3) that provides, through the elastic properties of the bar, the force acting on the specimen during the test. Two targets are attached on both ends of the specimen and their movements are measured by two contact-less displacement transducers (2).

The constant speed movement of the piston guarantees the constancy of the strain-rate during the test; this depends mainly on the constancy of the force exerted by the gas pressure on the piston face. A good result in this sense was obtained with small change of gas volume during the test in order to have small gas pressure decrease and consequently small piston force decrease. Furthermore, the load P resisted by the specimen is measured by the dynamometric elastic bar, whereas the specimen elongation ΔL is measured by the displacement transducers, sensing the displacement of the plates target fixed to both specimen ends. Such acquisitions allow to obtain the stress vs. strain relationship at the strain-rate level, achieved during the test.

4. Results and discussion

The strain rate behaviour of the orthogneiss rock (for $\theta = 0°$, $45°$ and $90°$) and two marbles are here described with the results obtained by the two dynamic testing set-ups and the quasi-static results.

4.1. High strain rate results

All results of the tests at high strain rate carried out by the JRC-SHTB are summarized in Table 2. All the tests have been performed keeping the preload constant (18 kN); in this way, the rocks were tested under the same loading condition. The strain rate behaviour of the orthogneiss has been analysed in three θ orientations: $\theta = 0°$, $\theta = 45°$ and $\theta = 90°$. The measurements of the strain histories of the input and output bars were used for determination of the stress versus strain curves by the Eqs. (3.1) and (3.2). In Fig. 5 are shown the stress versus strain curves of the orthogneiss (a) for $\theta = 0°$, $\theta = 45°$ and $\theta = 90°$ and the two Carrara and Peccia marbles (b). These diagrams con-

Table 2. High strain rate results.

Rock material	Dynamic Tensile Strength $f_{t,d}$ [MPa]	Average value f_{t,d_ave} [MPa]	Fracture Energy $G_{f,d}$ [J/m^2]	Average value G_{f,d_ave} [J/m^2]	Stress rate [GPa/s]
Orthogneiss $\theta = 0°$_N1	25.71		1260		1161
Orthogneiss $\theta = 0°$_N2	24.96	25.45±0.4	1146	1304±183	1151
Orthogneiss $\theta = 0°$_N6	25.70		1505		870
Orthogneiss $\theta = 45°$_N3	8.07		414		405
Orthogneiss $\theta = 45°$_N4	16.86	13.52±4.7	1154	868±397	788
Orthogneiss $\theta = 45°$_N7	15.65		1036		737
Orthogneiss $\theta = 90°$_N1	6.50		691		257
Orthogneiss $\theta = 90°$_N4	9.56	8.67±1.9	801	712±81	545
Orthogneiss $\theta = 90°$_N6	9.96		643		534
Peccia_Marble_N1	11.50		302		719
Peccia_Marble_N3	12.47	12.04±0.5	378	355±46	676
Peccia_Marble_N4	12.30		384		658
Carrara_Marble_N1	6.49		368		223
Carrara_Marble_N2	8.74	7.08±1.4	441	380±56	390
Carrara_Marble_N3	6.02		330		187

firm that the JRC-SHTB is able to measure both the ascending and descending branch of the curve and permits to measure the fracture energy (computed as the subtended area in a stress-displacement curve). For the orthogneiss analysed, the fracture energy changes with the orientation of schistosity at high strain rates. Higher values are observed for the $\theta = 0°$, while lower values are for $\theta = 90°$, then fracture energy reveals an increasing trend with the orientation. This increase in fracture energy shows that at $\theta = 0°$ this orthogneiss is more ductile [9]. In order to understand better the ductility and/or brittleness of this material, the characteristic length should be considered. As a unique material property, the characteristic length $l_{ch} = G_F \cdot E/f_t^2$ expresses fracture of concrete-like materials, which is inversely proportional to the square of the tensile strength. This means that brittleness decreases with high fracture energy and increases with an increase of strength of the material. The values at $\theta = 0°$, $\theta = 45°$ and $\theta = 90°$ are respectively 79 mm, 192 mm and 413 mm [9]. The lower value is for $\theta = 0°$ revealing less brittle behaviour with respect to the other two ($\theta = 90°$ and $\theta = 45°$). The brittleness increases also with the strain rate [8].

a)

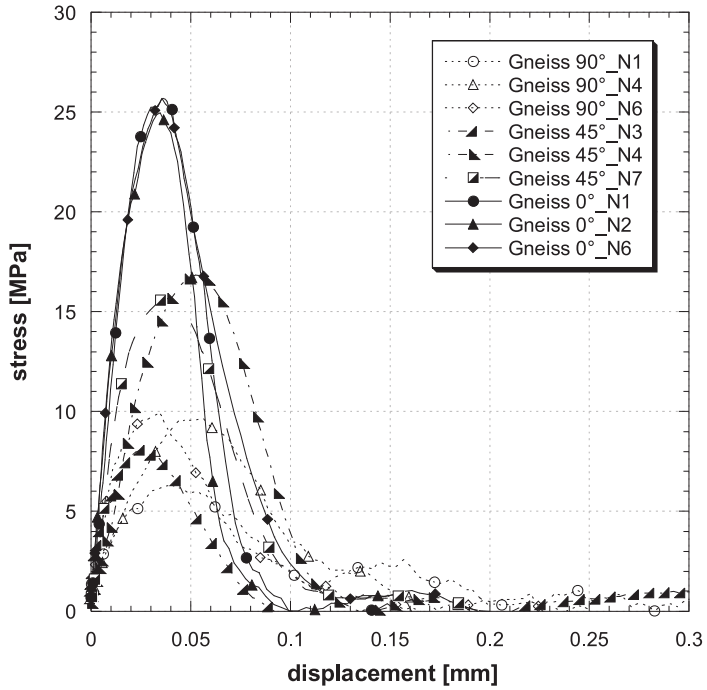

b)

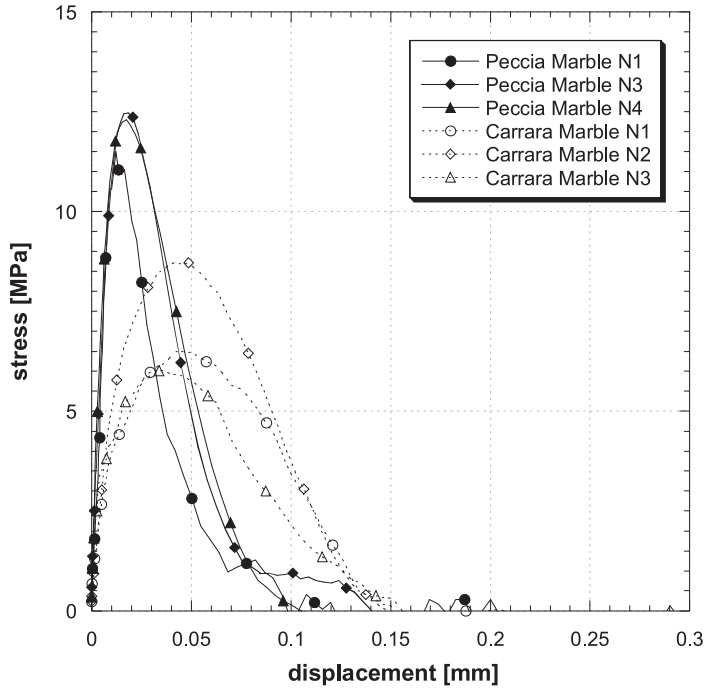

FIG. 5. Stress versus displacement curves of: a) orthogneiss, b) marbles.

In Fig. 6 are shown the photos of the Onsernone orthogneiss (a) and the Carrara marble (b) after the dynamic test with the JRC-SHTB.

a)

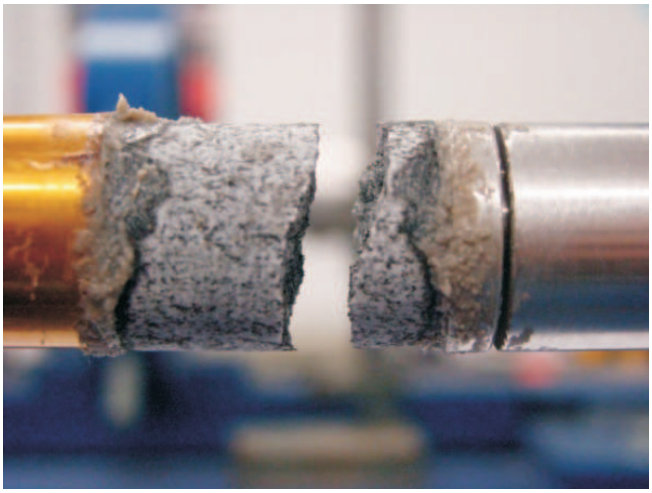

b)

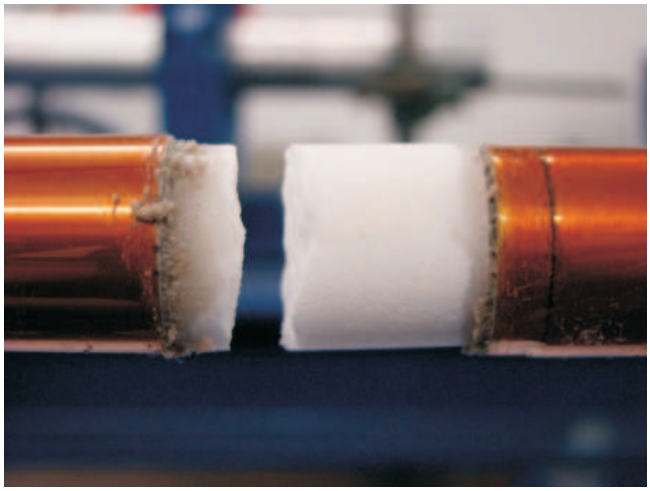

FIG. 6. Specimen after dynamic test: a) Orthogneiss, b) Carrara marble.

4.2. Medium strain rate results

The medium strain rate has been studied using a HPM with different calibrated orifices, having diameters from 1 mm to 3 mm. With the smaller diameter has been obtained lower intermediate velocity (about 200 MPa/s), while with the larger diameter has been obtained higher intermediate velocity (about 1500 MPa/s). The results are collected in Table 3. The tests have been carried out in tension for the same three θ orientations 0°, 45° and 90° of the orthogneiss.

Table 3. Medium strain rate results.

ID	Orifice diameter [mm]	Dynamic Tensile Strength $f_{t,d}$ [MPa]	Average f_{t,d_ave} [MPa]	Stress rate obtained [GPa/s]
Orthogneiss $\theta = 0°$_N3	3	19.78		1.752
Orthogneiss $\theta = 0°$_N4	3	17.56	17.39±2.4	1.370
Orthogneiss $\theta = 0°$_N7	3	14.82		1.439
Orthogneiss $\theta = 0°$_N8	1	16.88		0.185
Orthogneiss $\theta = 0°$_N9	1	15.19	15.77±0.9	0.207
Orthogneiss $\theta = 0°$_N13	1	16.38		0.191
Orthogneiss $\theta = 45°$_N1	3	8.66		1.401
Orthogneiss $\theta = 45°$_N2	3	10.72	8.92±1.2	1.457
Orthogneiss $\theta = 45°$_N8	3	8.20		1.514
Orthogneiss $\theta = 90°$_N2	3	2.26		1.665
Orthogneiss $\theta = 90°$_N3	3	4.42	4.21±1.8	1.354
Orthogneiss $\theta = 90°$_N7	3	5.96		1.525
Orthogneiss $\theta = 90°$_N8	1	4.56		0.201
Orthogneiss $\theta = 90°$_N9	1	1.91	3.73±1.6	0.116
Orthogneiss $\theta = 90°$_N11	1	4.95		0.193
Carrara_Marble_N7	2	4.15		0.998
Carrara_Marble_N8	2	3.92		1.035
Carrara_Marble_N9	2	3.72		0.734
Carrara_Marble_N10	2	4.66	4.42±0.8	0.918
Carrara_Marble_N11	2	4.12		0.980
Carrara_Marble_N12	2	5.96		1.013
Peccia_Marble_N11	2	4.43		0.784
Peccia_Marble_N12	2	5.91	5.80±1.3	0.979
Peccia_Marble_N13	2	7.07		0.939

4.3. Strain rate effect

Analysing the results at different strain rates it can be immediately observed that there is a dramatic difference in the strengths between the quasi-static and dynamic loading.

In Fig. 7 is shown the comparison between the static and dynamic stress versus displacement curves of Carrara Marble. For the rocks analysed, the dynamic strength at high strain rate is at least twice that of the static strength, indicating that rock reacts quite differently to dynamic loading than to static

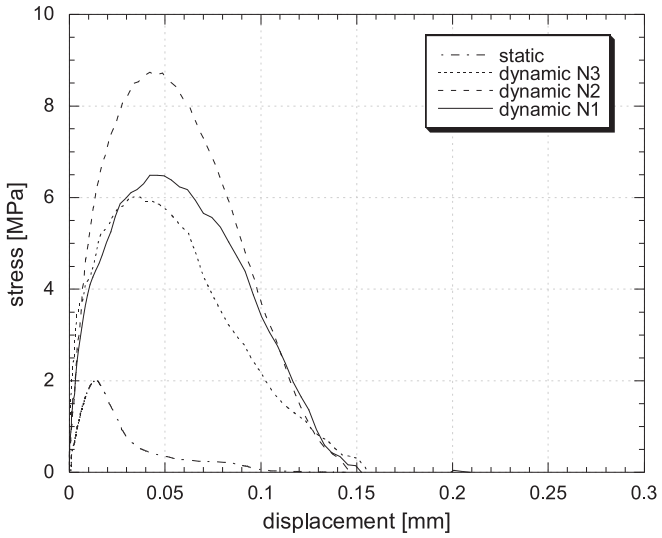

FIG. 7. Quasi-static and dynamic stress vs. displacement curves of Carrara Marble.

loading. The Carrara marble respond to the high loading rate with an increment of absorbed energy and larger deformation; all these effects can be attributed to the dynamic failure process.

The fracture processes of rocks are not the same under the static and dynamic types of loading as for concrete [5–7]. The rapid increase in terms of strength with increase in rate of loading has been explained through the impossibility for the weakest links in the rock to participate in the fracturing process. In fact, they may not necessarily have the time to propagate following the minimum energy path due to the nature of the dynamic fracturing process, that involves a complex interaction of multiple crack growth [6]. The test results show how the loading rate effect is governed by the wave propagation in the material in dynamic case (high strain rate), while in the quasi-static case the cracking process is governed by the defect and preferential plane of fracture eventually present in the rocks.

The strain-rate behaviour on the tensile strength can be represented through the ratio between the dynamic and static strength, well-known as Dynamic Increase Factor (DIF). It has been found that DIF of strength increase with strain rate. This ratio is usually higher for low strength rocks, and lower for high strength rocks.

DIF has been extensively used in order to quantify strain-rate effects for concrete-like materials in a large number of experimental researches. From these results some expressions of the DIF of the tensile strength have been developed but unfortunately, these do not consider any corrections taking into considera-

tion the type of materials (grain size, specimen size, etc.), neither the type of experimental set-up used to determine the dynamic tensile strength. In the case of compression [11] it is known that the dynamic strength of rocks at strain rates higher than 10^2 s^{-1} can be expressed as $\sigma_d = K(d\varepsilon/dt)^{1/3}$. In the case of tension, this assumption cannot be accepted because of fracture behaviour that strictly depends to the nature of the rocks.

Figure 8 illustrates the increase of the DIF versus strain rate, obtained by other researchers [9] and of the rocks here considered. It is shown that at lower strain rates, the strength increase is gradual above a certain strain rate, whilst this increase is drastic for higher strain rates. This transition seems to be present in the lower strength rocks and might be less marked for the higher strength rocks. This transition may be dependent on rock type and loading.

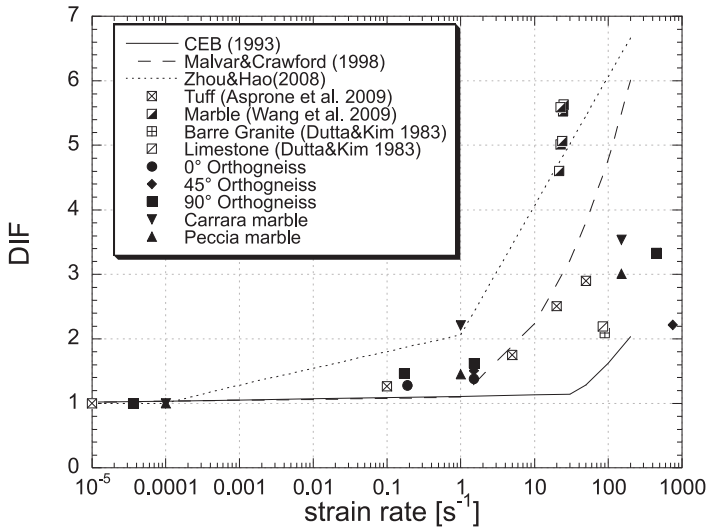

FIG. 8. DIF vs. strain rate.

In Fig. 8 are shown some formulations proposed for rocks and concrete [12], but it confirms that a more suitable formulation is necessary for rocks and that a wide experimental campaign on different families of rocks is needed.

5. Concluding remarks

Dynamic direct tensile tests of an orthogneiss and two marbles were conducted using the JRC-Split Hopkinson Tensile Bar, and Hydro Pneumatic Machine for dynamic testing and an electro-mechanic machine for quasi-static tests. Results show that rock tensile strength is strain-rate dependent.

The mechanism of failure under dynamic loading by stress wave is significantly different from the quasi-static loading. Dynamic loading produces multiple fractures and this brings the material to absorb more energy, because higher loads are required to complete failure.

It has been verified that for the orthogneiss the tensile strength increases with the strain rate increasing within the wide strain rate range. The results show a non-linear relationships between strength and strain rates and the influence of the loading direction with respect to the schistosity of the orthogneiss examined. No influence were observed for the marbles.

Finally, the results confirm that a more appropriate formulation is necessary to describe the dynamic tensile strength evolution in function of the strain rate for rocks. Future research will be addressed to increase the knowledge on the dynamic behaviour of other rock types and in a wide range of strain rates using the experimental techniques presented here.

References

1. A. J. Zielinski, *Fracture of concrete and mortar under uniaxial impact tensile loading*, D.Sc. Thesis, Delft Univ., 1982.
2. H. W. Reinhardt, H. A. Körmeling, A. J. Zielinski, *The split Hopkinson bar, a versatile tool for the impact testing of concrete*, Materiaux et Constructions, **19**, 1, 55–63, 1986.
3. J. R. Klepaczko, A. Brara, *Experimental method for dynamic tensile testing of concrete by spalling*, International Journal of Impact Engineering, **25**, 387–409, 2001.
4. H. Schuler, C. Mayrhofer, K. Thoma, *Spall experiments for the measurement of the tensile strength and fracture energy of concrete at high strain rates*, International Journal of Impact Engineering, **32**, 1635–1650, 2006.
5. C. Albertini, E. Cadoni, K. Labibes, *Dynamic mechanical behaviour of large concrete specimen by means of a bundle Hopkinson bars*, Proc. 2nd Int. Sym. on Impact Engineering, Chinese Mechanics Journal, Beijing, pp. 214–219, 1996.
6. C. Albertini, E. Cadoni, K. Labibes, *Impact fracture process and mechanical properties of plain concrete by means of an Hopkinson bar bundle*, Journal de Physique, **7**, C3, 915–920, 1997.
7. E. Cadoni, G. Solomos, A. Albertini, *Mechanical characterization of concrete in tension and compression at high strain-rate using a modified Hopkinson bar*, Magazine of Concrete Research, **61**, 3, 221–230, 2009.
8. D. Asprone, E. Cadoni, A. Prota, G. Manfredi, *Dynamic behavior of a Mediterranean natural stone under tensile loading*, International Journal of Rock Mechanics and Mining Sciences, **46**, 514–520, 2009.
9. E. Cadoni, *Dynamic Characterization of an Orthogneiss Rock Subjected to Intermediate and High Strain Rate in Tension, accepted for publication*, Rock Mechanics and Rock Engineering, 2010.

10. E. Cadoni, M. Dotta, D. Forni, P. Giorgetti, G. Riganti, C. Albertini, *Mechanical characterization of rocks at high strain rate by the JRC modified Hopkinson bar: A tool in blast and impact assessment*, Rock Fragmentation by Blasting – Sanchidrián [Ed.], 2009, Taylor & Francis Group, London, ISBN 978-0-415-48296-7, pp. 35–41.

11. S. Kubota, Y. Ogata, Y. Wada, G. Simangunsong, H. Shimada, K. Matsui, *Estimation of dynamic tensile strength of sandstone*, International Journal of Rock Mechanics and Mining Sciences, **45**, 397–406, 2008.

12. Comité Euro-International du Béton (1993), CEB-FIP Model Code 1990, Redwood Books, Trowbridge, Wiltshire, UK.

Received January 20, 2011; revised version June 4, 2011.

ENGINEERING TRANSACTIONS • *Engng. Trans.* • **59**, 3, 211–233, 2011
Polish Academy of Sciences • Institute of Fundamental Technological Research (IPPT PAN)
National Engineering School of Metz (ENIM)

FE ANALYSIS ON THE FORMATION OF PLASTIC INSTABILITIES IN DYNAMICALLY EXPANDED COPPER RINGS

C. Vela [1)], J.A. Rodríguez–Martínez [1)], A. Rusinek [2)]

[1)] **University Carlos III of Madrid**
Department of Continuum Mechanics and Structural Analysis
Avda. de la Universidad 30, 28911 Leganés, Madrid, Spain

[2)] **National Engineering School of Metz (ENIM)**
Laboratory of Mechanics, Biomechanics, Polymers and Structures (LaBPS)
1 route d'Ars Laquenexy, 57078 Metz Cedex 3, France
e-mail: rusinek@enim.fr

In this work the influence of the constitutive description in numerical simulations of the radial expansion of annealed **OFHC** copper rings has been studied. For that task, three physical-based constitutive models are implemented into the **FE** code ABAQUS/Explicit and applied to define the thermo-viscoplastic behaviour of the material in the simulations. These are those due to Rusinek *et al.* [A. Rusinek, J. A. Rodríguez–Martínez, A. Arias, *A thermo-viscoplastic constitutive model for FCC metals with application to OFHC copper*, Int. J. Mech. Sci., **52**, 120–135, 2010], Nemat–Nasser and Li [S. Nemat–Nasser, Y. Li, *Flow stress of FCC polycrystals with application to OFHC Copper*, Acta Mater., **46**, 565–577, 1998] and Voyiadjis and Almasri [G. Z. Voyiadjis, A. H. Almasri, *A physically based constitutive model for fcc metals with applications to dynamic hardness*, Mech. Mater., **40**, 549–563, 2008]. The attention is primarily focussed on analyzing the influence of the material description on the strain localization process. Notable differences are observed in the response of the specimen under loading depending on the constitutive relation used. The numerical study indicated that the constitutive model controls the flow localization, defines the strain of instability and determines the number of necks formed. The causes which reside behind such decisive role played by the constitutive relation are investigated. It has been found that the rate sensitivity definition governs the models' predictions for the strain localization process.

Key words: annealed OFHC copper, Fragmentation, Ring expansion, Constitutive description, Numerical simulation.

1. Introduction

Plastic instabilities play a prominent role in the deformation and failure of engineering materials subjected to dynamic loading [1–3]. Susceptibility of metals for instabilities formation determines their suitability for absorbing energy under dynamic solicitations. Understanding formation and propagation of instabilities in metals offers significant steps towards optimizing material's behaviour

at high strain-rates [4–9]. Strain localization has gathered the efforts of many researchers [8–9, 10–16]. The seminal works of HUTCHINSON and NEALE [17], GHOSH [18] and FRESSENGEAS and MOLINARI [19–20] among others analysed the mechanisms responsible for plastic localization and instabilities progression.

Among the experimental arrangements applied to approach the localization problem under high loading rates, the ring expansion test has raised the interest of many investigators [21–26]. The main advantage of this test is that disturbances resulting from wave propagation are eliminated due to the symmetry of the problem (*under ideal boundary conditions and complete homogeneity of the material*) [23, 27–28] and the material ductility may be properly evaluated.

The test consists of loading a ring of radius R at a roughly constant velocity V_0 within the range 10 m/s $\leq V_0 \leq$ 300 m/s [25–26]. The dynamic loading uses to be procured by a magnetic field or by the use of explosives. Among the previous testing techniques, the former displays an improved capacity for controlling the applied velocity. In any case, the mean strain rate $\dot{\varepsilon}(t)$ applied to the material during the test is defined by Eq. (1.1).

$$\dot{\varepsilon}(t) = \frac{V_0}{R(t)}, \tag{1.1}$$

where $R(t)$ is the specimen radius as a function of time.

Large strains and strain rates that take place during the expansion of the ring lead to the formation of plastic instabilities inducing posterior fragmentation of the sample, Fig. 1.

Unfortunately, such kind of highly instrumented test is complicated to perform and requires of specific facilities. In order to avoid the complications arising from experimentation, recently the localization problem in expanded rings has attempted to be analytically described in the seminal works of MERCIER and MOLINARI [27] and ZHOU *et al.* [8]. In these publications a perturbation analysis is conducted in order to investigate the mechanisms which reside behind plastic localization. For this kind of analytical studies, due to complications in the mathematical formulation of the problem, the definition of the homogeneous material behaviour uses to be given by a simplified power-type equation [8, 27]. The accurate definition of the material behaviour is subordinated to a fast derivation of the problem solution. If *advanced* constitutive descriptions want to be used for defining the macroscopic behaviour of the material, numerical methods are a suitable alternative [28].

The term *advanced* uses to be tied to the physical-based constitutive models. They account for physical aspects of the material deformation behaviour. Most of them are founded on the theory of thermodynamics and kinetics of slip developed by KOCKS *et al.* [29]. Some examples are those models proposed in [30–36]. They allow for an accurate definition of the material behaviour un-

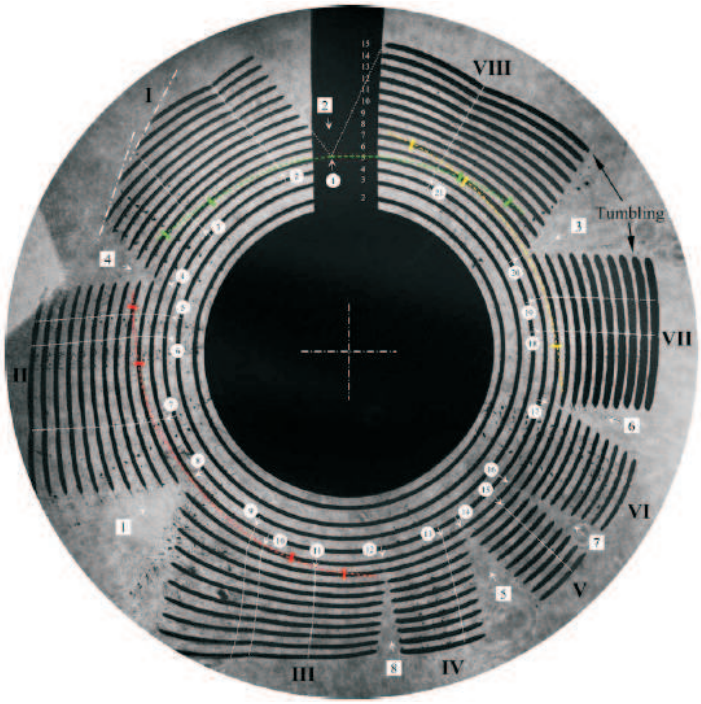

FIG. 1. Composite image for an Al 6061-O ring expanding test. Dimensions of the ring: 15.5 mm mean radius, 0.5 mm thick and 1 mm long. Applied velocity $V_0 \approx 125$ m/s. The frame numbers are identified along the current lead on the top. The necks are identified at the location of their appearance by the numbers inside circles, numbering them counterclockwise. The fracture locations are identified by the numbers inside squares, numbering them in the time sequence of their appearance [25].

der wide a range of loading conditions. Due to their flexibility, physical-based models have an increasing interest for engineering applications like high speed machining, perforation [37], blast loading or crash-tests. In such processes, the material work-piece is subjected to wide ranges of strain rate and temperature as well as large deformation.

In this work the influence of constitutive description in numerical simulations of the radial expansion of annealed **OFHC** copper rings has been studied. For that task, three physical-based constitutive relations with proven efficiency for modelling this material have been implemented into the **FE** code ABAQUS/Explicit and applied in the simulations. These are those due to RUSINEK *et al.* [38], NEMAT–NASSER and LI [31] and VOYIADJIS and ALMASRI [36]. The main reasons that have led us to choose these constitutive descriptions are the rigor of their formulation *(all of them are based on the additive decomposition of the equivalent stress as it will be shown later in this paper)* and the relevance they have raised within the framework of metallic alloys modeling.

The numerical analysis revealed that the process of strain localization occurring in the sample during loading is strongly influenced by the material modelling. A systematic evaluation of the constitutive relations is performed to identify the causes behind this behaviour. It has been found that the rate sensitivity definition determines the models' predictions for instabilities formation.

2. Constitutive modeling of the annealed OFHC copper

Copper is widely used in several industrial fields, typical applications of this metal include electrical and electronic applications, piping for water supplies, heat exchangers, manufacture of semiconductors and superconductor components and manufacture of high vacuum devices such as particle accelerators. Thus, polycrystalline **OFHC** copper is a typical **FCC** metal that has been widely used to explore the dependence of the flow stress on strain, strain rate and temperature [39–40]. Thus, it is clear the aroused interest by the processes of strain localization and fragmentation which occur in this material during dynamic solicitations.

Next, the constitutive descriptions applied for modelling the thermo-viscoplastic behaviour of this material in the simulations are briefly described.

2.1. The Extended Modified Rusinek–Klepaczko model to viscous drag effects

The **E**xtended **M**odified **R**usinek–**K**lepaczko (**EMRK**) [38] constitutive relation is based on the additive decomposition of the equivalent Huber–Mises stress $\overline{\sigma}$ [30, 33, 35, 41–43], Eq. (2.1).

$$\overline{\sigma}(\overline{\varepsilon}^p, \dot{\overline{\varepsilon}}^p, T) = \frac{E(T)}{E_0} \cdot \left[\overline{\sigma}_\mu + \overline{\sigma}^*(\overline{\varepsilon}^p, \dot{\overline{\varepsilon}}^p, T)\right] + \overline{\sigma}_{vs}(\dot{\overline{\varepsilon}}^p), \tag{2.1}$$

where each term of the previous expression, Eq. (2.1), is defined below.

The multiplicative factor $E(T)/E_0$ defines the Young's modulus evolution with temperature [44], Eq. (2.2).

$$E(T) = E_0 \left\{1 - \frac{T}{T_m} \exp\left[\theta^* \left(1 - \frac{T_m}{T}\right)\right]\right\}, \qquad T > 0, \tag{2.2}$$

where E_0, T_m, and θ^* denote respectively the Young's modulus at $T = 0$ K, the melting temperature and the characteristic homologous temperature. This expression allows for defining the material thermal softening depending on the crystal lattice [45]. In the case of **FCC** metals like copper $\theta^* \approx 0.9$ as discussed in [38].

According to the considerations for **FCC** metals reported by several authors [30, 34, 46] the athermal stress $\overline{\sigma}_\mu$ is defined independent of plastic strain. In agreement with [36] this stress component reads as follows, Eq. (2.3).

$$\overline{\sigma}_\mu = Y, \tag{2.3}$$

where Y is the flow stress at $\overline{\varepsilon}^p = 0$.

The thermal stress $\overline{\sigma}^*(\overline{\varepsilon}^p, \dot{\overline{\varepsilon}}^p, T)$ describes macroscopically the rate controlling deformation mechanism from thermal activation. Based on the theory of thermodynamics and kinetics of slip [29], Rusinek *et al.* [38] derived the following expression, Eq. (2.4).

$$\overline{\sigma}^*(\overline{\varepsilon}^p, \dot{\overline{\varepsilon}}^p, T) = B(\dot{\overline{\varepsilon}}^p, T) \cdot (\overline{\varepsilon}^p)^{n(\dot{\overline{\varepsilon}}^p, T)} \cdot \left\langle 1 - \xi_1 \left(\frac{T}{T_m}\right) \log\left(\frac{\dot{\varepsilon}_{\max}}{\dot{\overline{\varepsilon}}^p}\right)\right\rangle^{1/\xi_2}, \tag{2.4}$$

where ξ_1 and ξ_2 are material constants describing temperature and rate sensitivities of the material, T_m is the melting temperature and $\dot{\varepsilon}_{\max}$ defines the maximum rate level for application of the model.

The explicit formulations describing the modulus of plasticity $B(\dot{\overline{\varepsilon}}^p, T)$ and the strain hardening exponent $n(\dot{\overline{\varepsilon}}^p, T)$ are given by Eqs. (2.5)–(2.6).

$$B(\dot{\overline{\varepsilon}}^p, T) = B_0 \left(\left(\frac{T}{T_m}\right) \log\left(\frac{\dot{\varepsilon}_{\max}}{\dot{\overline{\varepsilon}}^p}\right)\right)^{-\nu}; \qquad T > 0, \tag{2.5}$$

$$n(\dot{\overline{\varepsilon}}^p, T) = n_0 \left\langle 1 - D_2 \left(\frac{T}{T_m}\right) \log\left(\frac{\dot{\overline{\varepsilon}}^p}{\dot{\varepsilon}_{\min}}\right)\right\rangle, \tag{2.6}$$

where B_0 is a material constant, ν is tied to the material temperature sensitivity, n_0 is the strain hardening exponent at $T = 0$ K, D_2 is a material constant and $\dot{\varepsilon}_{\min}$ defines the minium rate level for application of the model. The McCauley operator is defined as follows $\langle \bullet \rangle = \bullet$ if $\langle \bullet \rangle \geq 0$ or $\langle \bullet \rangle = 0$ if $\langle \bullet \rangle \leq 0$. It has to be noted that previous expressions are dependent on strain rate and temperature. This feature, which is consistent with experimental evidences reported for most metals [47–48], makes the **EMRK** model appropriate to describe the formation of plastic instabilities in metallic alloys subjected to dynamic solicitations.

The viscous drag component $\overline{\sigma}_{vs}(\dot{\overline{\varepsilon}}^p)$ provides a phenomenological description of the flow stress augment at high strain rates taking place in many metals due to the phonon drag effects in dislocation generation. The formulation used comes from the investigations due to Kapoor and Nemat–Nasser [49]. Based on theoretical considerations and supported by experimental evidences for a certain number of metals they proposed the following relation, Eq. (2.7).

$$\overline{\sigma}_{vs}(\dot{\overline{\varepsilon}}^p) = \chi \cdot \left[1 - \exp(-\alpha \cdot \dot{\overline{\varepsilon}}^p)\right], \tag{2.7}$$

where χ is a material constant, and α represents an effective damping coefficient affecting the dislocations' motion [50–51].

The material constants corresponding to annealed **OFHC** copper are listed in Table 1. They were obtained via a systematic procedure for calibration of the model. This procedure ensures the uniqueness of their values [38].

Table 1. Material constants for annealed OFHC copper for the EMRK model [38].

Y [MPa]	B_0 [MPa]	ν [–]	n_0 [–]	D_2 [–]	ξ_2 [–]	ξ_1 [–]	χ [MPa]	α [s^{-1}]	T_m [K]	$\dot{\varepsilon}_{\min}$ [s^{-1}]	$\dot{\varepsilon}_{\max}$ [s^{-1}]	θ^* [–]
40	560.28	0.30447	0.492	0.0553	0.0131	0.0011932	249	0.0000122	1340	10^{-5}	10^{7}	0.9

Next, the constitutive description proposed by Nemat–Nasser and Li (**NNL**) [31] is introduced.

2.2. The Nemat–Nasser – Li model

In the same manner as the **EMRK** constitutive description, the **NNL** model decomposes the equivalent stress $\overline{\sigma}$ into thermal $\overline{\sigma}^*(\overline{\varepsilon}^p, \dot{\overline{\varepsilon}}^p, T)$ and athermal $\overline{\sigma}_\mu(\overline{\varepsilon}^p)$ components, Eq. (2.8),

$$\overline{\sigma}(\overline{\varepsilon}^p, \dot{\overline{\varepsilon}}^p, T) = \overline{\sigma}_\mu(\overline{\varepsilon}^p) + \overline{\sigma}^*(\overline{\varepsilon}^p, \dot{\overline{\varepsilon}}^p, T). \tag{2.8}$$

The athermal stress term is defined as a function of the equivalent plastic strain, Eq. (2.9).

$$\overline{\sigma}_\mu(\overline{\varepsilon}^p) = \sigma_a^0 \cdot (\overline{\varepsilon}^p)^{n_1}, \tag{2.9}$$

where σ_a^0 and n_1 (*which, on contrary to the* **EMRK** *model, are assumed constant*) are material parameters describing the flow stress level and the strain hardening of the material.

The thermal stress is defined by Eq. (2.10). It depends on plastic strain, strain rate and temperature.

$$\overline{\sigma}^*(\overline{\varepsilon}^p, \dot{\overline{\varepsilon}}^p, T) = \sigma^0 \cdot \left(1 - \left(-\frac{k \cdot T}{G_0} \cdot \left(\ln\left(\frac{\dot{\overline{\varepsilon}}^p}{\dot{\varepsilon}_0}\right) + \ln\left(1 + a(T) \cdot (\overline{\varepsilon}^p)^{n_0}\right)\right)\right)^{1/q}\right)^{1/p} \cdot \left(1 + a(T) \cdot (\overline{\varepsilon}^p)^{n_0}\right), \tag{2.10}$$

where σ^0 is a material constant, k is the Boltzmann's constant, G_o is the reference Gibbs free energy at $T = 0$ K, $\dot{\varepsilon}_0$ is the reference strain rate, n_0 is a material

parameter defining strain hardening (*assumed constant*) and p and q are parameters describing the profile of the short range energy barrier to the motion of dislocations. Moreover, $a(T)$ is an empirical function depending on temperature and tied to the average dislocation spacing *(free path)*, Eq. (2.11).

$$a(T) = a_0 \left(1 - \left(\frac{T}{T_m}\right)^{n_2}\right), \tag{2.11}$$

where a_0 and n_2 are material constants.

The material constants corresponding to annealed **OFHC** copper are listed in Table 2.

Table 2. Material constants for annealed OFHC copper for the NNL model [31].

p [–]	q [–]	k/G_0 [K^{-1}]	$\dot{\varepsilon}_0$ [s^{-1}]	a_0 [–]	σ^0 [MPa]	σ_a^0 [MPa]	n_0 [–]	n_1 [–]	n_2 [–]
2/3	2	0.000049	$2*10^{10}$	20	46	220	0.5	0.3	2

In the following section of the manuscript, the constitutive relation due to Voyiadjis and Almasri (**VA**) [36] is introduced.

2.3. The Voyiadjis–Almasri model

Voyiadjis and Almasri [36] derived a physically-based model founded on the concept of thermal activation analysis. In the same manner as the **EMRK** and **NNL** models, the **VA** splits into two parts the equivalent stress $\overline{\sigma}$. This is the addition of the equivalent thermal stress $\overline{\sigma}^*(\overline{\varepsilon}^p, \dot{\overline{\varepsilon}}^p, T)$ and the equivalent athermal stress $\overline{\sigma}_\mu$, Eq. (2.12),

$$\overline{\sigma}(\overline{\varepsilon}^p, \dot{\overline{\varepsilon}}^p, T) = \overline{\sigma}_\mu + \overline{\sigma}^*(\overline{\varepsilon}^p, \dot{\overline{\varepsilon}}^p, T). \tag{2.12}$$

As the **EMRK** formulation, Eq. (2.1), the **VA** model defines the athermal stress independent of plastic strain, Eq. (2.13).

$$\overline{\sigma}_\mu = Y_a, \tag{2.13}$$

where Y_a is a material constant describing the stress component temperature and rate independent.

The thermal stress is defined as a function of plastic strain Eq. (2.14),

$$\overline{\sigma}^*(\overline{\varepsilon}^p, \dot{\overline{\varepsilon}}^p, T) = (B_0 \cdot \overline{\varepsilon}_p^n) \cdot \left(1 + B_1 \cdot T \cdot (\dot{\overline{\varepsilon}}_p)^{1/m} - B_2 \cdot T \cdot \exp\left(A\left(1 - \frac{T}{T_t}\right)\right)\right). \tag{2.14}$$

In the previous expression B and n denote the strain hardening modulus and the strain hardening exponent respectively (*which, on contrary to the* **EMRK** *model, are assumed constant*). Moreover B_1 and B_2 are material constants tied to mobile dislocation density evolution and to thermodynamic material parameters [36], m defines the strain rate sensitivity and A is a material constant.

The material constants corresponding to annealed **OFHC** copper are listed in Table 3.

Table 3. Material constants for annealed OFHC copper for the VA model [36].

Y_a [MPa]	B_0 [MPa]	n [–]	B_1 [K^{-1}]	B_2 [K^{-1}]	m [–]	A [–]	T_t [K]
0	600	0.42	0.0000004	0.001	1.15	0.001	610

In the case of adiabatic conditions of deformation the constitutive relations previously presented are combined with the energy balance principle, Eq. (2.15). Such relation allows for an approximation of the thermal softening of the material via the adiabatic heating.

$$\Delta T(\overline{\varepsilon}^p, \overline{\sigma}) = \frac{\beta}{\rho C_p} \int_0^{\overline{\varepsilon}^p_{\max}} \overline{\sigma}(\overline{\varepsilon}^p, \dot{\overline{\varepsilon}}^p, T) d\overline{\varepsilon}^p, \tag{2.15}$$

where β is the Taylor-Quinney coefficient assumed as constant, ρ is the material density and C_p is the specific heat at constant pressure. Transition from isothermal to adiabatic conditions of deformation is assumed at $\dot{\varepsilon} = 10\ \mathrm{s}^{-1}$ in agreement with experimental observations reported for metallic materials in [52–53].

Conventional physical constants of annealed **OFHC** copper may be obtained from material handbooks, Table 4.

Table 4. Physical constants for annealed OFHC copper.

E_0 [GPa]	C_p [$\mathrm{Jkg}^{-1}\mathrm{K}^{-1}$]	β [–]	ρ [kgm^{-3}]
130	385	0.9	8960

In the following section of the document the analytical predictions of previous models are compared with experiments [31]. The definition they provide of the thermo-viscoplastic material behaviour is discussed.

3. Application of EMRK, NNL and VA models to annealed OFHC copper

In Fig. 2 is depicted the comparison between analytical predictions of the models and experiments at room temperature for two values of strain rate, $\dot{\varepsilon} = 0.1\ \mathrm{s}^{-1}$ and $\dot{\varepsilon} = 8000\ \mathrm{s}^{-1}$ (*The former strain rate corresponding to isothermal conditions of deformation, the latter to adiabatic*). Satisfactory agreement is observed in, Fig. 2.

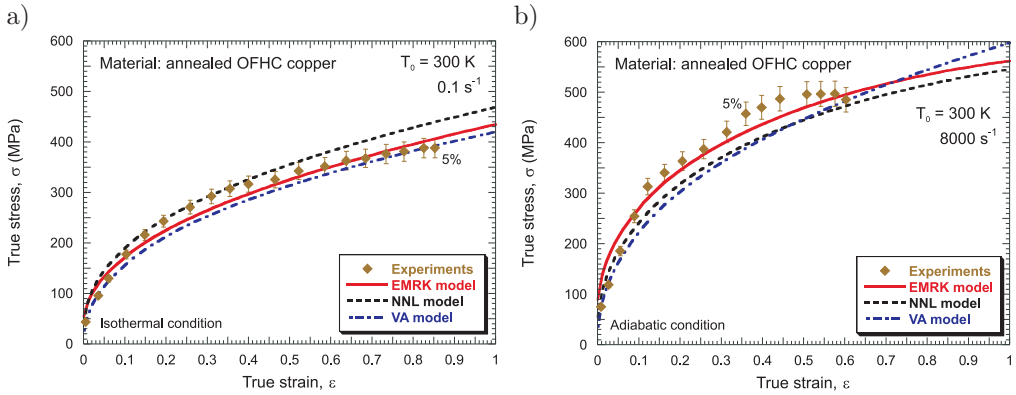

Fig. 2. Description of the flow stress evolution as a function of strain using **EMRK**, **NNL** and **VA** models and comparison with experiments at room temperature: a) 0.1 s^{-1}, b) 8000 s^{-1} [31].

However for strain rate levels between those analyzed in previous graphs, $0.1\ \mathrm{s}^{-1} < \dot{\varepsilon} < 8000\ \mathrm{s}^{-1}$, the **VA** model provides predictions of material flow stress quite lower than those due to the **EMRK** and **NNL** formulations, Fig. 3.

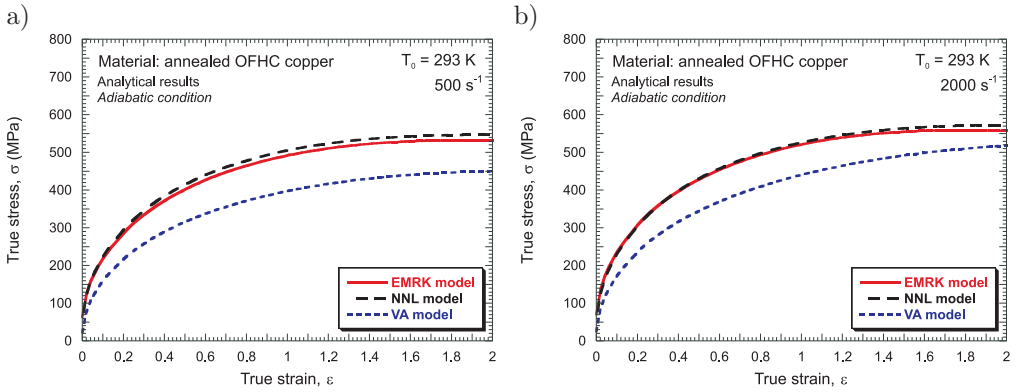

Fig. 3. Description of the flow stress evolution as a function of strain using **EMRK**, **NNL** and **VA** models at room temperature: a) 500 s^{-1}, b) 2000 s^{-1}.

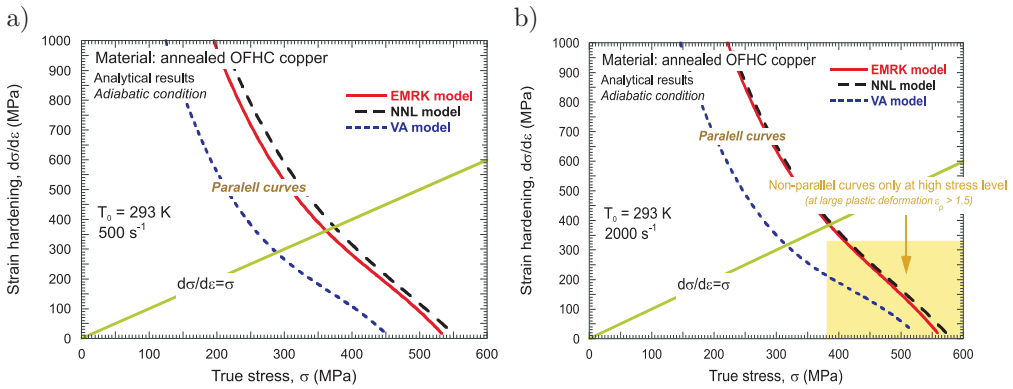

FIG. 4. Description of the strain hardening evolution as a function of stress using **EMRK**, **NNL** and **VA** models at room temperature: a) 500 s^{-1}, b) 2000 s^{-1}.

Nevertheless, it must be highlighted that the strain hardening definition provided by the three models is quite similar for the whole range of strain rates analyzed in this paper, Fig. 4.

The differences in the flow stress level mentioned above come from the rate sensitivity definition predicted by each constitutive relation, Fig. 5. Those differences are especially remarkable within the range of strain rates covered in the numerical simulations conducted in this work, 100 $s^{-1} < \dot{\varepsilon} <$ 10000 s^{-1}, Fig. 5.

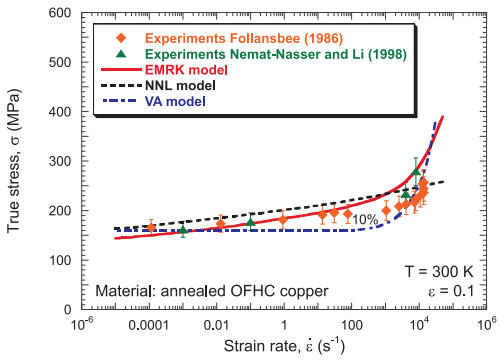

FIG. 5. Description of the flow stress evolution as a function of strain rate using **EMRK**, **NNL** and **VA** models and comparison with experiments at room temperature for $\varepsilon = 0.1$ [31, 54].

In Fig. 6 is illustrated the rate sensitivity predicted by the constitutive relations considered for two values of strain, $\varepsilon = 0.1$ and $\varepsilon = 0.5$. The **NNL** model shows quite reduced rate sensitivity, lower than that provided by the **EMRK** formulation for the whole range of strain rates considered, Fig. 6. It has to be noted that for $\dot{\varepsilon} \leq 10$ s^{-1} the rate sensitivity shown by the **VA** model

is practically nil. Nevertheless, beyond that point the rate sensitivity exhibited by this model sharply increases and it quickly exceeds the **EMRK** and **NNL** predictions, Fig. 6.

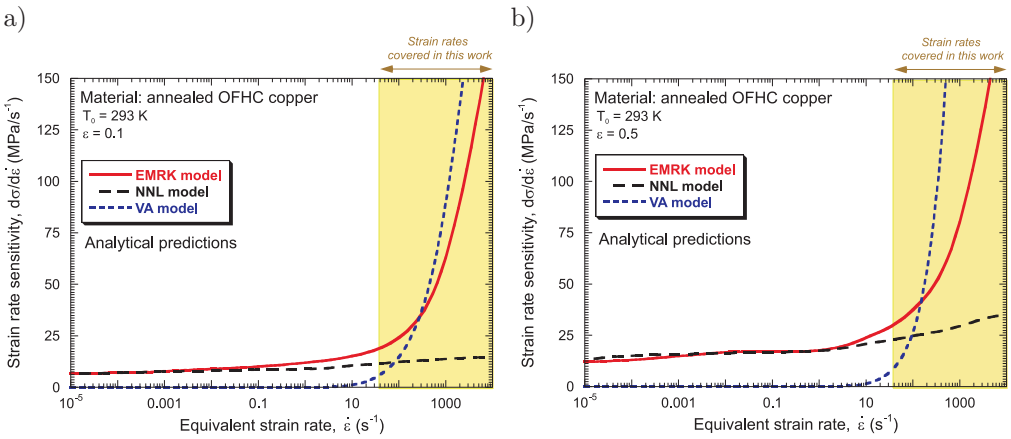

FIG. 6. Rate sensitivity predicted by the three models considered for different values of strain at room temperature: a) $\varepsilon = 0.1$, b) $\varepsilon = 0.5$.

In the following section of the manuscript, the numerical model built for simulation of the ring expansion problem is described.

4. Numerical model and validation

4.1. Numerical model

The geometry and dimensions of the ring are based on a previous work [28], Fig. 7. The inner diameter of the ring is $\phi = 30$ mm, with a thickness of

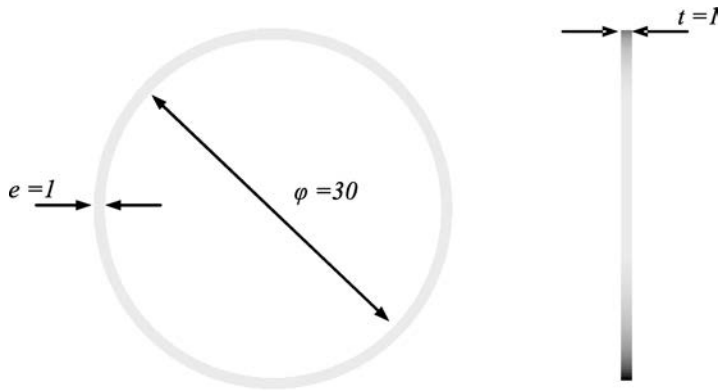

FIG. 7. Geometry and dimensions (mm) of the specimen used in the simulations [28].

$e = 1$ mm and a width of $t = 1$ mm (1 mm^2 *square cross section*). The impact velocity is applied in the inner surface of the ring and remains constant during the whole loading process [28] leading to the strain rate decrease described by Eq. (1.1).

The mesh used is shown in Fig. 8. Three elements are placed along the thickness and width of the sample. The ring has been meshed using hexahedral elements whose aspect ratio is close to 1:1:1 ($\approx 0.33 \times 0.33 \times 0.33$ mm^3). This definition is in agreement with the considerations reported by ZUKAS and SCHEFFLER [55]. No geometrical or material imperfections were introduced in the model [56] since they could perturb the necking process [57–58].

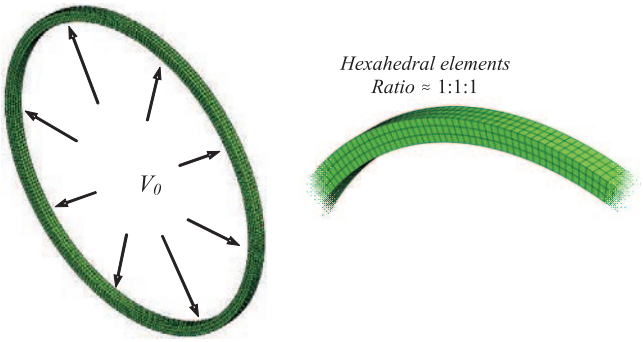

FIG. 8. Mesh configuration used in the numerical simulations. Symmetric mesh without any geometrical imperfection.

The boundary conditions applied to the simulations must guarantee the uniaxial tensile state in the specimen during loading.

It must be noticed that the strain of instability is intrinsically tied to the definition of the homogenous material behaviour (*constitutive description used to define the material behaviour*). Thus, in agreement with RUSINEK and ZAERA [28], a constant critical failure strain, $\overline{\varepsilon}_f^p = 2.5$, has been used in the simulations (*erosive failure criterion involving element deletion*). The condition that must be imposed to the failure strain is to be large enough to not disturb plastic localization and necking development. If such condition is fulfilled, the number of necks is not affected by the failure strain level. The numerical uncertainties through the integration process being enough to perturb the stress and deformation fields [28]. Then, wave reflections and interactions take place leading to strain localization in the absence of geometrical or material irregularities [60].

It has to be highlighted that considering a viscoplastic material model acts as a regularization method for solving mesh-dependent strain softening problems of plasticity [7]. Rate dependent plasticity introduces implicitly a length-scale

parameter into the boundary value problem diffusing the localization region [59]. It guarantees the well-posedness of the problem and the uniqueness of the numerical solution [60].

The three constitutive relations here analyzed have been implemented into ABAQUS/Explicit **FE** code via a **VUMAT** subroutine by means of the thermo-viscoplastic integration scheme for Huber-Misses plasticity proposed by Zaera and Fernández–Sáez [61].

4.2. Validation of the numerical model

Numerical simulations within the range of impact velocities 5 m/s $\leq V_0 \leq$ 150 m/s have been carried out. Stress – strain curves obtained from simulations are compared with analytical predictions of the constitutive relations. In the simulations, the measurement is conducted on an integration point belonging to an element out of the necking zone, Fig. 9. There, the flow stress can be considered homogeneous.

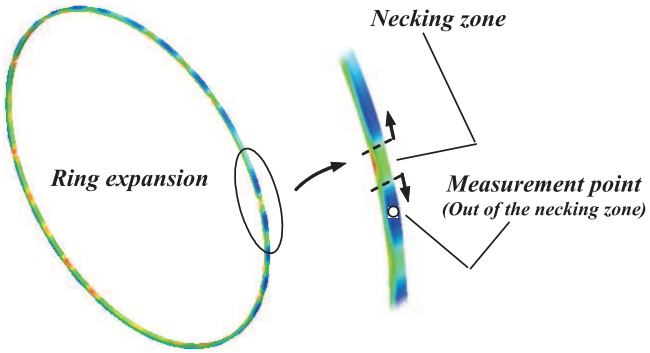

Fig. 9. Measurement point of strain-stress curves for validation of the model.

It has been already mentioned that the strain rate is not constant along the test. However, since the decrease of the strain rate during loading will be quite reduced, let us assume that a satisfactory comparison between analytical predictions and simulations can be conducted. The analytical predictions are obtained using the initial strain rate applied to the test. Perfect matching is observed between analytical predictions and simulation results (*for the* **EMRK** *model the decrease of the strain rate during the test is responsible for the small disagreement taking place at large deformation*), Fig. 10. This validates the numerical model developed and the implementation of the constitutive relations into the **FE** code.

In the following section of the manuscript the results obtained from the numerical simulations are discussed.

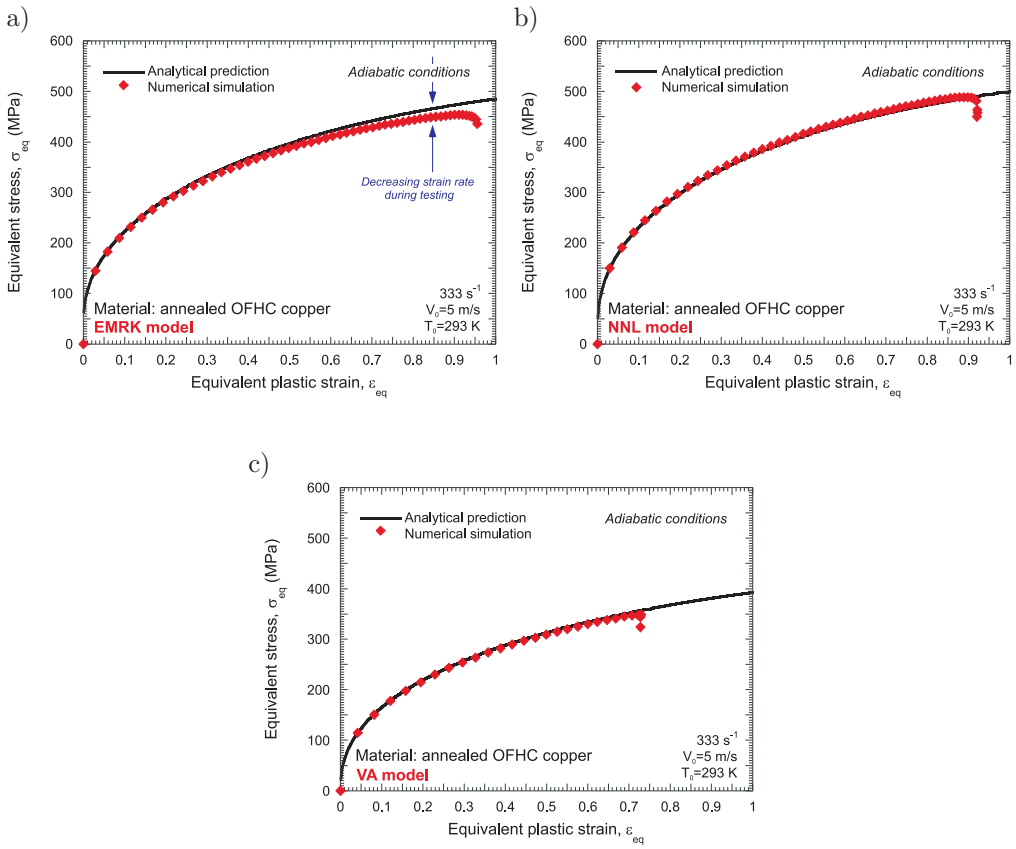

FIG. 10. Comparison between numerical results and analytical predictions for the three models considered at $V_0 = 5$ m/s.

5. Numerical results and discussion

The first step is to analyze the evolution of the local plastic strain (*in the necking*) as a function of the global one (*theoretical deformation corresponding to homogeneous behaviour*) for all the constitutive descriptions and different impact velocities. The measurement of the local plastic strain is conducted as depicted in Fig. 11.

The calculation of the global deformation is carried out via Eq. (5.1).

$$\varepsilon_{\text{global}}(t) = \ln\left(\frac{R(t)}{R_0}\right), \tag{5.1}$$

where R_0 is the initial radius of the sample and $R(t)$ is the specimen radius as a function of time obtained from the simulations.

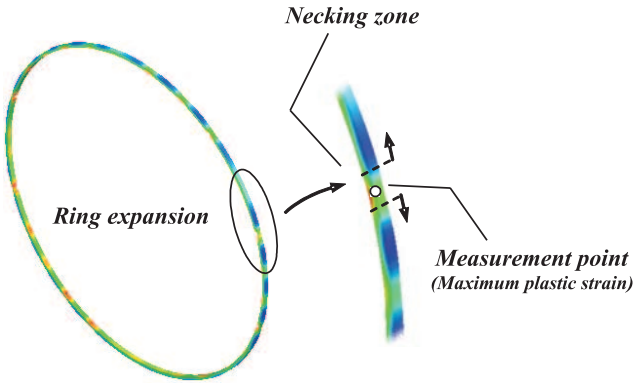

FIG. 11. Measurement point of local plastic strain.

By application of this procedure the following graphs are obtained, Fig. 12. Until necking takes place the local plastic strain agrees with the theoretical one. Once instability is formed, the local plastic strain drastically deviates from the global specimen deformation [62]. The bifurcation point (*strain of instability*) is highly dependent on impact velocity as well as on the constitutive model applied, Fig. 12.

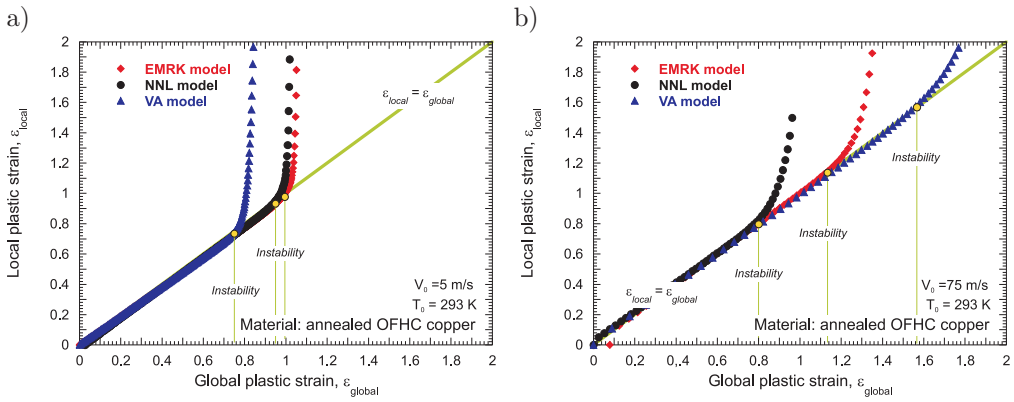

FIG. 12. Local plastic strain as a function of the global plastic strain for the three constitutive descriptions considered: a) $V_0 = 5$ m/s, b) $V_0 = 75$ m/s.

It can be observed that the strain of instability predicted by the **EMRK** model is larger than that predicted by the **NNL** model for both velocities checked, Fig. 12. Moreover, it is interesting to notice that in the case of $V_0 = 5$ m/s the smallest strain of instability corresponds to the **VA** constitutive description, however for $V_0 = 75$ m/s it predicts the largest one, Fig. 12.

Such trends are confirmed analyzing the evolution of the local plastic strain rate in the necking as a function of the global plastic strain, Fig. 13. In such

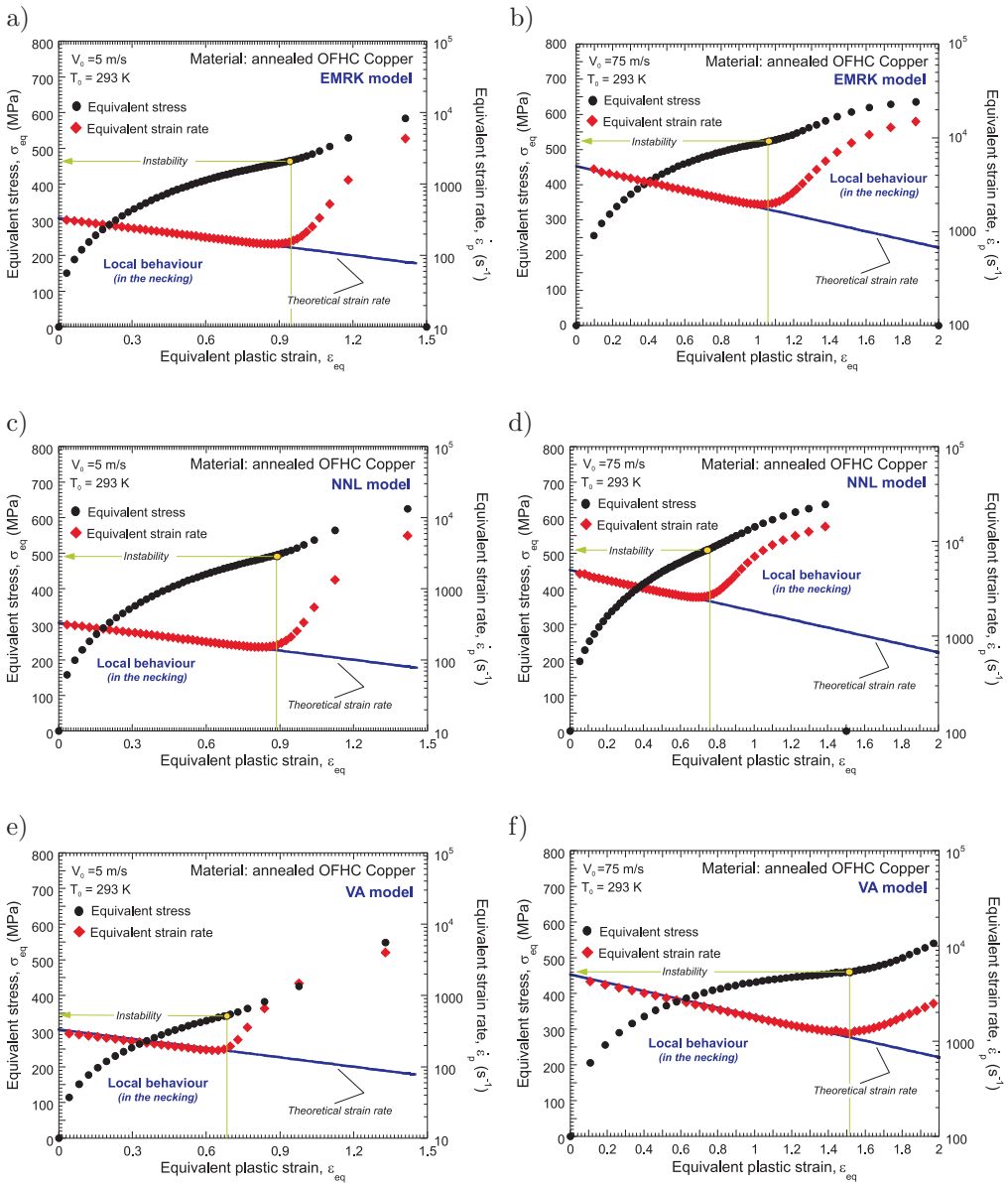

FIG. 13. Local strain rate and local flow stress as a function of the global plastic strain for the three constitutive descriptions considered and two impact velocities: a), c), e) $V_0 = 5$ m/s. b), d), f) $V_0 = 75$ m/s.

a case the strain of instability is determined by the bifurcation point of the local strain rate from the theoretical one, Eq. (1.1), Fig. 13. Necking formation involves a sharp augment of the local strain rate and flow stress.

In order to go further in this investigation let us depict the evolution of the strain of instability and the time of instability as a function of the impact velocity for the three models considered, Fig. 14. For the whole range of impact velocities, the strain of instability predicted by the **EMRK** model is larger than that determined by the **NNL** formulation. The difference between the predictions of both models increases with the impact velocity applied to the ring. Moreover, the **VA** constitutive description shows the lowest strain of instability until $V_0 = 10$ m/s, Fig. 14. Then, it exceeds the predictions of **EMRK** and **NNL** models and the strain of instability shown by the **VA** constitutive relation becomes the largest one. The range of impact velocities $V_0 < 10$ m/s corresponds to initial strain rate of the test $\dot{\varepsilon} \leq 650\ \mathrm{s}^{-1}$ (*the strain rate applied to the material will decrease during loading from this value*). It has to be noted that within that range of strain rates the rate sensitivity predicted by the **VA** model is the lowest one, Fig. 5. The range of impact velocities $V_0 > 10$ m/s corresponds to initial strain rate of the test $\dot{\varepsilon} \geq 650\ \mathrm{s}^{-1}$. It has to be noted that within that range of strain rates the rate sensitivity predicted by the **VA** model becomes the largest one, Fig. 5. It seems to be clear that rate sensitivity and strain of instability are closely related.

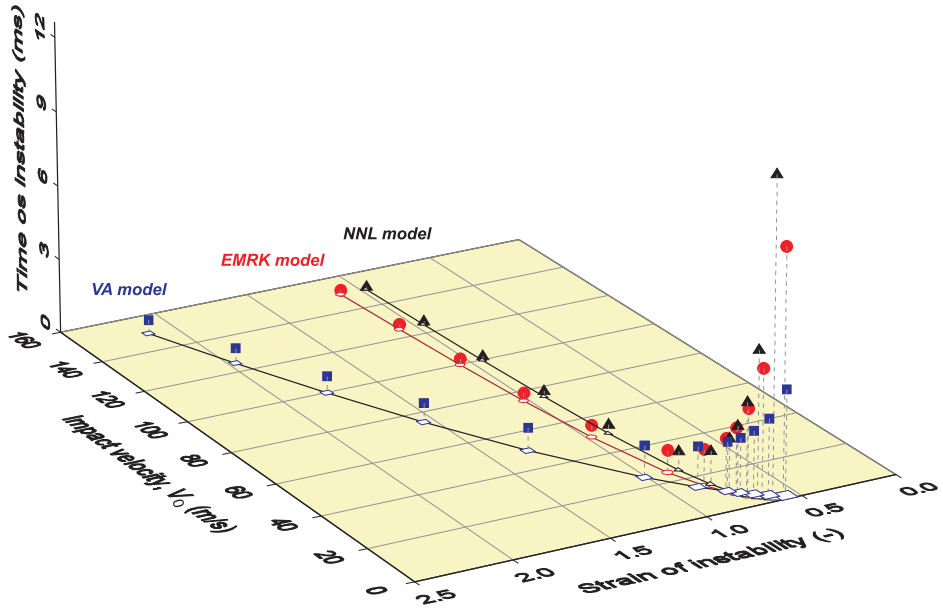

FIG. 14. Strain and time of instability as a function of impact velocity for the three constitutive descriptions considered.

The larger the rate sensitivity, the larger the strain of instability (*It has to be taken into account that the strain hardening predictions of all the models are*

very similar, Fig. 4. Strain hardening is not responsible for the differences in the strain of instability shown in Fig. 14). This consideration explains the increasing strain of instability with impact velocity exhibited by the three constitutive relations, Fig. 14. Since all constitutive models show increasing rate sensitivity with strain rate augment (*within the range of impact velocities considered in this investigation*), the strain of instability is always increasing with impact velocity (*this trend is also enhanced by effect of inertia* [24]). Within the range of impact velocities into which the **VA** model shows the lowest rate sensitivity, it predicts the smallest time of instability. Opposite behaviour is observed within the range of impact velocities into which the **VA** formulation predicts the largest rate sensitivity, Fig. 14.

Moreover, it has been analyzed the number of necks taking place in the sample (*as previously discussed the number of necks is independent of the failure strain applied in the simulations if this is large enough to not disturb the strain localization process*), Fig. 15. Increasing impact velocity leads to increasing number of necks for all the models analyzed [27–28].

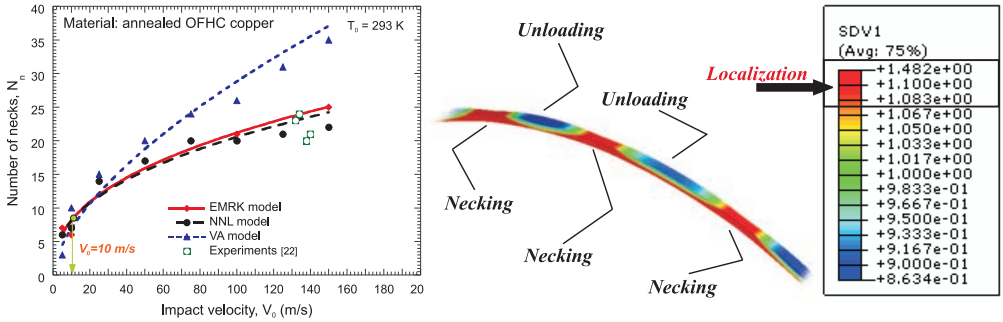

FIG. 15. Number of necks as a function of the impact velocity for the three constitutive descriptions considered and comparison with experiments [22]. Plastic strain contours of the ring during loading for determination of the number of necks.

It has to be highlighted that, within the range of impact velocities 100 m/s$\leq$ $V_0 \leq$ 150 m/s, both **EMRK** and **NNL** constitutive models seem to provide satisfactory predictions of the number of necks in comparison with the experimental data reported by GRADY and BENSON [22], Fig. 15. However, the **VA** model predicts much larger number of necks than those observed in experiments. Such disagreement seems to be caused rate sensitivity definition that the **VA** model shows at high strain rates.

It is concluded that the rate sensitivity acts as a key variable for controlling the strain localization processes taking place in metals subjected to dynamic loading. If a constitutive description is applied for predicting the thermo-viscoplastic response of a metallic alloy subjected to impact loading, it has

to provide a precise description of the material rate sensitivity. Otherwise the confidence on the results obtained from such analysis should be questioned. Accuracy in constitutive modelling of metals is a key point in numerical analyses of dynamic processes.

6. Concluding and remarks

This work presents a numerical analysis on the role played by the constitutive description on the strain localization process in the radial expansion of copper rings. For that task, three physical-based constitutive relations have been implemented into the **FE** code ABAQUS/Explicit and applied in the simulations. These are the **E**xtended **M**odified **R**usinek–**K**lepaczko, the **N**emat–**N**asser–**L**i and the **V**oyiadjis–**A**lmasri constitutive descriptions. Numerical simulations within the range of impact velocities 5 m/s $\leq V_0 \leq$ 150 m/s have been carried out. The analysis revealed that the process of strain localization occurring in the sample during loading is strongly influenced by the material modelling. It has been found that the rate sensitivity definition determines the model predictions for instabilities formation. The application of numerical methods for solving dynamic initial-boundary value problems requires of constitutive descriptions providing a very accurate description of the material rate sensitivity within wide ranges of loading conditions.

Acknowledgment

The researchers of the University Carlos III of Madrid are indebted to the Comunidad Autónoma de Madrid (Project CCG08-UC3M/MAT-4464) and to the Ministerio de Ciencia e Innovación de España (Project DPI/2008-06408) for the financial support received which allowed conducting part of this work.

References

1. R. P. Papirno, J. F. Mescall, A. M. Hansen, *Beyond the taylor test to fracture*, [in:] *Designing for extremes: Environment, loading, and structural behavior*, Proceedings of the Army Symposium on Solid Mechanics, pp. 367–385, Watertown, MA, September 1980. Army Materials and Mechanics Research Center.

2. H. Couque, *On the use of the symmetric Taylor test to evaluate dynamic ductile compression fracture properties of metals*, Proceedings of the 5th International Conference on Structures Under Shock and Impact, pp. 579–589, Computational Mechanics Inc, Billerica, MA, USA, 1998.

3. A. Molinari, C. Musquar, G. Sutter, *Adiabatic shear banding in high speed machining of Ti–6Al–4V: Experiments and modeling*, Int. J. Plasticity, **18**, 443–459, 2002.

4. M. K. Duszek, P. Perzyna, *The localization of plastic deformation in thermoplastic solids*, Int. J. Solids and Struct., **27**, 1419–1443, 1991.

5. T. Łodygowski, M. Lengnick, P. Perzyna, E. Stein, *Viscoplastic numerical analysis of dynamic plastic strain localization for a ductile material*, Arch. Mech., 46, 4, 541–557, 1994.

6. P. Perzyna, *Instability phenomena and adiabatic shear band localization in thermoplastic flow processes*, Acta Mechanica, **106**, 173–205, 1994.

7. A. Glema, T. Łodygowski, P. Perzyna, *Interaction of deformation waves and localization phenomena in inelastic solids*, Comput. Methods Appl. Mech. Engrg., **183**, 123–140, 2000.

8. F. Zhou, J. F. Molinari, K. T. Ramesh, *An elasto-visco-plastic analysis of ductile expanding ring*, Int. J. Impact Eng., **33**, 880–891, 2006.

9. D. Rittel, G. Ravichandran, A. Venkert, *The mechanical response of pure iron at high strain rates under dominant shear*, Mat. Sci. Eng. A., **1–2**, 191–201, 2006.

10. H. C. Mann, *High-velocity tension-impact tests*, Proc. ASTM, **36**, 85, 1936.

11. J. R. Klepaczko, *Generalized conditions for stability in tension test*, Int. J. Mech. Sci., **10**, 297–313, 1968.

12. A. M. Rajendran, I. M. Fyfe, *Inertia effects on the ductile failure of thin rings*, Journal of Applied Mechanics, Transactions of the ASME, **49**, 31-36, 1982.

13. R. J. Clifton, J. Duffy, K. A. Hartley, T. G. Shawki, *On the critical conditions for shear band formation at high strain rates*, Scripta Metall., **5**, 443–448, 1984;.

14. R. C. Batra, C. H. Kim, *Effect of viscoplastic flow rules on the initiation and growth of shear bands at high strain rate*, J. Mech. Phys. Solids, **6**, 859–874, 1990.

15. J. R. Klepaczko, *Remarks on impact shearing*, J. Mech. Phys. Solids, **35**, 1028–1042, 1998.

16. Z. Xue, A. Vaziri, J.W. Hutchinson, *Material aspects of dynamic neck retardation*, J. Mech. Phys. Solids, 56, 93–113, 2008.

17. J. W. Hutchinson, K. W. Neale, *Influence of strain rate sensitivity on necking under uniaxial tension*, Acta Metall., **25**, 839–846, 1977.

18. A. K. Ghosh, *Tensile instability and necking in materials with strain hardening and strain-rate hardening*, Acta Metall., **25**, 1413–1424, 1977.

19. C. Fressengeas, A. Molinari, *Instability and localization of plastic flow in shear at high strain rates*, J. Mech. Phys, Solids, **2**, 185–211, 1987;.

20. C. Fressengeas, A. Molinari, *The time development of Eulerian/Lagrangian perturbations to simple shear and its applications to shear banding*, J. Mech. Phys. Solids, **8**, 1735–1756, 1992.

21. F. L. Niordson, *A unit for testing materials at high strain rates*, Exp. Mech., **5**, 29–32, 1965.

22. D. E. Grady, D. A. Benson, *Fragmentation of metal rings by electromagnetic loading*, Exp. Mech., **12**, 393–400, 1983.

23. X. Hu, G. S. Daehn, *Effect of velocity on flow localization in tension*, Acta Mater., **44**, 1021–1033, 1996.

24. M. Altynova, X. Hu, G. S. Daehn, *Increased ductility in high velocity electromagnetic ring expansion*, Metall. Trans. A, **27**, 1837–1844, 1996.

25. H. Zhang, K. Ravi–Chandar, *On the dynamics of necking and fragmentation – I. Real-time and post-mortem observations in Al 6061-O*, Int. J. Fract., **142**, 183–217, 2006.

26. H. Zhang, K. Ravi–Chandar, *On the dynamics of necking and fragmentation – II. Effect of material properties, geometrical constraints and absolute size*, Int. J. Fract., **150**, 3–36, 2008.

27. S. Mercier, A. Molinari, *Analysis of multiple necking in rings under rapid radial expansion*, Int. J. Impact. Eng., **4**, 403–419, 2004.

28. A. Rusinek, R. Zaera, *Finite element simulation of steel ring fragmentation under radial expansion*, Int. J. Impact. Eng., **34**, 799–822, 2007.

29. U. F. Kocks, A. S. Argon, M. F. Ashby, *Thermodynamics and kinetics of slip*, [in:] Progress in Materials Science, vol. 19, Chalmers B., Christian J.W., Massalski T.B. [Eds.], Pergamon Press, Oxford, 1975.

30. F. J. Zerilli, R. W. Armstrong, *Dislocation-mechanics-based constitutive relations for material dynamics calculations*, J. Appl. Phys., **61**, 1816–1825, 1987.

31. S. Nemat–Nasser, Y. Li, *Flow stress of FCC polycrystals with application to OFHC Copper*, Acta Mater., **46**, 565–577, 1998.

32. A. Rusinek, J. R. Klepaczko, *Shear testing of sheet steel at wide range of strain rates and a constitutive relation with strain-rate and temperature dependence of the flow stress*, Int. J. Plasticity, **17**, 87–115, 2001.

33. S. Nemat–Nasser, W. G. Guo, *Thermomechanical response of DH-36 structural steel over a wide range of strain rates and temperatures*, Mech. Mat., **35**, 1023–1047, 2003.

34. G. Z. Voyiadjis, F. H. Abed, *Microstructural based models for bcc and fcc metals with temperature and strain rate dependency*, Mechanics of Materials, **37**, 355–378, 2005.

35. F. H. Abed, G. Z. Voyiadjis, *Plastic deformation modeling of AL-6XN stainless steel at low and high strain rates and temperatures using a combination of bcc and fcc mechanisms of metals*, Int. J. Plasticity, **21**, 1618–1639, 2005.

36. G. Z. Voyiadjis, A. H. Almasri, *A physically based constitutive model for fcc metals with applications to dynamic hardness*, Mech. Mater., **40**, 549–563, 2008.

37. A. Rusinek, J. A. Rodríguez–Martínez, R. Zaera, J. R. Klepaczko, A. Arias, C. Sauvelet, *Experimental and numerical analysis of failure process of mild steel sheets subjected to perpendicular impact by hemispherical projectiles*, Int. J. Impact. Eng., **36**, 565–587, 2009.

38. A. Rusinek, J. A. Rodríguez–Martínez, A. Arias, *A thermo-viscoplastic constitutive model for FCC metals with application to OFHC copper*, Int. J. Mech. Sci., **52**, 120–135, 2010.

39. M. C. Cai, L. S. Niu, X. F. Ma, H. J. Shi, *A constitutive description of the strain rate and temperature effects on the mechanical behavior of materials*, Mech. Mat., **42**, 774–781, 2010.

40. C. Y. Gao, L. C. Zhang, *A constitutive model for dynamic plasticity of FCC metals*, Materials Science and Engineering A., **527**, 3138–3143, 2010.

41. A. Seeger, *The mechanism of glide and work-hardening in face centered cubic and hexagonal close-packed metal*, [in:] *Dislocations and Mechanical Properties of Crystals*, J. Wiley, New York, 1957.

42. U. F. Kocks, *Realistic constitutive relations for metal plasticity*, Mat. Sci. and Eng. A., **317**, 181–187, 2001.

43. J. A. Rodríguez–Martínez, A. Rusinek, J. R. Klepaczko, *Constitutive relation for steels approximating quasi-static and intermediate strain rates at large deformations*, Mech. Res. Com., **4**, 419–427, 2009.

44. J. R. Klepaczko, *A general approach to rate sensitivity and constitutive modeling of FCC and BCC metals*, [in:] *Impact: Effects of Fast Transient Loadings*, Rotterdam, 3–35, 1998.

45. A. Rusinek, J. A. Rodríguez–Martínez, J. R. Klepaczko, R. B. Pecherski, *Analysis of thermo-visco-plastic behaviour of six high strength steels*, J. Mater. Des., **30**, 1748–1761, 2009.

46. P. S. Follansbee, U. F. Kocks, *A constitutive description of the deformation of copper based on the use of the mechanical threshold stress as an internal state variable*, Acta Metall., **1**, 81–93, 1988.

47. J. R. Klepaczko, *Thermally activated flow and strain rate history effects for some polycristalline f.c.c. metals*, Materials Science and Engineering, **18**, 121–135, 1975.

48. J. R. Klepaczko, B. Rezaig, *A numerical study of adiabatic shear banding in mild steel by dislocation mechanics based constitutive relations*, Mechanics of Materials, **24**, 125–139, 1996.

49. R. Kapoor, S. Nemat–Nasser, *Comparison between high strain-rate and low strain-rate deformation of tantalum*, Metall. Mater. Trans., **31A**, 815–823, 1999.

50. S. Nemat–Nasser, W. G. Guo, D. P. Kihl, *Thermomechanical response of AL-6XN stainless steel over a wide range of strain rates and temperatures*, J. Mech. Phys. Solids, **49**, 1823–1846, 2001.

51. A. Rusinek, J. A. Rodriguez–Martinez, R. Pesci, J. Capelle, *Experimental characterisation and modelling of thr thermo-viscoplastic behaviour of steel AISI 304 within wide ranges of strain rate at room temperature*, Journal of Theoretical and Applied Mechanics, 2010 [in press].

52. O. Oussouaddi, J. R. Klepaczko, *An analysis of transition from isothermal to adiabatic deformation in the case of a tube under torsion* [in French], Proceedings Conf. DYMAT 91, Journal de Physique IV 1991, Coll. C3 (Suppl. III), C3–323.

53. A. Rusinek, R. Zaera, J. R. Klepaczko, *Constitutive relations in 3-D for a wide range of strain rates and temperatures – application to mild steels*, Int. J. Solids Struct., **44**, 5611–5634, 2007.

54. P. S. Follansbee, *High-strain-rate deformation of FCC metals and alloys*, [in:] *Metallurgical applications of shock-wave and high-strain-rate phenomena*, pp. 451–479, 1986.

55. J. A. Zukas, D. R. Scheffler, *Practical aspects of numerical simulations of dynamic events: effects of meshing*, Int. J. Impact Eng., 925–945, 2000.

56. M. Larson, A. Needlemen, V. Tvergaard, B. Storakers, *Instability and failure of internally pressurized ductile metal cylinders*, Internal report, Division of Engineering, Brown University, Providence, June 1981.

57. J. B. Han, V. Tvergaard, *Effect of inertia on the necking behaviour of ring specimens under rapid axial expansion*, Eur. J. Mech. A/Solids, **14**, 287–307, 1995.

58. N. J. Sorensen, L. B. Freund, *Unstable neck formation in a ductile ring subjected to impulsive radial loading*, Int. J. Solids Struct., **37**, 2265–83, 2000.

59. G. Z. Voyiadjis, F. H. Abed, *A coupled temperature and strain rate dependent yield function for dynamic deformations of bcc metals*, International Journal of Plasticity, **22**, 1398–1431, 2006.

60. J. A. Nemes, J. Eftis, *Constitutive modelling on the dynamic fracture of smooth tensile bars*, International Journal of Plasticity, **9**, 243–270, 1993.

61. R. Zaera, J. Fernández–Sáez, *An implicit consistent algorithm for the integration of thermoviscoplastic constitutive equations in adiabatic conditions and finite deformations*, Int. J. Solids Struct., **43**, 1594–1612, 2006.

62. N. Triantafyllidis, J. R. Waldenmyer, *Onset of necking in electro-magnetically formed rings*, J. Mech. Phys. Solids, **52**, 2127–2148, 2004.

Received May 11, 2011.

ENGINEERING TRANSACTIONS • *Engng. Trans.* • **59**, 3, 235–248, 2011
Polish Academy of Sciences • Institute of Fundamental Technological Research (IPPT PAN)
National Engineering School of Metz (ENIM)

DYNAMIC COMPRESSION TESTS – CURRENT ACHIEVEMENTS AND FUTURE DEVELOPMENT

W. Moćko [1)], Z.L. Kowalewski [1,2)]

[1)] **Institute of Fundamental Technological Research**
Polish Academy of Sciences
Pawińskiego 5B, 02-106 Warszawa, Poland
e-mail: wmocko@ippt.gov.pl

[2)] **Motor Transport Institute**
Jagiellońska 80, 03-301 Warszawa, Poland

In this paper a modified arrangement of the DICT technique was introduced. Miniaturization of bar and use of shadow principle to make a measurement of displacement allow to obtain strain rate up to 2.2×10^5 s^{-1}. Commonly used methods of elimination of friction, inertia and adiabatic heating were presented. In order to estimate the rate sensitivity of a material (tantalum), quasi-static and SPHB tests were performed at room temperature within the rate spectrum ranging from 5×10^{-4} s^{-1} to 10^3 s^{-1}. The final true stress versus true strain curves at different strain rates were corrected to a constant temperature and zero friction.

Key words: direct impact compression tests, tantalum, Hopkinson bars, miniaturized arrangement.

1. Introduction

It is known for a long time that most materials are dependent on the rate of deformation and temperature. At strain rates above $\sim 10^3$ s^{-1} the strain rate sensitivity for most metals and alloys substantially increases and an accurate and complete picture is necessary in formulation of constitutive relations in the range of the strain rate spectrum up to $\sim 10^6$ s^{-1}.

Although advances in electronics and recordings of short time processes have caused that compression impact experiments are much easier to perform at present, still some improvements in both mechanical designs and measuring techniques are possible. One possibility, which is more recently observed, is miniaturization of experimental setups. The miniaturization enables not only for a substantial increase of strain rate but also for reduction of the radial and longitudinal inertia of specimen. The miniaturization concept has been employed in this study in order to reach strain rates up to $\sim 10^5$ s^{-1}.

One of the most popular experimental techniques applied in determination of viscoplastic properties of materials at strain rates from $\sim 5 \times 10^2$ s^{-1} to $\sim 10^4$ s^{-1} is the Kolsky apparatus [1] or the so-called Split Hopkinson Pressure Bar (SHPB). A modified version of the Kolsky apparatus, the version that is used in most laboratories up to now, has been developed by LINDHOLM [2]. In both versions, a wafer specimen is placed between bars. Such an experimental technique can be applied in many configurations, for example in compression [3, 4], tension [5, 6], torsion [7, 8] and in shear [9, 10], and also in different sizes. In the case of compression test, the wafer specimens are prone to friction and inertia. Moreover, the use of the SHPB technique is limited by the elastic limit of the incident bar. According to the one-dimensional elastic wave propagation theory the "safe" maximum impact velocity is directly related to the elastic limit of the incident bar [1]. Such a condition limits the maximum strain rate in the test.

In order to reach strain rates higher than $\sim 10^4$ s^{-1}, DHARAN and HAUSER [11] introduced modification of the SHPB concept by elimination of the incident bar. Thus, application of the direct impact of a striker onto wafer specimen supported by the transmitter bar enabled to reach strain rates $\sim 10^5$ s^{-1}. Such a modification can be defined as the Direct Impact Compression Test (DICT). It is clear that elimination of the incident bar and reduction of the specimen size leads to a substantial increase of the maximum nominal strain rate in DICT experimental technique. The maximum strain rate $\sim 10^5$ s^{-1} attained by further miniaturization of the DICT up to 1.5 mm transmitter bar diameter was also reported in literature [12].

Of course, specimen reduction can be applied for both SHPB and DICT arrangements. A specimen reduction must be performed proportionally to the length-to-diameter ratio l_{S0}/d_{S0}, usually ~ 0.5 because of optimization of friction and inertia effects [3, 13, 14]. As a consequence of the specimen reduction the whole arrangement, that is SHPB or DICT, must be also reduced. Several attempts to reduce the SHPB size, that is the striker and both bars, were reported in the past [12, 15, 16]. Another miniaturization of SHPB has been reported in 1992 by SAFFORD [17]. The wave dispersion was taken into account. In general, for elastic bars of small dimensions the wave dispersion is a second order effect. A new design and some problems associated with miniaturization were published more recently [18]. Those examples indicate that miniaturization of the conventional SHPB arrangement enables to reach the maximum strain rate $\sim 4.5 \times 10^4$ s^{-1}.

In both cases, namely the conventional and miniaturized DICT arrangements, the technical problem arises how to determine the displacement of the interface striker-specimen as a function of time. This technical problem has been solved in several ways:

- assuming that the striker is perfectly rigid [11],
- applying of a high-speed camera incorporating an optical system with the image-splitting refraction element and lens [16, 19],
- using a two-channel non-contact displacement gage [20, 21],
- following radial displacement of the specimen shadow [22], the so-called LORD (Laser Occlusive Radius Detector).

2. Miniaturized DICT arrangement

A new miniaturized DICT is shown schematically in Fig. 1 [23, 24]. Modification in the mechanical part, similar as reported earlier [25], lies in an introduction of the decelerator tube *5* in to which a small Hopkinson bar *3* with miniature SR gages *4* is inserted. The decelerator tube is mounted in supports *7* slightly ahead of the a Hopkinson bar *3* with a possibility to change the distance between them. Such configuration permits programming of different plastic deformations of specimens. The tube and the bar are both attached to the bumper *8*. The tube can be exactly adjusted to the axis of striker *2* by special support *6*, which also prevents vibrations. In Fig. 2 are shown the main details of the miniaturized DICT. The striker (No. *2* in Fig. 1) of diameter slightly lower than that of the decelerator tube (No. *5* in Fig. 1) triggers deformation of a small cylindrical specimen until it stops by the decelerator tube. The transmitted elastic wave is detected by the SR gage (No. *4* in Fig. 1). The net displacement between the striker and the decelerator tube is measured by the shadow technique. Strikers of diameter 11 mm and of different lengths from 12.5 mm to 50 mm can be launched by an air-gun up to 100 m/s. Specimens of diameter 2.0 mm and lengths from 1.0 mm to 0.8 mm were supported by the transmitter bar of

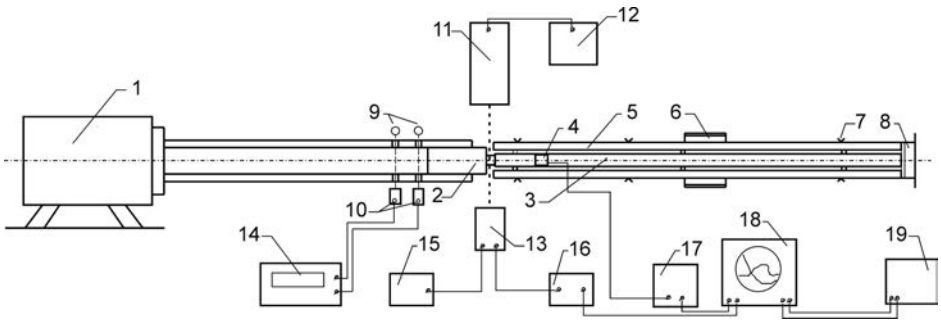

Fig. 1. General scheme of DICT, *1* – air gun; *2* – striker; *3* – transmitter bar; *4* – SR gage; *5* – decelerator tube; *6* – main support; *7* – supports; *8* – dumper; *9* – light sources; *10* – photodiodes; *11* – laser diode; *12* – supply of *11*; *13* – photodiode (displacement measurement); *14* – time counter; *15* – supply unit of *13*; *16* – DC amplifier; *17* – SR amplifier; *18* – digital oscilloscope; *19* – PC.

diameter 5.2 mm and length 243 mm. The transmitter bar was made of the maraging steel with the yield stress of 2.1 GPa. The relative distance between the tube and the transmitter bar could be varied from 0 up to 2.0 mm. This distance defines the maximum deformation of the specimen. In addition, in the application of the combination tube – the bar enables to recover specimens after testing, thus giving an opportunity to observe some microstructural effects. The arrangement permits also for tests with a negative jump in strain rate [25, 26].

The scheme of measurements is shown schematically in Fig. 1. Three independent circuits permit for precise measurement of the impact velocity V_0, the net displacement during specimen deformation $\Delta U(t) = \Delta l_S(t)$, and the transmitted elastic wave $\varepsilon_T(t)$, where t is time.

The striker is accelerated in the launcher tube *1* of length 840 mm up to preprogrammed impact velocity after pressure calibration, that is $V_0(p)$. The mean impact velocity V_0 is determined by two channels consisting of two laser diodes *9*, two diaphragms of diameter 0.5 mm and two photodiodes *10*. The axes of the laser diodes and photodiodes perpendicular to the direction of the launcher tube are situated at 140 mm and 60 mm from the specimen, respectively. Thus, the distance over which the impact velocity is measured is 80 mm. Signals from the photodiodes are recorded by the time counter.

The net displacement, and thus the net mean velocity V_{AV} of specimen deformation, is measured by the principle of shadow, Fig. 1 and Fig. 2, and the wave mechanics in the Hopkinson bar. The light emitted by laser diode *11* is formed by a diaphragm and goes through the gap in between the moving striker and the stationary deceleration tube. During the test the gap is closing up when the specimen is deformed. The displacement of the interface striker/specimen is proportional to the light passed by the gap. The transmitted light is detected by photodiode *13*, the photodiode is supplied by the unit *15*. The electric signal from the photodiode after amplification in *16* is recorded by two-channel digital oscilloscope *18*. It is clear that after calibration the photodiode voltage can be transformed into the displacement of the interface striker/specimen versus time.

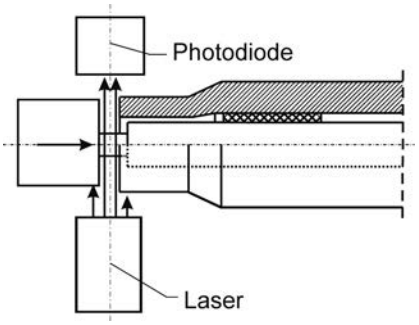

FIG. 2. Zoom of the specimen arrangement.

The displacement of the specimen/transmitter bar can be determined via recording of the signal from the two SR gages of length 0.6 mm cemented on the opposite sides of the transmitter bar. The signals from the SR gages are recorded by the second channel of digital oscilloscope *18* next, the records of both channels are transmitted into PC, No. *19* in Fig. 1.

The definition of the nominal strain rate is given by:

$$\dot{\varepsilon}_n(t) = \frac{1}{l_{S0}} \left[\frac{dU_A(t)}{dt} - \frac{dU_B(t)}{dt} \right]. \tag{2.1}$$

Introducing into Eq. (2.1) the quantities recorded by the DICT measurement system leads to:

$$\dot{\varepsilon}_n(t) = \frac{1}{l_{S0}} \left[\frac{dU_A(t)}{dt} - C_0 \varepsilon_T(t) \right], \tag{2.2}$$

where $U_A(t)$ – displacement of the striker/specimen interface, C_0 – elastic wave speed in transmitter bar, $\varepsilon_T(t)$ – transmitted elastic wave.

The nominal strain $\varepsilon_n(t)$ can be found by integration of Eq. (2.2), thus

$$\varepsilon_n(t) = \frac{1}{l_{S0}} \left[U_A(t) - C_0 \int \varepsilon_T(t)\, dt \right], \qquad 0 < t < T. \tag{2.3}$$

If strikers are assumed being rigid during the whole process of specimen deformation, and their kinetic energies are sufficiently high, then deceleration of a striker is zero. The rigid striker was assumed by Dharan and Hauser [11] in the first version of the DICT. However, in a more exact analysis it may be assumed that deceleration of the interface A is proportional to time, then $a_A = -Bt$, where B is a constant determined from the test via $U_A(t)$ record. This procedure assures flexibility and eliminates difficulties in finding $V_A(t)$ by the time derivative of $U_A(t)$. If $B = 0$, then the deceleration is constant. In general case the velocity $V_A(t)$ is given by

$$V_A(t) = V_0 - B \int_0^t \xi d\xi \qquad \text{and} \qquad V_A(t) = V_0 - \frac{1}{2} B t^2, \qquad 0 < t < T. \tag{2.4}$$

From Eqs. (2.1) and (2.2) one obtains the nominal quantities $\dot{\varepsilon}_n(t)$ and $\varepsilon_n(t)$. The parameters in Eq. (2.4): V_0, B and T must be determined from experiment. Approximation of Eq. (2.4) leads to the following formulas:

$$\dot{\varepsilon}_n(t) = \frac{1}{l_{S0}} \left[V_0 - \left[B \int_0^t \xi d\xi + C_0 \varepsilon_T(t) \right] \right]. \tag{2.5}$$

After integration, the nominal strain is given by:

$$\varepsilon_n(t) = \frac{1}{l_{S0}} \left[V_0 t - \left[\frac{B}{2} t^2 + C_0 \int_0^t \varepsilon_T(\xi) d\xi \right] \right]. \tag{2.6}$$

Of course, the true strain $\varepsilon(t)$ can be obtained from the standard formula $\varepsilon(t) = ln(1 - \varepsilon_n(t))$.

The nominal stress, $\sigma_n(t) \approx F_B(t)/A_{S0}$, in the specimen can be obtained as a function of time assuming that the force equilibrium occurs during the entire process of specimen deformation. This assumption, which is a good approximation for very short specimens, should be in general confirmed every time, for example by a FE analysis. In the present case the specimen is very short, $l_{S0} = 0.8$ mm, and the transit time of the elastic wave through the specimen is $\Delta t_S = 160$ ns. It is well recognized that after 3 to 5 transits the force equilibrium is satisfied [27]. In the present case, $3\Delta t_S = 480$ ns and this period of time is much shorter than the total time of deformation $T = 20$ μs at strain rate 2×10^4 s^{-1}. In real tests the total time of deformation is still longer. The force F_B in the transmitter bar is determined after introduction of Hooke's law:

$$F_B(t) = A_b \rho C_0^2 \varepsilon_T(t), \tag{2.7}$$

where A_b is the cross-section area of the transmitter bar. Thus, the average nominal stress σ_n is given by:

$$\sigma_n(t) = \rho_S C_0^2 \left(\frac{d_H}{d_{S0}} \right)^2 \varepsilon_T(t), \tag{2.8}$$

where d_{S0} and d_H are respectively the initial diameter of specimen and diameter of the transmitter bar, $d_H > d_{S0}$, ρ_S is the density of the specimen material. Because all constitutive relations are defined in true values, that is true stress, true strain and true strain rate, it is important to transform the nominal values into the true quantities like $\sigma(t)$, $\varepsilon(t)$ and $\dot{\varepsilon}(t)$. After elimination of time, the final material characterization can be found: $\sigma(\varepsilon)$ and $\dot{\varepsilon}(\varepsilon)$.

3. Elimination of friction, inertia and adiabatic heating

It is well known that friction occurring on the specimen interfaces with platens during quasi-static compression test increases the mean axial pressure [13, 14, 27, 28]. By integration of the equation of force equilibrium several authors estimated in the past the effect of friction at different levels of approximation. For example, Siebel [28] derived an approximate formula for the mean stress on the cylindrical specimen in terms of the axial yield stress;

$$\overline{\sigma} = \sigma\left(1 + \frac{4\mu d_{S0}}{3l_{S0}}\right) \qquad \text{or} \qquad \sigma = \overline{\sigma}\left(1 + \frac{4\mu d_{S0}}{3l_{S0}}\right)^{-1}, \tag{3.1}$$

where $\overline{\sigma}$ and σ are respectively the mean stress determined from experiment and the net flow stress of a material, μ is the coefficient of Coulomb friction and d_{S0} is the initial specimen diameter. If the coefficient of friction is known then the flow stress of a material can be found. For example, for specimen dimensions $l_{S0} = 1.0$ mm, $d_{S0} = 2.0$ mm and $\mu = 0.06$ the relative increment of stress is $(\overline{\sigma}/\sigma) - 1 = 0.04$, the increase is only 4.0%. It is interesting to note that the coefficient of dynamic friction is lower as a rule than the quasi-static one (slow gliding) [29].

Another possibility to reduce the friction effects is application of a ring specimen [30]. Application of ring specimens in dynamic tests was also reported in several papers [11, 16, 31]. In conclusion, the effect of friction in determination of the flow stress in fast compression tests with a good lubrication is expected to be relatively limited in comparison to other effects like the radial and longitudinal specimen inertia.

Effects of inertia in DICT are very important because of high accelerations and mass velocities observed in such circumstances. One possibility of estimating the radial inertia is integration of the equation of the quantity of movement in the radial direction and application of the Huber-Mises yield condition [11, 20, 32], then

$$\sigma(t) = \overline{\sigma}(t) - \frac{3}{8}\rho\left(\frac{2d_{S0}}{l_{S0}}\right)^2 \frac{V^2(t)}{(1 - \varepsilon_S(t))^2}, \tag{3.2}$$

where $V(t)$ is the current axial velocity of specimen compression $V(t) = V_A(t) - V_B(t)$. The second term in Eq. (3.2) is the stress correction for the radial inertia.

The early numerical analysis of both friction and inertia in SHPB was reported in 1975 [27]. Nowadays many numerical analyses have been published on specimen behavior in high-speed compression and it is out of scope of this paper to review those results.

The most general solutions for both effects, the friction and inertia in the form of overstress, is given by [13, 33]:

$$\Delta\sigma = \frac{\mu\overline{\sigma}}{3s} + \frac{\rho d_S^2}{12}\left(s^2 - \frac{3}{16}\right)(\dot{\varepsilon}_1^2 + \ddot{\varepsilon}) + \frac{3\rho d_S^2}{64}\ddot{\varepsilon}, \tag{3.3}$$

where s is the current ratio of the specimen length to the specimen diameter, $s = l_S/d_S$. The effect of the convection velocity is not taken into consideration. The first term appears because of friction and the next two are the results of inertia. The second term vanishes for all specimens satisfying the conditions:

$s^2 - 3/16 = 0$, or when $\dot{\varepsilon}^2 + \ddot{\varepsilon} = 0$ which may occur for $t > t_r$, where t_r is the rise time of the initial portion of the transmitted wave $\varepsilon_T(t)$. The ratio $s_D = \sqrt{3}/4$, ($s_D = 0.433$) for Poisson's ratio $\nu = 1/2$ was derived as the optimal one by DAVIES and HUNTER [3], but under assumption $\mu = 0$. According to Eq. (3.3) the stress difference $\Delta\sigma = \overline{\sigma} - \sigma$ shows the absolute minimum and the following s_{opt} is determined as:

$$s_{\text{opt}} = \left[\frac{2\mu\overline{\sigma}}{\rho d_S^2(\dot{\varepsilon}^2 + \ddot{\varepsilon})}\right]^{1/3}. \tag{3.4}$$

One of the most important problems in correct determination of stress-strain characteristics at high and very high strain rates is the thermal softening of specimen material caused by adiabatic heating. The adiabatic heating caused by conversion of plastic work into thermal energy triggers an auto-coherent process of the material softening leading to a decrease of the tangent modulus of stress-strain curve and consequently to a decrease of the flow stress when plastic deformation increases. Because of a positive strain rate sensitivity the process intensifies at very high strain rates. In the final stages of compression some forms of mechanical instability appear in the form of Adiabatic Shear Bands (ASB) leading to failure [34–36]. Since at lower strain rates, typically $\dot{\varepsilon} < 10\ \text{s}^{-1}$, plastic deformation is practically isothermal, in order to make comparison the adiabatic stress-strain characteristics obtained at higher strain rates than $\sim 10^2\ \text{s}^{-1}$ should be corrected into isothermal conditions [34]. A simple correction procedure that was applied in this paper was given earlier [34].

The stress correction for the adiabatic increase of temperature used in further analysis of DICT experiments reported in this paper is given by:

$$\Delta\sigma(\varepsilon)_{\dot{\varepsilon}} \approx \frac{\vartheta\beta\sigma_o f(\dot{\varepsilon})\varepsilon}{\rho(T_0)C_p(T_0)} \qquad \text{or} \qquad \Delta\sigma(\varepsilon)_{\dot{\varepsilon}} \approx A\sigma_o\varepsilon f(\dot{\varepsilon}). \tag{3.5}$$

It can be shown that this approximation is relatively exact for mild steels because of a very limited strain hardening at high strain rates [34]. Of course, the highest decrease of stress caused by adiabatic heating occurs for large plastic strains, when the mean stress and the temperature sensitivity are high and the density and the specific heat are low. Since $f(\dot{\varepsilon})$ is an increasing function of strain rate the effect of adiabatic heating intensifies at high strain rates.

In conclusion, the correction of the flow stress from adiabatic to isothermal conditions becomes more important at high and very high strain rates. After correction into isothermal conditions the constitutive surface $(\sigma, \varepsilon, \dot{\varepsilon})_{T_0} = 0$ can be determined for any metallic material.

4. Experimental results

Compression tests of the polycrystalline tantalum were performed at room temperature in as-received state at five strain rates: 10^{-4} s^{-1}, 10^{-2} s^{-1}, 2.6×10^3 s^{-1}, 2.6×10^3 s^{-1}, 1.1×10^5 s^{-1}, 2.2×10^5 s^{-1}. The tests at static deformation regime were performed on servo-controlled universal machine. The diameter of specimens was $d_{S0} = 5.14$ mm and initial length was $l_{S0} = 2.5$ mm, what gave the initial aspect ratio $s_0 = 0.5$. In order to minimize friction effects a lubrication of MoS2 was applied.

Dynamic compression tests of tantalum at high rates of deformation were carried out at one strain rate of 2.6×10^3 s^{-1} with the use of SHPB of diameter $d_H = 20$ mm with application of the two-wave analysis, which consists of incident and transmitted waves. Dynamic compression tests at very high rates of deformation were performed applying miniaturized DICT method at two strain rates of 1.1×10^5 s^{-1} and 2.2×10^5 s^{-1}. The stress-strain curve has been corrected for adiabatic heating, Eq. (3.5). Thus, all curves were transformed into the isothermal conditions. It is noted that tantalum shows substantial strain rate sensitivity. The final set of quasi-static and dynamic $\sigma(\varepsilon)$ curves is shown in Fig. 3. The range of strain rate is nine decimal orders, that is from 10^{-4} s^{-1} to 2.2×10^5 s^{-1}. All curves are in true coordinates and corrected to isothermal conditions. The effect of strain rate on the flow stress is shown in Fig. 4 for three levels of strain. The rate sensitivity $\beta = (\partial\sigma/\partial \log \dot{\varepsilon})_\varepsilon$ shows two ranges, at lower strains $\beta \approx 46$ MPa and $\beta \approx 260$ MPa above the strain rate threshold $\dot{\varepsilon}_C \approx 1000$ s^{-1}.

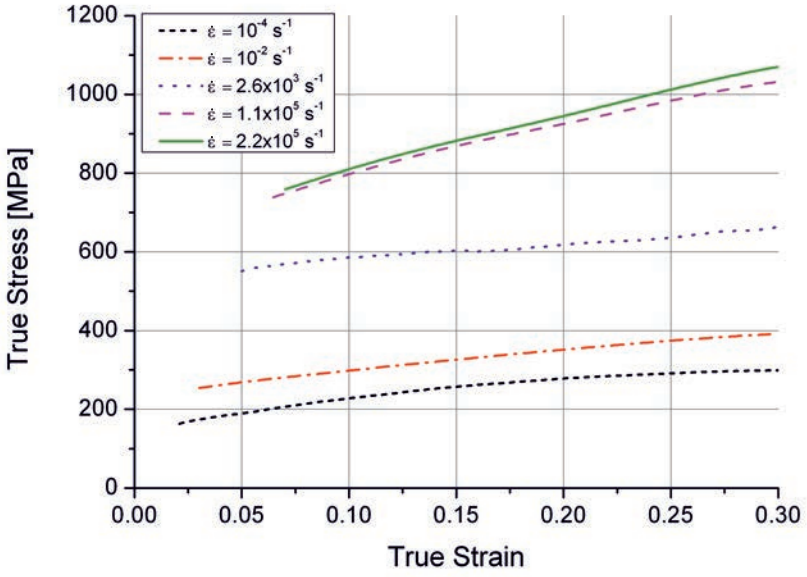

Fig. 3. True stress vs. true strain curves of tantalum at different strain rates.

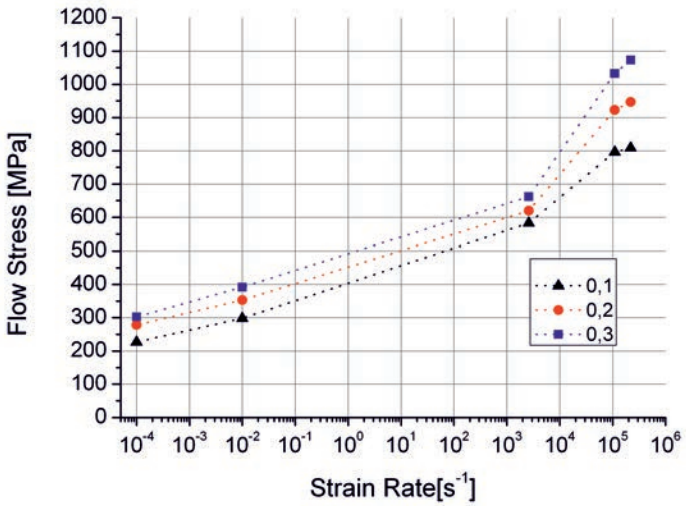

FIG. 4. Rate sensitivity of tantalum at three levels of true strain.

Such, a result suggests existence of two thermally activated dislocation micromechanisms of plastic deformation in those two ranges of strain rate [34].

Figure 5 shows optical micrographs of the as-received tantalum. Grains are regular without any deformations. Grain boundaries are straight at particular sections. Optical micrograph of the material after deformation at rate of 10^{-4} s^{-1} is shown in Fig. 6. Grains are strongly deformed in direction of the applied force. Grain boundaries are irregular and curved. Moreover, the shear bands along two main directions of shearing may be observed in particular grains. Hollows coming from etching shows that a large number of dislocations has occurred which is in agreement with the knowledge concerning plastic deformation mechanisms. Similar effects could be observed for tantalum after prestrain at strain rate of 5×10^3 s^{-1} (Fig. 7).

a) b)

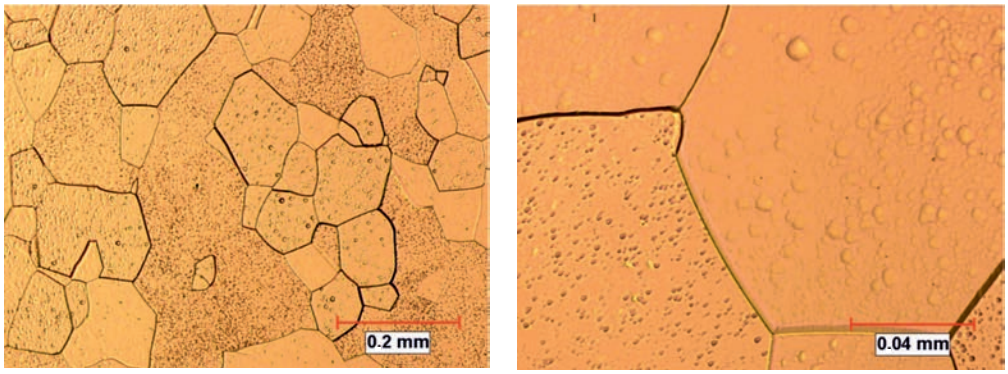

FIG. 5. Optical micrograph of the as-received tantalum at various magnifications.

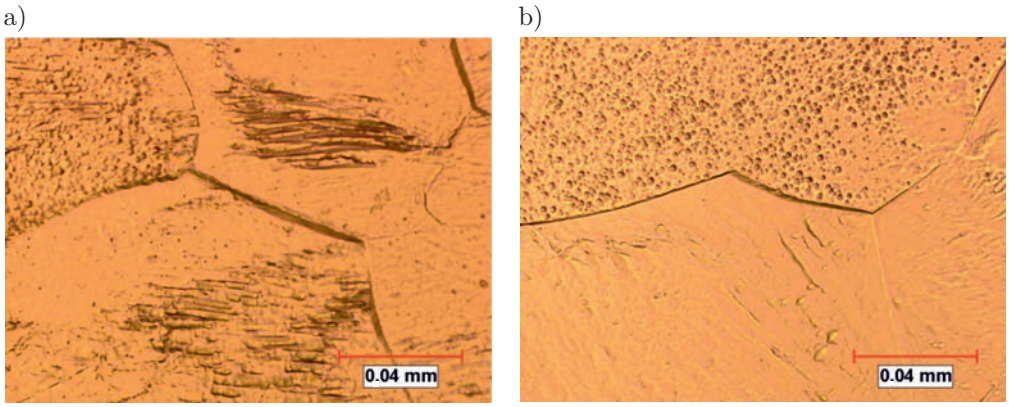

FIG. 6. Optical micrograph of tantalum prestrained using strain rate of 10^{-4} s^{-1}, a) longitudinal cross-section, b) transverse cross-section.

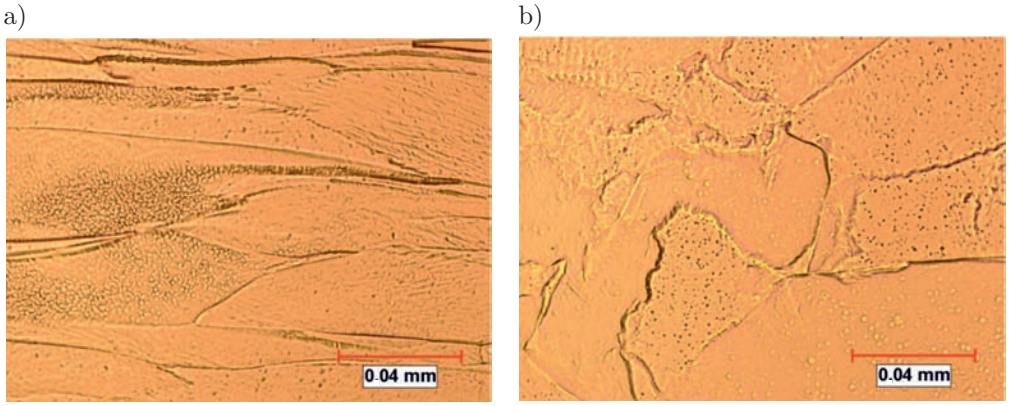

FIG. 7. Optical micrograph of tantalum prestrained using strain rate of 5×10^3 s^{-1}, a) longitudinal cross-section, b) transverse cross-section.

5. Discussion and conclusions

Introduction of specimen miniaturization in high strain rate materials testing, in both cases of SHPB and DICT, enables reaching of high strain rates up to $\sim 10^5$ s^{-1}. Typical dimensions applied in miniaturized tests are 1.0 mm $< l_{S0} <$ 2.0 mm, 1.0 mm $< d_{S0} <$ 2.0 mm and $0.5 < s_0 < 1.0$. Such specimen dimensions reduce substantially the effects of inertia reducing at the same time errors when the inertia analysis is neglected. Although a simple inertia analysis or even FE calculations are recommended, application of very small specimens assures minimum errors in determination of material behavior at very high strain rates. Previous analyses of the inertia effects related to the specimen dimensions indicated that the stress increment due to inertia raises

rapidly with strain rate and with specimen dimensions [37]. The strain rate threshold from the thermally activated rate sensitivity to the so-called pseudo-viscosity [9, 11] must be carefully evaluated in the future. On the other hand, specimen miniaturization leads to limitation of grain number in small specimens. For example, if the specimen volume is $v_s = 6.28$ mm^3 ($d_{S0} = 2.0$ mm and $l_{S0} = 0.5$ mm) and the mean grain diameter is 0.1 mm then the volume of each grain is $v_{gr} = 3.15 \times 10^{-3}$ mm^3 and the number of grains in the specimen volume is $N \approx 2 \times 10^3$. Probably this value is a minimum representative for measurement of the mean behavior.

Application of small diameter Hopkinson bars substantially reduces dispersion of elastic waves. Because in DICT technique strain gages are cemented closely to the specimen-bar interface, recommended distance $\sim 5\ d_H$, where d_H is diameter of Hopkinson bar, the transmitted wave gives not much distorted signal from the interface. In addition, the bar vibration in the longitudinal mode superimposed on the transmitted wave is relatively low [3]. However on the other hand it is impossible to monitor the force equilibrium, that is $F_A(t)$ and $F_B(t)$ as a function of time, and the force equilibrium must be assumed. One possibility is an analytic estimation or application a FE code. Because specimens applied in the miniaturized DICT are short the stress gradients within a typical specimen are assumed to be small.

In the version of the DICT arrangement reported in this paper the original and not expensive optical technique to measure displacement of the interface striker-specimen has been applied. Therefore, combination of the opto-electronic measurement of the displacement of interface A and theory of elastic wave propagation enabling measurement of the displacement of interface B, has provided an exact measurement of the specimen strain and strain rate as a functions of time.

Combination of the quasi-static precision compression test, along with application of SHPB along with the miniaturized DICT, makes possible determination of the rate sensitivity of materials for very wide strain rate spectrum, from 10^{-4} s^{-1} to 2.2×10^5 s^{-1}.

References

1. H. Kolsky, *An Investigation of the Mechanical Properties of Materials at Very High Rates of Loading*, Proc. Phys. Soc. London, **62B**, 676, 1949.

2. U. S. Lindholm, *Some Experiments with the Split Hopkinson Pressure Bar*, J. Mech. Phys. Solids, **12**, 5, 317, 1964.

3. E. D. H. Davies, S. C. Hunter, *The Dynamic Compression Testing of Solids by the Method of the Split Hopkins Pressure Bar*, J. Mech. Phys. Solids, **11**, 155, 1963.

4. U. S. Lindholm, L. M. Yeakley, *Dynamic Deformation of Single and Polycrystalline Aluminium*, J. Mech. Phys. Solids, **13**, 41, 1965.

5. J. Harding, E. O. Wood, J. D. Cambell, *Tensile Testing of Materials at Impact Rates of Strain*, J. Mech. Eng. Sci., **2**, 88, 1960.

6. T. Nicholas, *Tensile Testing of Materials at High Rates of Strain, Experimental Mechanics*, **21**, 177, 1981.

7. J. Duffy, J. D. Campbell, R. M. Hawley, *On the Use of a Torsional Split Hopkinson Bar to Study Rate Effects in 1100-0 Aluminium*, J. Appl. Mech., **93**, 3, 83, 1971.

8. P. E. Sensey, J. Duffy, R. M. Hawley, *Experiments on Strain Rate History and Temperature Effects During the Plastic Deformation of Close-Packed Metals*, J. Appl. Mech., Trans. ASME, **45**, 60, 1978.

9. J. D. Campbell, W. G. Ferguson, *The Temperature and Strain-Rate Dependence of the Shear Strength of Mild Steel*, Phil. Mag., **81**, 63, 1970.

10. J. Harding, J. Huddart, *The Use of the Double-Notch Shear Test in Determining the Mechanical Properties of Uranium at Very High Rates of Strain*, Proc. Conf. On Mech. Prop. at High Rates of Strain, Oxford, Conf. Ser., **47**, 49, 1979.

11. C. K. M. Dharan, F. E. Hauser, *Determination of Stress – Strain Characteristic at Very High Strain Rates, Experimental Mechanics*, **10**, 370, 1970.

12. F. Kamler, P. Niessen, R. J. Pick, *Measurement of the Behavior of High Purity Copper at Very High Rates of Strain*, Canad. J. Phys., **73**, 295, 1995.

13. J. Z. Malinowski, J. R. Klepaczko, *A Unified Analytic and Numerical Approach to Specimen Behaviour in the SHPB*, Int. J. Mech. Sci., **28**, 381, 1986.

14. D. A. Gorham, P. H. Pope, O. Cox, *Sources of Error in Very High Strain Rate Compression Tests*, Proc. Conf. on Mech. Prop. at High Rates of Strain, Oxford, Conf. Ser., **70**, 151, 1984.

15. U. S. Lindholm, *Deformation Maps in the Region of High Dislocation Velocity*, Proc. IUTAM Symposium on High velocity Deformation of Solids, Tokyo, 1977, Springer-Verlag, Berlin Haidelberg New York, **26**, 1978.

16. D. A. Gorham, *Measurement of Stress-Strain Properties of Strong Metals at Very High Rates of Strain*, Proc. Conf. On Mech. Prop. At High Rates Strain, Oxford, Conf. Ser., **47**, 16, 1979.

17. N. A. Safford, *Materials Testing up to 10^5 s^{-1} Using a Miniaturized Hopkinson Bar with Dispersion Corrections*, Proc. 2nd Int. Symp. on Intense Dynamic Loading and its Efects, Sichuan University Press, Chengdu, China, 378, 1992.

18. D. Jia, K. T. Ramesh, *A Rigorous Assessment of the Benefits of Miniaturization in the Kolsky Bar System*, Experimental Mechanics, **44**, 445, 2004.

19. D. A. Gorham, *A Numerical Method for the Correction of Dispersion in Pressure Bar Signals*, J. Phys. E: Sci. Instrum., **16**, 477, 1983.

20. J. R. Klepaczko, *Advanced Experimental Techniques in Materials Testing*, [in:] *New Experimental Methods in Material Dynamics and Impact*, IPPT, Polish Academy of Sciences, Warsaw, p. 223, 2002.

21. D. Ostwald, J. R. Klepaczko, P. Klimanek, *Compression Tests of Polycrystalline α-Iron up to High Strains Over a Large Range of Strain Rates*, J. Phys. IV, Colloque C3, France, **7**, C3/385, 1997.

22. K. T. Ramesh, S. Narasimhan, *Finite Deformations and the Dynamic Measurement of Radial Strains in Compression Kolsky Bar Experiments*, Int. J. Solids Structures, **33**, 3723, 1996.

23. J. Z. Malinowski, J. R. Klepaczko, Z. L. Kowalewski, *Miniaturized compression test at very high strain rates by direct impact*, Experimental Mechanics, **47**, 451–463, 2007.

24. J. M. Malinowski, J. R. Klepaczko, Z. L. Kowalewski, *Modified version of the direct impact compression test technique*, Dynamic Behaviour of Materials – J.R. Klepaczko Workshop, Metz, 13–15 maj 2009.

25. J. Shioiri, K. Sakino, S. Santoh, *Strain Rate Sensitivity of Flow Stress at Very High Rates of Strain*, IUTAM Symp. Constitutive Relation in High/Very High Strain Rates, Kawata K. and Shioiri J. [Eds.], Springer-Verlag, Tokyo, **49**, 1966.

26. K. Sakino, J. Shioiri, *Dynamic Flow Stress Response of Aluminum to Sudden Reduction in Strain Rate at Very High Strain Rates*, J. Phys. IV, Colloque C3, France, **1**, C3/35, 1991.

27. L. D. Bertholf, C. H Karnes, *Two Dimensional Analysis of the Split Hopkinson Pressure Bar System*, J. Mech. Phys. Solids, **23**, 1, 1975.

28. E. Siebel, *Grundlagen zur Berechnung des Kraft und Arbeitbedorf bei Schmieden und Walzen*, Stahl und Eisen, **43**, 1295, 1923.

29. R. S. Montgomery, *Friction and Wear at High Sliding Speeds*, Wear, **36**, 275, 1976.

30. B. Avitzur, *Forging of Hollow Discs*, Israel Journal of Technology, **2**, 3, 295, 1964.

31. M. Ashton, D. J. Perry, *A Constitutive Relationship for Metals Compensated for Adiabatic and Friction Effects*, Proc. 6th Int. Conf. on Mechanical and Physical Behaviour of Materials under Dynamic Loading, Kraków, 263, 2000.

32. J. R. Klepaczko, F. E. Hauser, *Radial Inertia in Compression Testing of Materials*, Technical Report (internal), Division of Inorganic Materials, University of California, Berkeley, 1969.

33. J. Z. Malinowski, *Cylindrical Specimen Compression Analysis in the Split Hopkinson Pressure Bar System*, Engng. Trans., **35**, 4, 551, 1987.

34. J. R. Klepaczko, J. Duffy, *Strain Rate History Effects in Body-Center-Cubic Metals*, ASTM-STP 765, 251, 1982.

35. J. R. Klepaczko, *Generalized Conditions for Stability in Tension Test*, Int. J. Mech. Sci., **10**, 297, 1968.

36. S. L. Semiatin, J. J. Jonas, *Formability and Workability of Metals*, ASM, Metals Park, Ohio, 1984.

37. D. A. Gorham, *An Effect of Specimen Size in the High Strain Rate Compression Test*, Proc. Conf. Dymat, Coll. C3, suppl. Journal de Physique III, **1**, C3-411, 1991.

Received May 16, 2011; revised version August 24, 2011.